

AFRL-VA-WP-TR-2006-3006
SUPERSONIC PLASMA FLOW
CONTROL EXPERIMENTS



Roger L. Kimmel, J.R. Hayes, J.A. Menart, and J.S. Shang

Aerodynamic Components Research Branch (AFRL/VAAA)

Aeronautical Sciences Division

Air Vehicles Directorate

Air Force Materiel Command, Air Force Research Laboratory

Wright-Patterson Air Force Base, OH 45433-7542

DECEMBER 2005

Final Report for 01 January 2002 – 30 December 2005

Approved for public release; distribution is unlimited.

STINFO COPY

AIR VEHICLES DIRECTORATE

AIR FORCE MATERIEL COMMAND

AIR FORCE RESEARCH LABORATORY

WRIGHT-PATTERSON AIR FORCE BASE, OH 45433-7542

NOTICE AND SIGNATURE PAGE

Using Government drawings, specifications, or other data included in this document for any purpose other than Government procurement does not in any way obligate the U.S. Government. The fact that the Government formulated or supplied the drawings, specifications, or other data does not license the holder or any other person or corporation; or convey any rights or permission to manufacture, use, or sell any patented invention that may relate to them.

This report was cleared for public release by the Air Force Research Laboratory Wright Site (AFRL/WS) Public Affairs Office and is available to the general public, including foreign nationals. Copies may be obtained from the Defense Technical Information Center (DTIC) (<http://www.dtic.mil>).

2006-VA-WP-TR-2006-3006 HAS BEEN REVIEWED AND IS APPROVED FOR PUBLICATION IN ACCORDANCE WITH ASSIGNED DISTRIBUTION STATEMENT.

**/Signature/*

ROGER L. KIMMEL
Project Engineer
Aerodynamic Configuration Branch

//Signature//

CARL P. TILMANN
Technical Advisor
Aerodynamic Configuration Branch

//Signature//

MICHAEL J. STANEK, Ph.D.
Technical Advisor
Aeronautical Sciences Division

This report is published in the interest of scientific and technical information exchange, and its publication does not constitute the Government's approval or disapproval of its ideas or findings.

Disseminated copies will show “//signature//*” stamped or typed above the signature blocks.

REPORT DOCUMENTATION PAGE

Form Approved
OMB No. 0704-0188

The public reporting burden for this collection of information is estimated to average 1 hour per response, including the time for reviewing instructions, searching existing data sources, gathering and maintaining the data needed, and completing and reviewing the collection of information. Send comments regarding this burden estimate or any other aspect of this collection of information, including suggestions for reducing this burden, to Department of Defense, Washington Headquarters Services, Directorate for Information Operations and Reports (0704-0188), 1215 Jefferson Davis Highway, Suite 1204, Arlington, VA 22202-4302. Respondents should be aware that notwithstanding any other provision of law, no person shall be subject to any penalty for failing to comply with a collection of information if it does not display a currently valid OMB control number. **PLEASE DO NOT RETURN YOUR FORM TO THE ABOVE ADDRESS.**

1. REPORT DATE (DD-MM-YY) December 2005		2. REPORT TYPE Final		3. DATES COVERED (From - To) 01/01/2002– 12/30/2005	
4. TITLE AND SUBTITLE SUPERSONIC PLASMA FLOW CONTROL EXPERIMENTS				5a. CONTRACT NUMBER In-house	
				5b. GRANT NUMBER	
				5c. PROGRAM ELEMENT NUMBER 0601102	
6. AUTHOR(S) Roger L. Kimmel, J.R. Hayes, J.A. Menart, and J.S. Shang				5d. PROJECT NUMBER A03U	
				5e. TASK NUMBER	
				5f. WORK UNIT NUMBER 0B	
7. PERFORMING ORGANIZATION NAME(S) AND ADDRESS(ES) Aerodynamic Components Research Branch (AFRL/VAAA) Aeronautical Sciences Division Air Vehicles Directorate Air Force Materiel Command, Air Force Research Laboratory Wright-Patterson Air Force Base, OH 45433-7542				8. PERFORMING ORGANIZATION REPORT NUMBER AFRL-VA-WP-TR-2006-3006	
9. SPONSORING/MONITORING AGENCY NAME(S) AND ADDRESS(ES) Air Vehicles Directorate Air Force Research Laboratory Air Force Materiel Command Wright-Patterson Air Force Base, OH 45433-7542				10. SPONSORING/MONITORING AGENCY ACRONYM(S) AFRL-VA-WP	
				11. SPONSORING/MONITORING AGENCY REPORT NUMBER(S) AFRL-VA-WP-TR-2006-3006	
12. DISTRIBUTION/AVAILABILITY STATEMENT Approved for public release; distribution is unlimited.					
13. SUPPLEMENTARY NOTES Report contains color. PAO Case Number: AFRL/WS 06-0097, 11 Jan 2006.					
14. ABSTRACT A magneto aerodynamic channel was designed and constructed to investigate plasma flow control. Detailed, spatially resolved measurements of dc discharges in the channel freestream were obtained. The flow exaggerated nonuniformities in number density and conductivity. Conductivity was highest near the cathode, and air flow increased conductivity by 2 orders of magnitude near the cathode, compared to a no-flow discharge. There was no significant increase in translational temperature, except near electrode surfaces. There was some limited evidence of vibrational relaxation downstream. Longitudinal dc discharges were created between surface electrodes on a flat plate. Transverse magnetic fields applied parallel to the plate surface created Lorentz forces either into or out of the plate surface. With no applied magnetic field, the discharge increased surface pressure through boundary layer heating and subsequent viscous interaction. A Lorentz force directed into the plate inhibited surface pressure increases, and a Lorentz force in the opposite direction enhanced them. Although this is consistent with a Lorentz force acting on the fluid, joule heating is the dominant effect.					
15. SUBJECT TERMS Supersonic, plasma, MHD, boundary-layer					
16. SECURITY CLASSIFICATION OF:			17. LIMITATION OF ABSTRACT: SAR	18. NUMBER OF PAGES 92	19a. NAME OF RESPONSIBLE PERSON (Monitor) Roger L. Kimmel
a. REPORT Unclassified	b. ABSTRACT Unclassified	c. THIS PAGE Unclassified			

Table of Contents

Table of Contents	iii
List of Figures	iv
List of Acronyms, Abbreviations, and Symbols	vii
Abstract	x
1. Plasma Flow Control for Boundary Layers	1
1.1. Introduction	1
1.2. MHD Control	2
1.3. Control via Joule Heating	8
1.4. Summary and Overview of Report	9
2. Plasma Channel Development and Diagnostics	13
2.1. Introduction	13
2.2. Design Requirements	13
2.3. Construction of the Channel	14
2.4. Subsystems and Aerodynamic Instrumentation	15
2.5. Tunnel Calibration	17
3. Microwave Instrumentation	22
3.1. Introduction	22
3.2. Data Reduction Procedure	23
3.3. Problems Encountered	25
3.4. Results	28
4. Freestream Plasma Characterization and Optical Temperature Measurement	38
4.1. Introduction	38
4.2. Temperature Measurement – Method and Verification	38
4.3. Langmuir Probe Measurements	39
4.4. Results	40
4.4.1. Langmuir Probe Measurements	40
4.4.2. Temperature and Pitot Measurements	41
4.5. Summary	43
5. Thermal Actuation Using Surface Discharges	52
5.1. Introduction	52
5.2. Experiment	52
5.3. Results	53
5.3.1. No Applied Magnetic Field	53
5.3.2. Thermal Response of the Plate and Electrode	55
5.3.3. Effect of Magnetic Field on Applied Voltage	56
5.3.4. Effect of Magnetic Field on Surface Pressures	57
5.4. Summary	59
6. References	70

List of Figures

Figure 1 Ratio of axial force due to skin friction to overall axial force for a slender hypersonic configuration.	10
Figure 2 Ratio of integrated laminar to turbulent heat transfer for a hypersonic configuration.	10
Figure 3 Forces and currents in MHD flow of ionized fluid.	10
Figure 4 Instantaneous second-mode wall pressure fluctuations in a flat-plate, non-MHD, $M=4.5$ boundary layer (Ref. 40).	11
Figure 5 Instantaneous second-mode wall pressure fluctuations in a flat-plate, MHD boundary layer flow through a 1.2 T field, $M=4.5$ (Ref. 40).	11
Figure 6 Voltage required to generate a 50 mA discharge as a function of magnetic field strength.	12
Figure 7 Schematic of the plasma channel. All dimensions centimeters. Flow is from left-to-right.	18
Figure 8 Photograph of the Mach 5 Plasma Channel.	18
Figure 9 Ratio of Pitot to stagnation pressure along channel centerline. $x = 0$ corresponds to the nozzle exit.	19
Figure 10 Vertical survey of Pitot pressure, normalized by stagnation pressure, at three axial stations.	19
Figure 11 Pitot survey in spanwise direction at three vertical locations, $x=0$	20
Figure 12 Pitot survey in spanwise direction at three vertical locations, $x=5.1$ cm.	20
Figure 13 Pitot survey in spanwise direction at three vertical locations, $x=5.1$ cm.	21
Figure 15 Ku-band horn and wave guide (back) and X-band horn and wave guide (front).	30
Figure 16 X-band horns in operation on Mach 5 wind tunnel with a plasma discharge.	31
Figure 17 Front view of a 100 mA DC discharge generated with upstream pointing, shod electrodes.	31
Figure 18 Front view of a 500 mA DC discharge generated with upstream pointing, shod electrodes.	31
Figure 19 Absorption of microwave power as a function of electron number density and collision frequency for a microwave beam at 10 GHz and a path length of 7 cm. The full range of absorption values are shown for Eqn. (10).	32
Figure 20 Absorption of microwave power as a function of electron number density and collision frequency for a microwave beam at 10 GHz and a path length of 7 cm. The full range of absorption values are shown for Eqn. (10).	32
Figure 21 Transmitted microwave power through a boundary layer plasma and with no plasma as a function of the separation between the horns or wave guides.	33
Figure 22 Interference pattern of a transmitted microwave beam as a function of separation distance between the horns with no plasma.	33
Figure 23 Transmitted 10 GHz microwave power as a function of the separation between the X-band horns with the plasma off and the plasma on. The plasma discharge is a core flow plasma.	34

Figure 24 Interference pattern of a 10 GHz transmitted microwave beam as a function of separation distance between the X-band horns with the plasma off for several absorbing pad configurations.....	34
Figure 25 Interference pattern of a 10 GHz transmitted microwave beam as a function of separation distance between the X-band horns with the plasma off for the hole configuration. The no absorbing pad and the absorbing pad on the transmitting horn cases are also shown for comparison.....	35
Figure 26 Transmitted 10 GHz microwave power as a function of the separation between the X-band horn for the plasma-off and the plasma-on cases utilizing an absorbing pad on the transmitting horn and an absorbing pad with a hole in it on the receiving horn. The plasma discharge is a core flow plasma.....	35
Figure 27 Electron number density versus discharge current for thin shoe electrodes with no flow through wind tunnel. Plasma produced was a glow discharge at 7 torr.....	36
Figure 28 Electron number density versus discharge current for thin shoe electrodes with Mach 5 flow and a stagnation pressure of 300 torr. Plasma produced was a core flow plasma.....	36
Figure 29 Electron number density vs. current for different electrodes, with Mach 5 flow and a stagnation pressure of 300 torr. The microwave frequency was 10 GHz, and the plasma produced was a core flow plasma.....	37
Figure 30 Nitrogen second positive group spectra for static discharge tube and Mach 5 DC glow discharge.....	44
Figure 31 Photograph of discharge with Pitot probe. Note shock structure between electrodes.....	44
Figure 32 Ion number density in a 50 mA discharge, no-flow case. In this and next figures, spanwise location is in the center of the electrodes.....	45
Figure 33 Ion number density in a 50 mA discharge, flow-on.....	45
Figure 34 Electron temperature in a 50 mA discharge, no-flow case.....	46
Figure 35 Electron temperatures measured in a 50 mA discharge, flow-on case.....	46
Figure 36 Plasma conductivity in a 50 mA discharge, flow-off case.....	47
Figure 37 Plasma conductivity measured with the Langmuir probe in a 50 mA discharge.....	47
Figure 38 Rotational temperatures measured in discharge as a function of current. Error bars represent + / - 10K uncertainty.....	48
Figure 39 Ratio of current-on Pitot pressure to current-off Pitot pressure.....	48
Figure 40 Schlieren image of shock produced by a sphere in the presence of a DC discharge. Luminosity from the discharge is evident between the plate electrodes on the left. The darker vertical strip in the middle is the superimposed schlieren image in the absence of a discharge.....	49
Figure 41 Rotational temperatures for 100 and 400 mA DC discharge between plates, streamwise distribution at $y/y_p = 0.0$	49
Figure 42 Vibrational temperatures for 100 and 400 mA DC discharge between plates, streamwise distribution at $y/y_p = 0.0$	50
Figure 43 Rotational temperatures for 100 and 400 mA DC discharge between plates, vertical distribution at $x/x_p = 0.7$	50
Figure 44 Vibrational temperatures for 100 and 400 mA DC discharge between plates, vertical distribution at $x/x_p = 0.7$	51

Figure 45	Vibrational temperatures for DC discharges between plates, at $x/x_p = 0.7$, $y/y_p = 0.0$ as a function of discharge current.....	51
Figure 46	Schematic of flat plate model. All dimensions cm. Electrodes are 0.64 cm wide. Pressure taps are spaced 1.27 cm, starting at $x = 2.48$ cm.	60
Figure 47	Pitot pressure near plate surface, normalized by stagnation pressure, as a function of stagnation pressure.	61
Figure 48	Pitot survey at $x = 5.65$ cm from leading edge.....	61
Figure 49	Effect of DC discharge on flat plate surface pressures. Pressures are normalized by undisturbed ($U=0$) static pressures.	62
Figure 50	Sample voltage trace during discharge.....	62
Figure 51	Electron number density as a function of streamwise distance at four locations above plate surface. Measurements made on model centerline.	63
Figure 52	Average discharge-on total temperature measurements at three locations above plate surface, normalized by stagnation temperature.....	63
Figure 53	Average Pitot pressure above downstream electrode (anode) on flat plate.....	64
Figure 54	Average Pitot pressure during discharge normalized by undisturbed Pitot pressure as a function of distance along the model for two heights above the plate.	64
Figure 55	Normalized surface pressure at stations 1, 2, 3 ($x = 2.48, 3.75$ and 5.02 cm, respectively) as a function of discharge input power. Pressure is normalized by discharge-off pressure.....	65
Figure 56	100 mA, 140W discharge, point A in Figure 55. View is from location downstream and above plate. Flow is from top-to-bottom, cathode is at top of image.....	65
Figure 57	400 mA, 170 W discharge, point B in Figure 55.....	65
Figure 58	Ratio of average Pitot pressure during discharge to undisturbed Pitot pressure for four different discharge durations.	66
Figure 59	Pitot pressure measured 0.5 cm above the plate surface at the downstream edge of the rear electrode.....	66
Figure 60	Cathode temperature as a function of time before and after a ten-second discharge (left), and peak cathode temperature as a function of discharge-on time.	67
Figure 61	Effect of magnetic field on the voltage required to drive a given current.....	67
Figure 62	Images showing the effect of transverse magnetic fields on the glow from a surface discharge. Flow is from left-to-right, cathode upstream.	68
Figure 63	Induced pressure at each measuring station as a function of power. Squares, cathode upstream, triangles, cathode downstream.....	68
Figure 64	Pressure induced by the discharge at each measuring station plotted versus the product of current and magnetic field.....	69

List of Acronyms, Abbreviations, and Symbols

B, B	magnetic field
C	Chapman-Rubensin parameter, $\rho_w \mu_w / \rho_e \mu_e$
C_1	coefficient relating skin friction to Reynolds number, $c_f = C_1 \text{Re}^{-1/2}$, nondimensional
C_2	coefficient relating boundary layer thickness to Reynolds number, $(\delta/L) = C_2 \text{Re}^{-1/2}$, nondimensional
C_A	axial force coefficient
c_f	skin friction coefficient, nondimensional
c_h	heat transfer coefficient, nondimensional
D	constant depending on experimental setup in optical emission measurements
d	path length through plasma
e	electron charge
E	Electric field vector
F	force vector
$G(v')$	energy of a vibrational state
h	Planck constant
Ha	Hartmann number
i	$\sqrt{-1}$
\mathbf{j}, j	current density vector and magnitude
k	Boltzmann constant
J	current magnitude, amperes
K	load factor, E / uB , nondimensional
L	length scale in interaction parameter
M	Mach number
m	electron mass
n	electron number density
N	total molecular species population in a given electronic state
$N_{v'}$	population of upper vibrational state

P	power
p	pressure
Q	MHD interaction parameter, nondimensional
Q^*	modified MHD interaction parameter based on friction velocity, nondimensional
$Q_v(T)$	vibrational partition function
\mathbf{r}	electron displacement vector, m
Re	Reynolds number
$S_{v',v''}$	band strength for vibrational transition
T	temperature
t	time
\mathbf{u}, u	velocity vector and magnitude, m/s
u^*	friction velocity, $\sqrt{\tau_w / \rho_w}$, m/s
\mathbf{v}_d, v_d	drift velocity vector and magnitude
x, y, z	spatial coordinates
x_p	electrode length in the streamwise direction, 45.7mm
y_p	one-half of vertical separation between discharge electrodes, 25.4 mm
β	Hall parameter, $\omega\tau$, nondimensional
χ	attenuation index
$\bar{\chi}$	chi-bar parameter
ε_0	permittivity of free space
γ	ratio of specific heats, nondimensional
κ	complex dielectric constant for a medium
μ	complex refractive index
μ_r	real part of the complex refractive index
ν	electron collision frequency for momentum transport
ρ	density, kg/m ³
σ	conductivity, mho/m
τ	skin friction, N/m ² , or collision frequency
ω	frequency of oscillating electric field, or electron cyclotron frequency

ω_p plasma frequency, $\sqrt{\frac{ne^2}{m\epsilon_0}}$

Subscripts

0 stagnation
abs absorbed
d drift
e edge conditions
H Hall
 $I_{v',v''}$ intensity of a vibrational transition from state v' to v''
inc incident
LAM laminar
r real
rot rotational
SF skin friction
trans translational
TURB turbulent
t2 total pressure after normal shock (measured Pitot pressure)
 v' upper vibrational state
 v'' lower vibrational state
vib vibrational
w wall conditions
 ∞ conditions upstream of model bow shock

Abstract

A magneto aerodynamic channel was designed and constructed to investigate plasma flow control. Detailed, spatially resolved measurements of DC discharges in the channel freestream were obtained using Langmuir probes, microwave absorption, and emission spectroscopy. Flow-off discharges were compared to flow-on discharges. The flow exaggerated nonuniformities in number density and conductivity that were present without flow. Conductivity was highest near the cathode, and air flow increased conductivity by two orders of magnitude near the cathode, compared to a no-flow discharge. There was no significant increase in translational temperature, except near electrode surfaces. There was some limited evidence of vibrational relaxation downstream.

After the plasma characteristics were measured, longitudinal DC discharges were created between surface electrodes on a flat plate. Transverse magnetic fields applied parallel to the plate surface created Lorentz forces either into or out of the plate surface. With no applied magnetic field, the discharge increased surface pressure through boundary layer heating and subsequent viscous interaction. A Lorentz force directed into the plate inhibited surface pressure increases, and a Lorentz force in the opposite direction enhanced them. Although this is consistent with a Lorentz force acting on the fluid, Joule heating is the dominant effect. It is unclear how much of the magnetic field effect was due directly to a Lorentz force, and how much was due to Joule heating modification by the magnetic field.

1. Plasma Flow Control for Boundary Layers

1.1. Introduction

Since the beginning of powered flight, the necessity of modulating fluid momentum about flight vehicles has been recognized. This modulation has taken such forms as flaps or ailerons for attitude control, or suction or blowing to alleviate undesirable momentum changes. Traditionally, fluid momentum was modulated by mechanical actuators. The application of magnetohydrodynamic (MHD) forces and Joule heating to plasmas creates the possibility of no-moving-parts flow control.

Viscous phenomena assume a special importance in hypersonic flight. An overriding concern is heat transfer, which is primarily a boundary layer phenomenon. Frictional heating causes the boundary layer thickness to increase as Mach number increases, leading to viscous interaction between the growing boundary layer and the external inviscid flow, altering the vehicle pressure distribution. The interaction of thick boundary layers with control surfaces may reduce control effectiveness. Although wave drag dominates blunt configurations, skin friction drag becomes important for slender configurations.¹

The effects of viscous phenomena depend to a great extent on whether the boundary layer is laminar or turbulent. Estimates for the National Aerospace Plane (NASP)² showed that the payload-to-gross-weight ratio would nearly double if the vehicle boundary layer were fully laminar, compared to fully turbulent.

A generic hypersonic transport was considered in Ref. 1 to assess the relative effects of skin friction and heat transfer. The hypersonic transport described in Ref 3 was chosen as a baseline. For this study, the vehicle was sized at 61 m in length, a reasonable value for vehicles designed for sustained hypersonic flight. The longer the vehicle, the greater the wetted area and the greater the contribution of skin friction. The analysis conditions were Mach 8, 10, 12, and 14. The altitude was varied at each Mach number to keep the freestream dynamic pressure constant at 71.8 kPa, which is again a reasonable value for an airbreathing trajectory. These conditions produced Reynolds numbers based on freestream conditions and vehicle length from 131×10^6 (Mach 14) to 247×10^6 (Mach 8). The configuration was analyzed using the Supersonic, Hypersonic, Arbitrary Body Program (SHABP).⁴ SHABP calculates skin friction using correlations based on the length Reynolds number along each body panel. The boundary layer was treated as either all laminar or all turbulent to provide upper and lower bounds on skin friction. Calculations were carried out for zero angle of attack. The inlet was treated as flow-through, and no drag was calculated for the internal surfaces. The results here are representative of large, slender vehicles with significant wetted area.

Figure 1 shows that the for fully laminar or fully turbulent conditions, the percentage of drag due to skin friction varies little over the Mach number range examined. For fully turbulent flow, skin friction contributes over 30 percent of the overall vehicle drag. For fully laminar flow, the skin friction contribution is about 10 percent. Given the large length Reynolds numbers, it is quite likely that the bulk of the flow over the vehicle is turbulent, even at the highest Mach number. A similar vehicle analyzed by Finley⁵

showed 65 percent to 100 percent of the vehicle area turbulent at Mach 15, depending on whether a correlating factor of $Re_\theta/M = 300$ or 100 (respectively) was used.

Heat transfer to the vehicle was estimated from the skin friction results, using the Reynolds analogy, $c_H = 1/2c_f$. The ratio of fully laminar to fully turbulent heat transfer, integrated over the vehicle, is shown in Figure 2. At Mach 8, turbulent heat transfer is up to eight times laminar heat transfer. Increased heating has a negative impact on vehicle performance. Heating must be managed either through increased thermal protection or active cooling, or by restricting the vehicle trajectory to limit higher velocity flight to high altitude. The first strategy results in increased weight, and the second results in reduced range.

The requirement to control boundary layer transition and boundary layer thickness in airbreathing hypersonic engines and inlets has been noted.⁶ The presence of the boundary layer has a number of deleterious effects on engine performance.⁷ The boundary layer increases flow distortion and reduces mass flux through the inlet. Boundary layer separation, which is a strong function of the state of the boundary layer, laminar or turbulent, exacerbates these effects and also can lead to unsteadiness and locally increased heating. The study cited in Ref. 6 listed surface discharges for reducing skin friction and controlling transition as a technology worthy of further investigation.

The benefits of being able to control the development of the viscous boundary layer on high-speed vehicles are clear. A number of factors make plasma boundary layer control an attractive option. At high hypersonic Mach numbers where boundary layer ionization is thermal in nature, the highest temperatures and ionization levels downstream of the bow shock will occur within the boundary layer.⁸ For control methods involving artificially ionized plasmas, boundary layer control relies on ionization of only the near-body fluid, in contrast to inviscid flow-control schemes involving the ionization of large volumes of plasma. Presumably, since the volume of ionized fluid is less, power requirements would also be lessened. Also, the boundary layer is easier to ionize than the inviscid flow due to its lower density. The sensitivity of boundary layer transition to the mean boundary layer state means that even small MHD control inputs may have a large effect on the overall system. Glow-discharges have been used for many years to excite boundary layer instabilities in supersonic^{9,10} and hypersonic flows.¹¹ MHD boundary layer control exploits the fact that fields from on-board magnets will be highest near the vehicle surface. Also, control inputs can be limited to locations where they are most effective to reduce weight.

This section discusses some aspects and recent advances in the application of plasmas to high-speed boundary layer control. Two control methods, MHD control and Joule heating, are examined in detail. A number of recent works have examined electrohydrodynamic (EHD) flow control in low-speed boundary layers, but as of yet this technique has not been applied to high-speed flows.

1.2. MHD Control

MHD boundary layer control relies on the forces exerted on a conductor (the plasma) flowing through a magnetic field. In the flow shown in Figure 3, plasma flows over a wall with a magnet embedded in it. Any number of magnetic field arrangements may be

conceived (see Ref. ¹² for example), but the scenario shown in Figure 3 illustrates the basic concept. Assuming a scalar conductivity, a body force \mathbf{F} , generated on the plasma is given by

$$\mathbf{F} = \sigma(\mathbf{E} + \mathbf{u} \times \mathbf{B}) \times \mathbf{B},$$

where σ is the fluid conductivity, \mathbf{u} is its velocity, \mathbf{B} is the magnetic field, and \mathbf{E} is the electric field imposed on the plasma by the external circuit. A primary figure of merit for characterizing MHD flows is the interaction parameter, which is the ratio of Lorentz force ($\sigma \mathbf{u} \times \mathbf{B}$) to inertial forces on a fluid element. The interaction parameter is

$$Q = \frac{\sigma B^2 L}{\rho u} K.$$

For the time-being, we will consider a load factor of unity. The Lorentz force will be a retarding force, regardless of whether the magnetic field is oriented into or out of the wall, and will decelerate the boundary layer.

Rossow¹³ analyzed the flow of a laminar conducting boundary layer over a flat plate with a magnetic field normal to the plate surface. He considered both the case above, where the magnetic field is fixed relative to the plate, and the case in which the field is fixed to the moving fluid, as would be encountered by a vehicle flying through the earth's magnetic field. Although Rossow's analysis and assumptions are open to some question,¹⁴ the qualitative trends derived from his work are similar to those observed by other investigators. His results show that as the interaction parameter increases, the boundary layer was increasingly decelerated. Skin friction of course decreased, and displacement thickness increased with increasing Q . As noted by Rossow, however, the magnetic-field/fluid interaction that decelerates the fluid also creates a drag on the magnet embedded in the plate, offsetting the decrease in skin friction. In the cases considered by Rossow, the net effect was to increase the overall drag on the plate.

Bush¹⁵ derived a similarity solution for conducting laminar boundary layers in the presence of an applied magnetic field. In the case examined by Bush, the magnetic field was set proportional to $x^{-1/2}$ to obtain a similarity solution. Bush also observed the trend of decreasing skin friction with increasing interaction parameter. Similar effects were predicted by Sastry¹⁶ and correlated with the Hartmann number. The Hartmann number is proportional to the square root of the ratio of MHD to viscous forces per unit fluid volume and is expressed as

$$Ha = KBL \sqrt{\frac{\sigma}{\mu}},$$

where μ is the fluid viscosity. It can be shown that if the same length scale is used,¹⁷ the ratio of the Hartmann number squared is equal to the product of interaction parameter and the Reynolds number.

Borghetti et al.¹⁸ calculated the ionized viscous flow over a blunt leading-edge flat plate. Magnetic fields were created by linear current-carrying conductors embedded within the model, parallel to the leading edge and transverse to the flow. Two cases were considered, one where a magnetic field was imposed at the leading edge, and the other

where the field was imposed at mid-span. In both cases, the applied magnetic field created a local reduction in skin friction. For the case of the field applied at mid-span, this was accompanied by an increase in surface static pressure. The magnetic field at the stagnation point had little, if any, effect on surface pressure.

Poggie and Gaitonde¹⁹ computed laminar viscous MHD flows in the vicinity of the stagnation region of an axisymmetric, spherically blunt body, and report a thorough literature search on this subject. The magnetic field in their computations was a dipole centered at the sphere and aligned with the body axis. They also showed a reduction in stagnation-point skin friction and heat transfer. These results are in qualitative agreement with the earlier theory of Bush.²⁰

Although the density of hypersonic flows is usually relatively low, the combination of high velocities and low conductivity leads to quite low interaction parameters. Compared to liquid metals, for example, the conductivities of typical plasma and electrolyte flows are relatively low. Ref. 14 cites the conductivity of copper at 6×10^7 mho/m, mercury at 10^6 mho/m, and salt water at 25 mho/m. Ionization is insignificant below about Mach 10 for typical trajectories.²¹ Non-equilibrium ionization such as electron beams, direct current (DC), radio frequency (RF), or microwave discharges may be used to produce plasma at lower Mach numbers. For non-equilibrium ionized air, conductivities are typically on the order of one mho/m.^{22,23,24} Measurements reported by Sears²⁵ suggest that conductivities of 100 mho/m may be attained in thermal plasmas above about Mach 16. This can be augmented by seeding the air with an alkali metal. For a flat plate at $M=6$ at 30 km altitude, assuming $\sigma = 1$ mho/m, $L = 1$ meter, and $B = 1$ tesla (conditions achievable in the laboratory), the interaction parameter based on freestream conditions is $Q=0.03$, indicating that the Lorentz force imposed on the fluid is quite small compared to the fluid inertia.

However, the interaction parameter within the boundary layer should be larger than the freestream MHD interaction parameter. The freestream or edge velocity is not a suitable scale for assessing MHD boundary layer flows, since the boundary layer velocities are lower than the edge velocity. Analysis of experiments by Heno and Stace²⁶ on MHD control of turbulent salt-water, flat plate boundary layers showed that the friction velocity u^* , where

$$u^* = \sqrt{\frac{\tau_w}{\rho_w}}$$

and τ_w and ρ_w are the skin friction and density evaluated at the wall, was an appropriate velocity scale for a modified interaction parameter, Q^* ... The friction velocity is a more appropriate scale for boundary layer phenomena since it is much less than the edge velocity. Macheret et al.,²⁴ have also suggested using u^* as a velocity scale in the interaction parameter for boundary layer flows. As noted by Macheret et al.,²⁴ by expressing the skin friction in terms of the skin friction coefficient, c_f ,

$$\tau_w = \frac{1}{2} \rho U^2 c_f$$

the interaction parameter based on the friction velocity, Q^* , for a load factor of one, is related to the interaction parameter based on freestream velocity by

$$Q^* = Q \sqrt{\frac{2}{c_f}}$$

Since c_f is typically $O(10^{-3})$ ²⁷, the interaction parameter based on friction velocity can be 40 times that based on freestream velocity.

All other conditions being equal, the interaction parameter for an applied electric field based on u^* rather than U is larger by a factor of $(U/u^*)^2$. For the current experiments, this ratio is 280, and the largest value of Q^* obtained is 2.5, based on a friction velocity derived from a similarity solution for a laminar boundary layer.

For laminar flows, Q^* is also simply related to the Hartmann number, which is conventionally used to describe laminar MHD shear layers. For laminar, flat-plate boundary layers, the skin friction is proportional to the inverse square root of the length Reynolds number, $c_f = C_1 \text{Re}^{-1/2}$. The length scale for the Hartmann number is some measure of the shear layer thickness, but for a laminar flat plate boundary layer the ratio of velocity thickness to streamwise dimension is inversely proportional to the square root of the Reynolds number, $(\delta/L) = C_2 \text{Re}^{-1/2}$. With these substitutions, the interaction parameter based on friction velocity $Q^* = (Ha/C_2)^2 \sqrt{2/C_1} \text{Re}^{1/4}$.

The interaction parameter may also be boosted by imposing an electric field. The necessity of boosting the interaction parameter in low-conductivity MHD flows has been recognized and applied for some time to electrolyte MHD flows.^{26,28} The load factor may be larger than one, even in hypervelocity flows. Fields of 10^4 V/m are easily achievable.^{22,23,29} Also, by supplying an external power source, the sign of the imposed electric field may be made opposite to the $\mathbf{u} \times \mathbf{B}$ field. If the imposed field is opposite in sign and greater than $\mathbf{u} \times \mathbf{B}$, the flow may be accelerated instead of decelerated. This MHD acceleration of the boundary layer would be expected to produce a fuller, more stable boundary layer profile and create a propulsive force on the vehicle from the magnetic / electric field interaction (at the expense of increased skin friction). Calculations by Jaffe³⁰ for an incompressible laminar boundary layer demonstrated this trend. It should be noted that as the load factor or current increases, Joule heating also increases.

MHD control of hypersonic boundary layer transition has been considered since at least the 1950s.³¹ There is no doubt that MHD effects may be used to influence mean boundary layer profiles, which in turn moderate hydrodynamic stability for traveling^{31,32,33} and stationary waves.³⁴ MHD forces can also operate on flow fluctuations as well as the mean flow. For example, if the mean flow is co-planar with the magnetic field and no electric field is imposed, $\mathbf{u} \times \mathbf{B} = 0$ and no Lorentz force is generated due to the mean flow. However, boundary layer instabilities generate transverse velocity fluctuations, which in turn generate fluctuating Lorentz forces that oppose them. Stuart's³⁵ calculations for incompressible planar Poiseuille flow of a conducting fluid with a co-planar magnetic field showed that the neutral stability curve shrank with

increasing interaction parameter and was completely stabilized with a sufficiently large interaction parameter. Lock's³⁶ calculations for the same flow with a magnetic field perpendicular to the main flow showed that since this field could operate on the mean flow, it was more effective in stabilizing the flow than the co-planar field.

Limited calculations support the concept of stabilizing the boundary layer to traveling disturbances using MHD forces. Rossow extended calculations of mean MHD boundary layer profiles¹³ to calculate the neutral stability diagrams³¹ for incompressible flat plate, MHD flows with magnetic fields co-planar and transverse to the mean flow. These results showed a fixed co-planar magnetic field or a transverse field moving with the flow to be stabilizing. A transverse field fixed to the flat plate (generating a retarding force on the mean flow) was destabilizing.

In general, for 2D flows above about Mach 5, the dominant boundary layer instability is the second mode.³⁷ The first work to consider MHD effects on second-mode instability was by Cheng et al.^{32,33} This work featured DNS simulation of second-mode instabilities in a flat plate, $M_e = 4.5$ boundary layer. A uniform conductivity of 100 mho/m was imposed on the fluid. A number of dipole magnet configurations were considered. The basic results can be illustrated by considering flow over a dipole pair. The first dipole was placed 0.02 m from the leading edge of the plate, with dipole moment in the positive y-direction. The second dipole was located 0.025 m downstream of the leading edge, with dipole moment in the negative y-direction. Two cases were considered, one with a field strength equal to approximately 2.5 T at the wall, the other with a field strength of approximately 1.2 T at the wall. The interaction parameters, based on edge conditions, were 1.0 and 0.26, respectively.

The flow of the conducting fluid through the magnetic field created an adverse pressure gradient upstream and in the immediate vicinity of the dipole. The adverse pressure gradient was sufficient to separate the boundary layer for the high-interaction-parameter case. Downstream of the magnet, the flow relaxed through a favorable pressure gradient. A second mode disturbance that was unstable in the non-MHD boundary layer was introduced at the upstream boundary. The instantaneous wall pressure (Figure 4) illustrates the instability of the disturbance, as pressure fluctuations increase with increasing x . When the 1.2 T magnetic field was imposed on the same flow, wall pressures showed that the second mode amplification was slightly increased in the initial adverse pressure gradient. The second mode was stabilized through the rest of the interaction, even in regions of adverse pressure gradient (Figure 5). Damping was even higher for the 2.5 T field.

Since it is well known that inflected velocity profiles are generally more unstable than profiles without velocity inflections, the strong damping of instabilities observed in the MHD flows was unexpected. The authors ascribed this effect to the tight tuning of the most unstable second-mode frequency to the boundary layer thickness. Since the boundary layer was dramatically thickened through the interaction, the most unstable frequency was tuned away from the forced disturbance to a lower frequency. This behavior was reminiscent of effects seen in models with geometrically-imposed adverse and favorable pressure gradients.³⁸ Although MHD effects stabilized monochromatic disturbances, it was not clear that transition could be delayed by such a configuration,

since the most unstable frequency would just be shifted to a lower value where other environmental disturbances would amplify. Nevertheless, this work constitutes the first result that second-mode growth may be moderated by MHD effects.

Palm et al.²² measured the effect of MHD forces on a helium channel flow at $M=4$, in an experimental realization of the flow shown in Figure 3. In these experiments, a Nd-Fe-B permanent magnet was mounted in the tunnel sidewall, and electrodes in adjacent walls created an imposed electric field. The flow was pre-ionized upstream of the DC electrodes using an RF discharge. Wall pressure fluctuations were monitored just downstream of the magnet. Wall pressure fluctuations were reduced when a 50 mA current was passed through the DC electrodes, with the bottom DC electrode negative and the top ground. When the electrode polarity was reversed, no effect on pressure fluctuations was observed. When the magnet polarity was reversed, the electrode polarity resulting in pressure fluctuation reductions was also reversed, in this case with the top electrode negative and the bottom ground. The experiment was repeated using unmagnetized, dummy Nd-Fe-B blocks in the tunnel wall. In this case, no effect was observed. These observations further bolstered the authors' conclusions that the observed effects were due to MHD forces on the fluid.

Although it was not clear whether the channel flow was laminar or turbulent, results show that a sufficiently high interaction parameter can be obtained in the laboratory to modify weakly ionized MHD boundary layers. A notable result of the above experiment is that results were achieved at very low interaction parameter, based on edge velocity, $Q = 1.5 \times 10^{-4}$. The interaction parameter based on estimated friction velocity was approximately 0.15.

A surprising result from these experiments was that an electrode polarity that should have exerted an accelerating force on the fluid had no effect, and a polarity that should have generated a decelerating force reduced pressure fluctuations. Pressure measurements were made downstream of the magnet, in the region of return magnetic field lines. Also, the current paths in the interaction are unknown. Future work on this experiment will focus on a larger, better characterized flow and improved diagnostics.³⁹

A complicating factor of MHD boundary layer control is that Hall effects are likely to be present in the low-density, high-magnetic-field scenarios typical of MHD plasma boundary layer control applications.¹² The Hall effect arises in low density flows when the period of revolution of an electron about a magnetic field line becomes appreciable compared to the time between electron-neutral collisions. The magnitude of this effect is described by the ratio of these two times, or the Hall parameter, $\beta = \omega\tau$, where ω is the electron cyclotron frequency, and τ is the period between electron-neutral collisions.⁴⁰ When the Hall parameter is large, electrons in effect become trapped within the magnetic field. This is manifested in two ways. First, the effective resistance of the fluid perpendicular to magnetic field lines increases. The effective conductivity of the plasma perpendicular to the magnetic field lines is reduced by³⁹

$$\sigma_{B \neq 0} = \frac{\sigma_{B=0}}{1 + \beta^2},$$

and the current responsible for the Faraday force, that perpendicular to the magnetic field lines, is correspondingly reduced.

This reduction in the effective conductivity of the fluid perpendicular to magnetic field lines is demonstrated graphically in Figure 6, from Ref. 23. In this case, a 50 mA DC discharge between two electrodes on a flat plate was created. A magnetic field perpendicular to the flat plate was imposed. The discharge was run in a constant-current mode. As B increases, the voltage required to sustain the 50 mA discharge increases. Based on the Equation above, the Hall parameter was estimated to be approximately one at $B=0.9\text{T}$. Similar results were observed in Ref. 39, where the discharge was run in a voltage-stabilized mode, and the current was allowed to vary with B . In this case, a Hall parameter of three was inferred at the maximum field achievable in the experiment, $B=1.4\text{ T}$.

The second effect of a large Hall parameter is the generation of an additional current, the Hall current with its own corresponding $\mathbf{j}\times\mathbf{B}$ force. The Hall force may be visualized by considering that the drift velocity, v_d , of the charge carriers becomes appreciable. This gives rise to an additional force on the electrons, $\mathbf{v}_d \times \mathbf{B}$, creating the Hall current, j_H parallel to the velocity vector.⁴⁰ The interaction of the Hall current and the magnetic field produces the Hall Force, $\mathbf{j}_H \times \mathbf{B}$, perpendicular to both the magnetic field and the Faraday force. This creates an inherent three dimensionality in the MHD forces. For the flow shown in Figure 3, the Hall force would tend to push the flow against one of the sidewalls. The inevitability of Hall effects in low-density flows has been known for some time, and numerous schemes have been developed for dealing with them.^{12,39,40}

It is conceivable that the Hall forces could be exploited in conjunction with the Faraday force to aid in controlling the boundary layer. For the scenario shown in Figure 3, a boundary layer crossflow would be created that might be used to negate crossflow instability on a swept wing, for example.

1.3. Control via Joule Heating

Boundary layers may be manipulated by the application of electrical fields alone, either through Joule heating of the fluid or EHD forces on the plasma. An advantage of this form of boundary layer control over MHD control is that no magnets are required. A number of researchers have exploited EHD forces in subsonic boundary layers on flat plates using glow discharges,⁴¹ and corona discharges.^{42,43} Glow discharges have been used to delay separation and enhance lift on airfoils^{44,45,46,47} and to trip the boundary layer on 3D airfoils.⁴⁸ Wilkinson⁴⁹ has explored spanwise-oscillating discharges as a means of reducing Reynolds stress and skin friction in turbulent boundary layers. As of the time of this publication, EHD control has not been applied explicitly to hypersonic boundary layers. Macheret et al.²⁴ suggest that velocities induced by EHD effects could be appreciable at low density, but also note that Joule heating effects may be hard to separate from EHD effects.

Limited results on Joule heating control have been obtained in supersonic boundary layers. Analysis of surface microwave discharges⁵⁰ indicates local heating, with attendant increases in pressure and boundary layer displacement thickness, for these flows. Leonov et al.^{51,52,53,54,55} has considered pulsed DC discharges in subsonic,

transonic, and low supersonic flows. In these experiments, pulses of up to 10 kW and 60 ms duration are applied to electrodes in the wall. These discharges are created between wall electrode pairs, usually separated transversely relative to the flow. For lower power discharges, the boundary layers were observed to thicken, increasing wall pressure and creating a wave structure above the boundary layer edge. Sufficiently high-power discharges separated the boundary layer and even caused choking in duct flows.

1.4. Summary and Overview of Report

The boundary layer is shown to be more amenable to plasma flow control than inviscid flow. The boundary layer is more easily ionized. MHD interaction parameters are higher in the boundary layer than in the freestream. Also, relatively small changes in the boundary layer may have global effects through viscous interaction and the fluid-dynamic amplification of disturbances in the boundary layer.

There is no doubt that, in principle, boundary layer profiles can be modulated with MHD effects if the interaction parameter is high enough. Obtaining high-enough conductivity for a reasonable interaction parameter is a challenge. The Hall effect places an upper limit on the maximum magnetic field that can be imposed effectively, and creates three-dimensionality. The net payoff of boundary layer control for skin friction and heat transfer remains to be demonstrated. Skin friction and heat transfer reduction from decelerating the boundary layer comes at the cost of reaction drag on the magnet in the vehicle and an unstable velocity profile. Conversely, an accelerated profile that is more stable and produces a propulsive force on the vehicle will increase skin friction and heat transfer. Payoffs in reduced heat transfer and engine operability may offset some of these negatives.

Initial experiments and computations have indicated the potential for controlling boundary layer transition through MHD. Even relatively simple experimental and computational configurations have created surprising results. The boundary layers in MHD flows will be subjected to numerous effects including EHD forces, Joule heating, and three-dimensionality. Extensive and careful computational and experimental work is required to fully understand the complex physics of these flows and to utilize the potential for MHD control to its fullest. Although MHD boundary layer control is certainly possible in principle, complete systems analyses will be required to evaluate its overall practicality.

This report summarizes work carried out in the AFRL/VA Mach 5 Plasma Channel in support of plasma flow control, with special attention to boundary layer control. The Plasma Channel was completed in 2002. Initial work in the channel focused on characterization of the device and diagnostic development. When plasma generation was routine, the next phase of work focused on characterizing plasmas in the flow. After this, attention turned to surface discharges, with and without magnetic fields. Each of these phases is summarized in a separate section of this report.

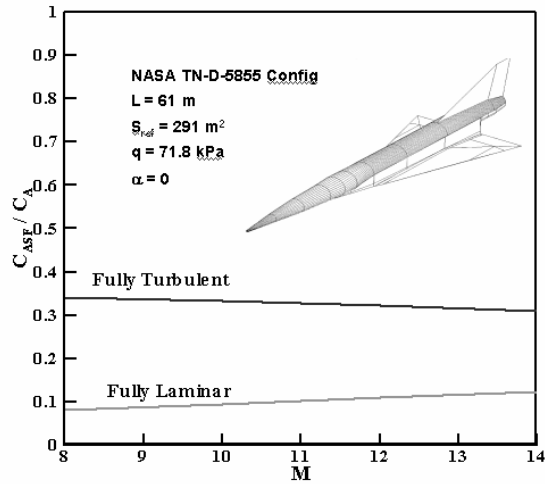


Figure 1 Ratio of axial force due to skin friction to overall axial force for a slender hypersonic configuration.

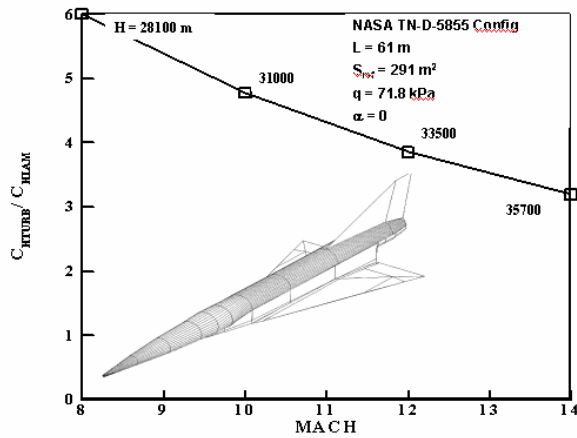


Figure 2 Ratio of integrated laminar to turbulent heat transfer for a hypersonic configuration.

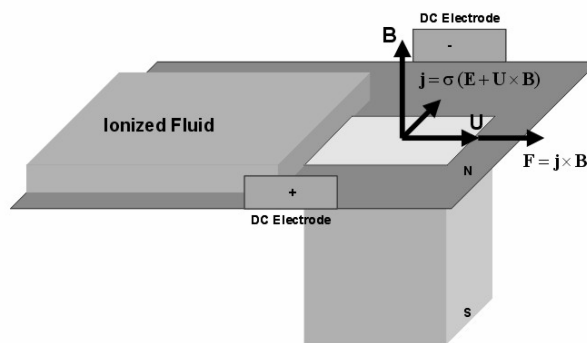


Figure 3 Forces and currents in MHD flow of ionized fluid.

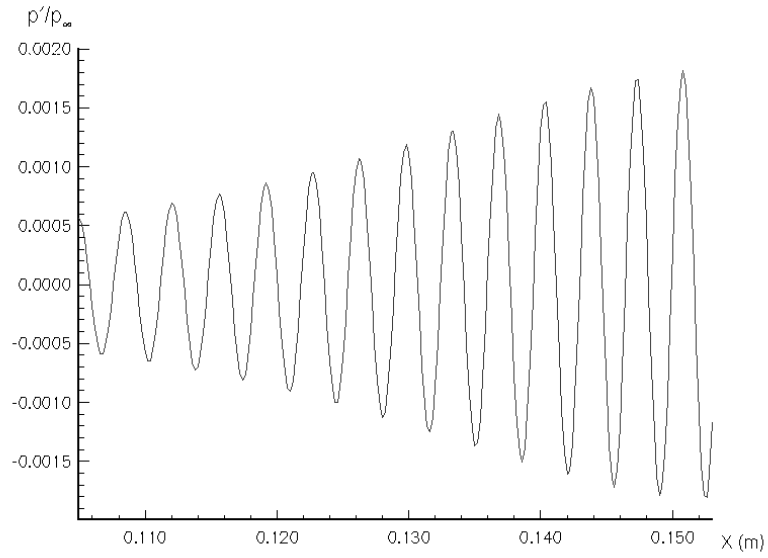


Figure 4 Instantaneous second-mode wall pressure fluctuations in a flat-plate, non-MHD, $M=4.5$ boundary layer (Ref. 32).

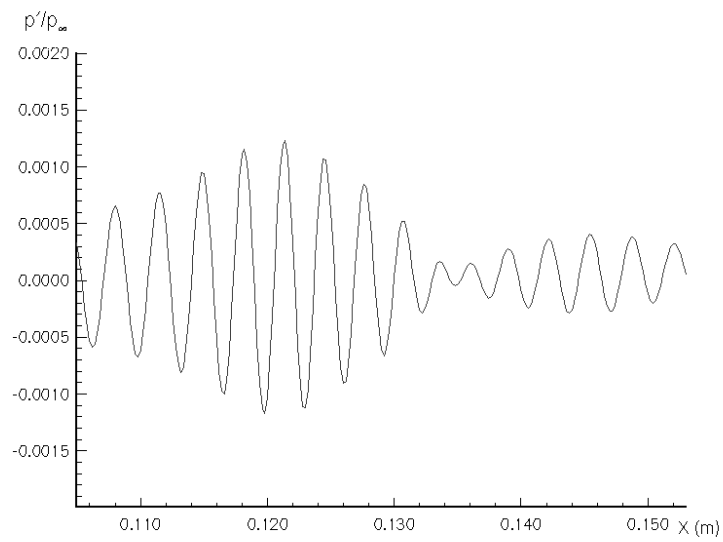


Figure 5 Instantaneous second-mode wall pressure fluctuations in a flat-plate, MHD boundary layer flow through a 1.2 T field, $M=4.5$ (Ref. 32).

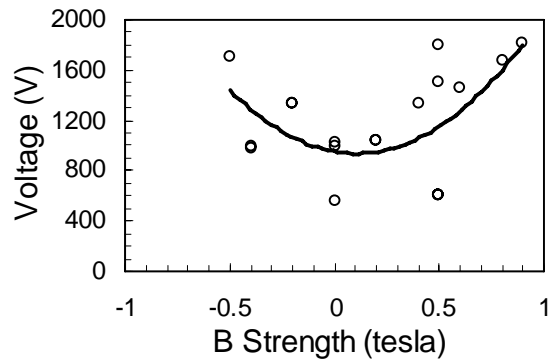


Figure 6 Voltage required to generate a 50 mA discharge as a function of magnetic field strength.

2. Plasma Channel Development and Diagnostics

2.1. Introduction

Plasma aerodynamics is a phenomenologically rich field, offering numerous challenges to computation. Among these are the prediction of gas chemistry, transport properties, electrode boundary conditions, and three-dimensionality introduced either through non-uniformities in the plasmas or through Hall effects. In addition, the usual complications of supersonic and hypersonic flight are present. Although great strides have been made in the computation of plasma aerodynamics, numerical simulations will of necessity be subject to physically simplified scenarios. For this reason, experimental research is crucial to the understanding and application of plasma aerodynamics.

Two mechanisms for creating plasmas in hypervelocity flight are aerodynamic heating and applied electromagnetic fields. In hypervelocity flight, thermal plasmas are created either via compression through shock waves or through constant pressure deceleration in boundary layers. Significant heating is required to generate thermal plasmas, so that they are generally not encountered below about Mach 10 in typical reentry trajectories.²¹ Because of the high temperatures required to generate thermal plasmas, they typically have been simulated in impulse facilities or arc-jets. These facilities present numerous operational challenges, and are relevant only to reentry-velocity flight scenarios. The use of non-equilibrium plasmas offers the ability to create low translational temperature plasmas and to operate at lower Mach numbers.

Initial experimental work on plasma aerodynamic flows in AFRL/VAA began in the Mach 6 High Reynolds Facility.⁵⁶ Research in this facility presented a number of operational difficulties. To facilitate plasma generation, the tunnel was exhausted to vacuum in order to run at the lowest possible stagnation pressure (206 kPa).⁵⁷ Static pressures above about 2 torr created constrictions in DC discharges. Electromagnetic noise from RF plasma discharges interfered with the tunnel stagnation-valve controller, rendering RF plasmas unusable. Also, great care had to be taken to isolate DC electrodes from any unintended ground paths inside the all-metal wind tunnel. A tunnel stagnation temperature of 610 K was required to avoid air liquefaction, which also increased operational problems. These problems provided an impetus to construct a new device designed specifically for magnetoaerodynamic experiments. Prior publications^{23,58,59,60} describe initial shakedown and diagnostic development of the new device, the Mach 5 Plasma Channel. This section describes the design philosophy, construction, and initial results from the channel.

2.2. Design Requirements

Experience in the Mach 6 High Reynolds Facility led to some basic requirements for the new Plasma Channel. These included low-density operation, dielectric construction to avoid unintentional ground paths, and overall simplicity of operation. The requirement for simple operation created an upper bound on the Mach number to obviate the need for a heater. The design Mach was thus fixed at five.

Although some Mach 5 wind tunnels require heating, these are higher pressure tunnels than the Mach 5 Plasma Channel. The onset of air liquefaction is a function of pressure.

Lower pressure delays the onset of liquefaction to lower temperatures. Since the Mach 5 Plasma Channel operates at subatmospheric stagnation pressure, static pressures are low enough to avoid liquefaction,⁶¹ and no heater is required.

To breakdown and sustain the plasma, electrons must be accelerated between collisions to velocities high enough to frequently ionize the collision partner. This immediately implies that low pressures are beneficial in generating a discharge. The minimum in the Paschen curve for air occurs at a value of $pd < 1$ torr-cm.⁶² At high pressure, a DC discharge tends to constrict. In practice, in experiments in the Mach 6 wind tunnel, DC discharges began to constrict at pressures above about 2 torr (at the conditions of the Mach 6 tunnel, equivalent to a number density of about $2.4 \times 10^{17} \text{ cm}^{-3}$).⁶³ With the ratio of stagnation to static density in isentropic flow given by⁶⁴

$$\frac{\rho}{\rho_0} = \left(1 + \frac{\gamma - 1}{2} M^2 \right)^{-\gamma/(\gamma-1)},$$

a static number density of less than $2.4 \times 10^{17} \text{ cm}^{-3}$ at Mach 5 implies that the channel must operate at stagnation pressures less than atmospheric. This also requires that the test section exhaust to vacuum.

The requirement for subatmospheric pressures throughout the channel simplifies material requirements and design. To avoid unintended ground paths, as much of the channel as possible must be constructed of a dielectric. Since the channel would be subjected to no more than one atmosphere of pressure, it could be constructed entirely of acrylic plastic. This construction has the added benefit of providing excellent visual access to the channel.

An overriding concern in magnetoaerodynamic flows, especially in those with non-equilibrium plasmas, is the magnitude of the conductivity. A primary figure of merit for characterizing MHD flows is the interaction parameter, which is the ratio of Lorentz force to inertial forces on a fluid element. The conductivities of typical plasma and electrolyte flows are relatively low. For nonequilibrium ionized air, conductivities are typically on the order of one mho/m.^{22,23,24} At a stagnation pressure of 1.0 atmosphere, a magnetic field of one tesla, and a conductivity of 1 mho/m, the interaction parameter per unit length at Mach 5 is approximately 0.6 m^{-1} . With other parameters fixed, B and L must be maximized. This typically leads to MHD channels with elongated magnets to maximize L , and with walls in close proximity to maximize B .⁴⁰ The challenge in designing the plasma channel is to place the sidewalls in close proximity, but still provide adequate space for an inviscid core.

2.3. Construction of the Channel

The device as constructed is a blow-down, semi-free-jet facility. A rectangular cross-section, conical nozzle with a throat area of 73.7 by 5.08 mm expands to a nozzle exit plane of 73.7 by 177.8 mm. The test section has dimensions of 386.08 by 177.8 by 73.66 mm (length by height by width). Plenums on the top and bottom of the test section provide additional relief. The nozzle boundary layer separates from the nozzle lip at the beginning of the test section, forming a free shear layer, and reattaches at the beginning of the diffuser. The separating shear layer generates weak waves in the test section, but

the plenums greatly simplify the introduction of instrumentation and models into the test section. The entire length of the channel is 1555 mm and it is constructed of Plexiglas.TM Two 235 mm diameter quartz windows were mounted on the side walls of the test section. The windows expose the entire test section, including the nozzle exit plane. A sketch of the plasma channel is presented in Figure 7. Dry air is supplied from the existing high-pressure supply through a three-stage pressure-reduction system. The high-pressure supply capability is not required, but is merely a convenient source of dry air. A manual pressure regulator is used to set the channel stagnation pressure. The tunnel exhausts to a 2800 m³ vacuum sphere. Stagnation temperatures range from 270 K to 280 K depending on ambient conditions and throttling through the pressure reduction system.

The original design goal for the facility was to run at stagnation pressures from 0.1 to 1.0 atmosphere. In practice, the minimum back pressure that can be maintained downstream of the diffuser is approximately 6 torr. At this back pressure, the minimum stagnation pressure to sustain supersonic flow in the channel is 0.4 atm. The freestream Mach number of approximately 5.3 is slightly higher than design. The simulated altitude range (based on static density) of the facility extends from approximately 30,000 to 38,000 meters. At the lowest attainable stagnation pressure of 300 torr, stagnation temperature of 280 K, and a freestream Mach of 5.3, the freestream in the test section has a velocity, density, and temperature of 691 m/s, 0.0044 kg/m³, and 42 K, respectively. Under these conditions the mass-flow rate is less than 0.04 kg/s and the unit Reynolds number in the test section is 1.2×10^6 per meter. The freestream neutral particle number density under these conditions is 10^{17} cm⁻³. Although designed as a blow-down system, continuous operation can be easily sustained through continuous operation of the vacuum pump system. A photograph of the plasma channel is shown in Figure 8.

2.4. Subsystems and Aerodynamic Instrumentation

Plasma sources and magnets had to be acquired to complete the channel. In addition, conventional aerodynamic instrumentation as well as specialized plasma instrumentation had to be developed or acquired. This section describes plasma sources, magnets and conventional aerodynamic instrumentation. Microwave absorption and optical emission spectroscopy plasma diagnostics developed specifically for the plasma channel are described in subsequent sections. Langmuir probe development began during initial Mach 6 testing and was further refined during the plasma channel development. Some limited Langmuir probe data are presented along with the emission spectroscopy results.

A number of options are available for plasma generation. These include DC discharges, capacitively coupled RF discharges, inductively coupled RF discharges, microwave, and electron-beams, among others. Power sources for DC and RF discharges were available from the previous Mach 6 experiments. These had proved satisfactory in generating diffuse discharges in the Mach 6 experiments. DC discharges have the added advantage of having been well studied and accessible to analysis. In the current work all DC discharges were created with a Universal Voltronics reversible polarity switching power unit. It is rated at 8 kW with 10 kV and 800 mA output. Since the emphasis in the current work migrated from large-volume discharges to smaller, surface discharges, the work in this report was performed with DC discharges. RF discharges were successfully

created in the plasma channel, but were not used for any quantitative experiments since they proved very diffuse and their energy input could not be localized.

The initial concept for the magnet system consisted of a pair of air-core solenoids on opposite sides of the channel. A small solenoid with a pulsed power supply was wound for the Mach 6 experiments, and this system was capable of generating a field of up to 2 tesla.⁵⁷ The pulsed air-core solenoid concept for the Mach 5 channel was abandoned because of the difficulty in achieving a tuned circuit, due to the large impedance and inductance of the coils. The pulsed system presented other disadvantages due to the complexity of the power source and the short duration of the magnet field, which complicated diagnostics. A superconductor magnet was briefly considered. The superconductor offered the potential of high magnetic fields, but this concept was also abandoned due to the cost and complexity of the system. The final choice of magnet was a commercially available, large laboratory electromagnet.

The GMW 3474 electromagnet is a continuous-operation, water-cooled model. The coils, when connected in series, have a maximum power rating of 10.6 kW (140 amp, 76 Volts). Pole-spacing is adjustable from 0 to 160 mm, and pole-cap diameters range from 25 to 250 mm. Field strength is a function of pole gap and pole cap diameter. For a fixed pole cap diameter, field strength diminishes as the pole gap increases. For sufficiently small pole gaps, smaller pole cap diameters create a higher field. As the pole gap approaches the pole cap diameter, field uniformity is adversely affected. With a pole gap of 10 mm and a pole diameter of 25 mm, the field strength is as high as 3.5 tesla. In practice, the magnet for the plasma channel is always operated at the maximum pole spacing and pole-cap diameter to clear the channel sidewalls. Under these conditions, the transverse magnetic field has a magnitude of one tesla and is nearly uniform. The magnet is rail mounted so that it may be moved downstream to access the test section.

The capability for continuous operation of the electromagnet is a distinct advantage, especially given the ability for continuous tunnel operation. One drawback of the magnet is that it impedes visual access to the channel. This problem was alleviated by acquiring pole faces with 2 inch diameter through holes for visualization. The spacing of these poles could not be adjusted, but since the magnet was always operated with the poles at maximum spacing, this was not a detriment. Field uniformity was not affected within the resolution of the Teslameter (GMW DTM-133-DG) used to measure it.

A 3D traverse mechanism was developed for surveys. The placement of the traverse is controllable within a distance of 0.25 mm. All Pitot data were collected with a single pressure transducer. The Baratron MKS model 722-A-23320 absolute pressure gauge has a calibrated accuracy of +/- 1 0.1 percent of the 100 torr full range. Surface static pressure measurements were made with MKS Baratron pressure transducers with a 0 to 2 torr range. The manufacturer's stated accuracy of these transducers is +/-0.5 percent of the reading.

Schlieren flow visualization is an important baseline method for flow visualization. The application of schlieren imaging to low-density plasma flows presents special challenges, however. High sensitivity is required to image gradients in low-density flow. The plasma glow must also be rejected or otherwise dealt with. In addition, time-resolution is required to freeze unsteady phenomena. A high-sensitivity schlieren system was

developed especially for the plasma channel. The basis of the system was two 2540 mm focal length, gold-coated parabolic mirrors. Three pulsed light sources--LED, Xenon Corp. Nanopulser, and laser breakdown--were tested on identical flowfields. The results showed that a simple LED can provide excellent illumination, with pulse durations ranging from microseconds to continuous. The Nanopulser provides excellent, short-duration images, although illumination varies from shot-to-shot. Laser-breakdown provides short-duration, incoherent illumination that is constant from pulse-to-pulse. Details of the schlieren system and light sources are presented in a prior publication.⁶⁵

2.5. Tunnel Calibration

The primary concerns regarding flow quality in the channel were the uniformity of the flow arising from the conical nozzle, and the thickness of the sidewall boundary layers. Extensive Pitot surveys were conducted to assess flow uniformity and the extent of the inviscid core.

A first measure of flow uniformity is the Pitot pressure measured along the tunnel centerline, as shown in Figure 9. The Pitot pressures show some gradients for 2 cm downstream of the nozzle exit, then are uniform to within 4 percent for the next 8 cm. Assuming isentropic expansion from the stagnation chamber, this Pitot pressure variation corresponds to a Mach number variation of 5.35 to 5.30, or less than 1 percent. At 10 cm downstream of the nozzle exit, the wave structure from the nozzle lip crosses the centerline, causing the Pitot pressure to increase downstream of this location.

Pitot surveys in the vertical direction on the tunnel centerline at three axial stations are shown in Figure 10. The weak compression wave from the nozzle lip is evident even at the first survey station at $z = \pm 6$ cm, indicating that the nozzle boundary layer separates slightly upstream of the nozzle lip. The wave propagates deeper into the channel core flow at succeeding x -stations, eroding the area of uniform flow. Beneath the wave from the nozzle lip, the shear layer from the nozzle wall is evident. This shear layer is only about 1 cm thick at the two most upstream measuring stations. At the two most upstream measuring stations, the Pitot pressures are uniform to within 2.5 percent for $-5 < z < 5$ cm.

Spanwise Pitot surveys were conducted at three axial stations ($x=0.0, 5.1, \text{ and } 10.2$ cm), at three vertical locations ($z=-2.8, 0.0, 2.8$ cm), for a total of nine surveys. These surveys are shown in Figures 11 to -13. At each axial station the surveys are very similar at each vertical location, but nonuniform in the spanwise dimension. The sidewall boundary layer is evident and thickens as x increases. The Pitot pressures show an unexpected rise from the centerline to the edge of the shear layer, before they drop off in the shear layer. The source of this rise is presumed to be a compression wave system from the tunnel sidewalls. The source of these waves is unknown, but may be due to nonuniform boundary layer growth on the sidewalls, which is a common occurrence in rectangular cross-section wind tunnels.

In summary, the channel flow is remarkably free from gradients in the streamwise and vertical directions, but suffers from some degree of non-uniformity in the spanwise direction.

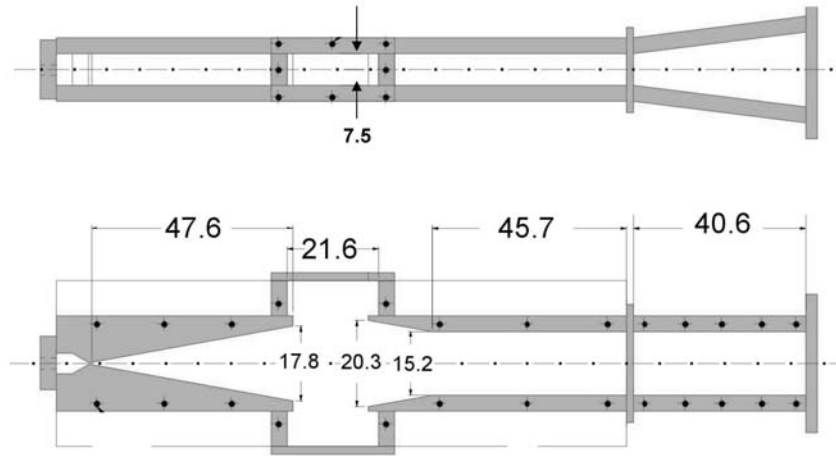


Figure 7 Schematic of the plasma channel. All dimensions centimeters. Flow is from left-to-right

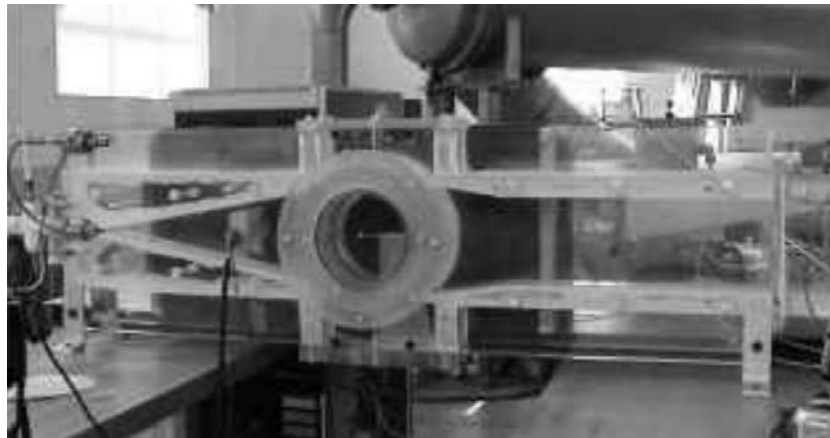


Figure 8 Photograph of the Mach 5 Plasma Channel.

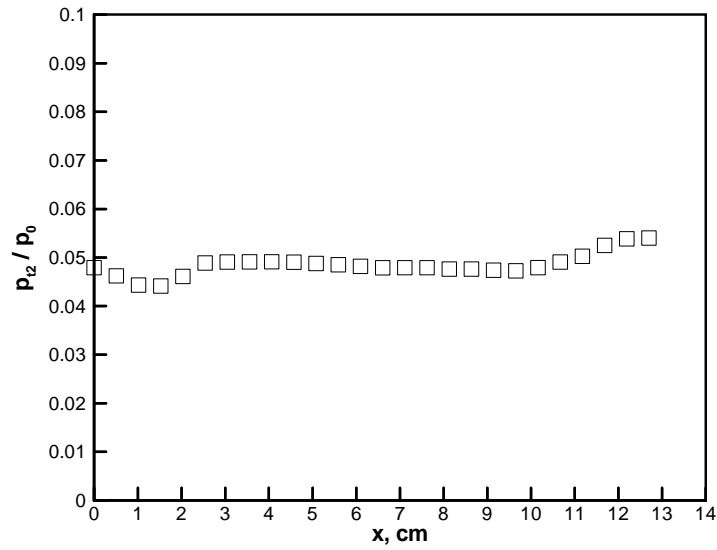


Figure 9 Ratio of Pitot to stagnation pressure along channel centerline. $x = 0$ corresponds to the nozzle exit.

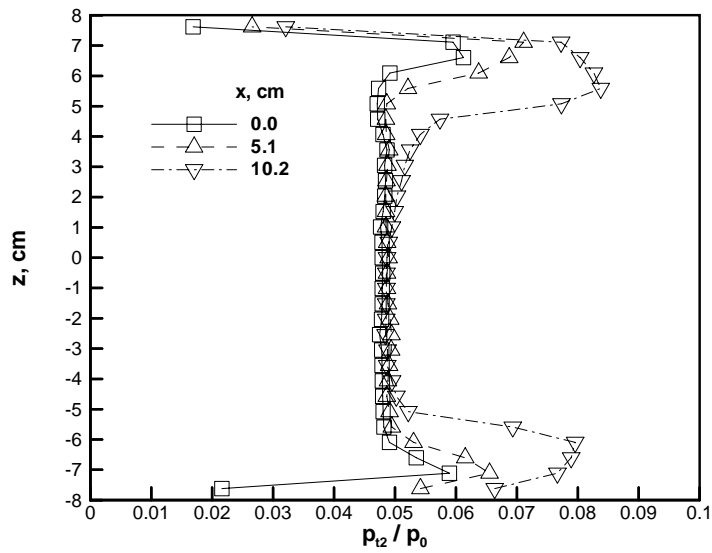


Figure 10 Vertical survey of Pitot pressure, normalized by stagnation pressure, at three axial stations.

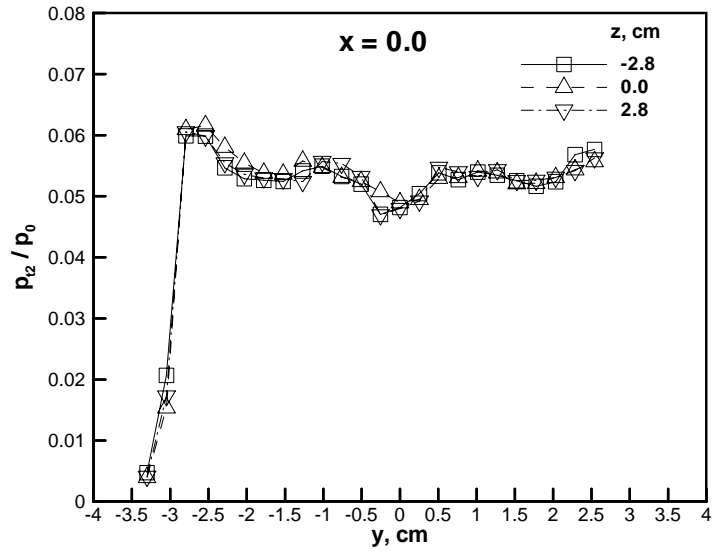


Figure 11 Pitot survey in spanwise direction at three vertical locations, $x=0$.

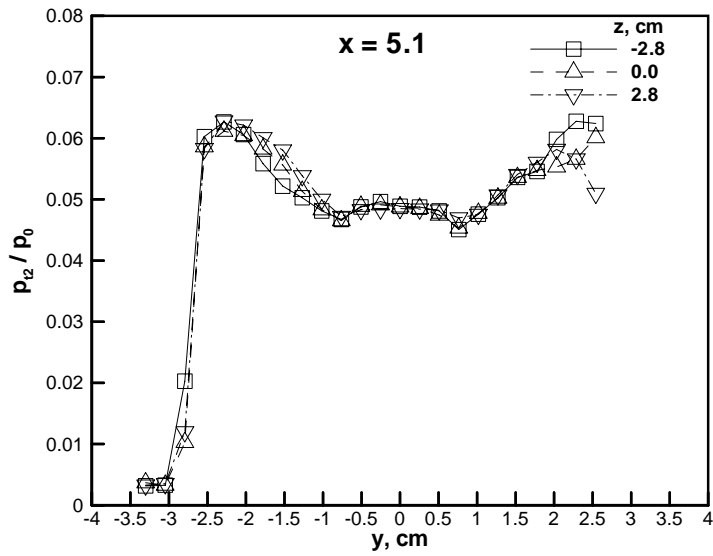


Figure 12 Pitot survey in spanwise direction at three vertical locations, $x=5.1$ cm.

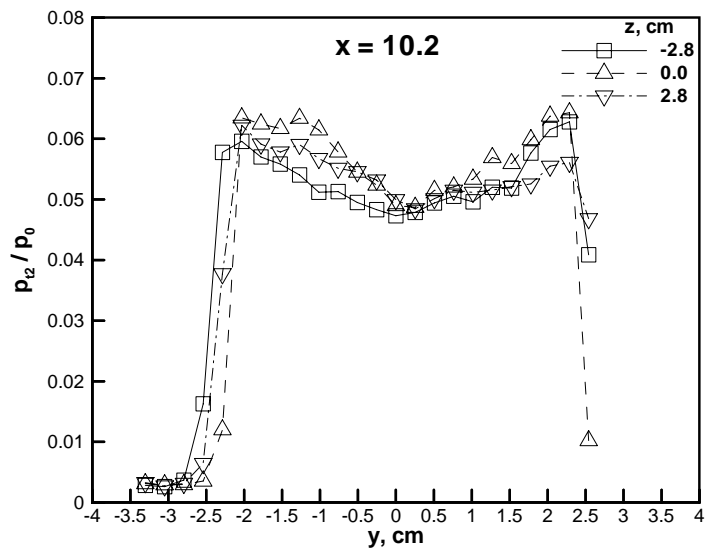


Figure 13 Pitot survey in spanwise direction at three vertical locations, $x=5.1$ cm.

3. Microwave Instrumentation

3.1. Introduction

Microwave absorption is one of the main methods used to determine electron number densities in weakly ionized plasmas generated in a hypersonic or supersonic flow. An advantage of this type of measurement technique is that it is nonintrusive. All the equipment required to make this measurement can be placed outside the flow field. Only microwave energy passes through the flow.

One method of determining the electron number density of a plasma with microwave diagnostics is to determine the amount of microwave energy absorbed by the plasma, relative to the amount of microwave energy incident on the plasma^{66,67}. This can be done by making a measurement of the microwave beam passing from the transmitting horn to the receiving horn with no plasma in the intervening space. This amount of energy will be called P_{inc} . Another measurement is then made with the microwave system in the same configuration, with the same settings, and the plasma discharge operating. This energy measurement will be called P_{trans} . The amount of microwave energy absorbed is then found from

$$P_{abs} = P_{inc} - P_{trans} \quad (1)$$

Another technique for making electron number density measurements with a microwave system is to determine the phase shift of the microwave beam when it passes through the plasma. A third technique used to garner information about the plasma using microwaves is scattering measurements.⁶⁷ This report deals only with the absorption technique of determining the electron number density with a microwave system.

A problem that has been encountered while making microwave absorption measurements on certain types of plasma discharges is that P_{trans} is larger than P_{inc} . This means that the plasma is somehow modifying the microwave beam so that more energy is collected by the receiving horn than the case when the plasma is turned off. This problem will be called negative absorption. This problem is not unique to the measurement that the authors have made; Ref. 66 also discusses this problem. Ref. 66 states that the microwave signal may increase when the plasma is much thinner than the wavelength of the microwave energy or the plasma overall volume is much smaller than the microwave beam. The problems encountered when making these types of microwave measurements are discussed in Section 3.3. Prior to Section 3.3 the equipment and data reduction procedures are presented. Finally, number density results are given.

The output from both the reflected and transmitted power detector is a voltage. This voltage is read with a Lecroy 9384CTM1 digital oscilloscope. A simple voltmeter could be used, but the oscilloscope permits a time averaged reading. This is important because there is some drift in the microwave system itself and the plasma discharges through which microwave measurements are being made fluctuate to some extent. Most of the measured data shown in this paper were averaged over a time period of 3 to 6 seconds.

A 4.6 m long, semi-rigid cable delivered microwave power from the microwave generator to the transmitting horn. The same type and length of cable connected the receiving horn to the transmitted power detector. The system used two different sets of

horns. One set of horns covered the X-band, 8.2 to 12.4 GHz, and the other set covered the Ku band, 12.4 to 18 GHz. Since the microwave system being used is only capable of operation from 10 GHz, the coverage of the 8.2 to 10 GHz range by the X-band horns was not important. The X-band horns have a 7.4 by 8.9 cm rectangular opening, and the Ku-band horns have a 15.0 by 15.2 cm opening. Beam shape measurements showed that the Ku-band horns collimate the microwave beam better than the X-band horns. Wave guides connected the horns to the semi-rigid cables. Different wave guides were used for the X-band and the Ku-band. Microwave measurements were made with the horns were attached to the wave guides and with the wave guides only.

A picture of one of the Ku-band horns and one of the X-band is given in Figure 15. The wooden block attached to each horn is used for holding the horns in a translator mechanism that can be slid along an optical guide. The optical guide allowed accurate positioning of the horns along a single axis. This aspect of the optical guide was important in the data acquisition process. Figure 15 shows the X-band horns positioned to make a measurement through a plasma discharge in the Mach 5 channel.

A number of electrodes and discharge configurations were tested. A detailed explanation and pictures of many of these discharges can be found in Menart et al.⁵⁸ For the first measurements made, the discharge was located in the boundary layers of the wind tunnel. This discharge was generated between two round, flat stainless steel disk electrodes located just outside of the flow region on the bottom and top of the wind tunnel. Most of the measured results presented in this paper were made on plasma discharges that looked like those shown in Figure 17 and Figure 18. The electrodes were either two 0.32 cm diameter steel rods placed into the core of the flow separated by 5.1 cm or two similar rods with 0.6 to 1 cm wide by 4.3 cm long flat plates (shoes) attached to the rod ends and directed in the up or downstream direction. These will be called the shoe electrodes, and they also had an electrode gap of 5.1 cm. The reason a number of different electrode configurations were used for the data presented in the Section 3.3 is that these data were obtained while efforts were being made to enlarge the plasma and reduce the strength of the shock coming off the electrodes. The flow-on electron number density data shown in 3.4 were all taken with upstream pointing, shoe electrodes. These discharges are shown Figure 17 and Figure 18 with the flow on. The Figure 17 discharge is at a low discharge current, and the Figure 18 discharge is at a high discharge current. The no flow discharge results were all taken on a glow discharge that only had luminous portions close to the electrodes.

3.2. Data Reduction Procedure

The data reduction procedure utilized to convert the microwave measurements to electron number densities is developed from the Equation of motion of a single electron moving in a continuous, uniform plasma subject to an applied sinusoidal, electric field:⁶⁸

$$m \frac{d^2 \vec{r}}{dt^2} = -e \vec{E} - \nu m \frac{d \vec{r}}{dt}. \quad (2)$$

There are a number of assumptions involved in this Equation in addition to the conditions stated above. It is assumed that electrons interact with each other only through collective space charge forces, ion and neutral particles are a background medium that only

interacts with the electrons through what can be considered a viscous damping term, the thermal motion of the electrons is much less than the speed of light but large relative to the velocities imparted by the electric field, the collision frequency is independent of the electron speed, and the effects of the magnetic field are ignored. The solution of Eqn. (2) is

$$\vec{r} = -\frac{e\vec{E}}{m\omega} \frac{(\omega + i\nu)}{(\omega^2 + \nu^2)}. \quad (3)$$

The complex conductivity of the plasma at a given frequency is

$$\sigma = -\frac{ne \frac{dr}{dt}}{E} = \frac{ne^2}{m} \frac{(\nu - i\omega)}{(\omega^2 + \nu^2)}. \quad (4)$$

The complex dielectric constant for a linear medium can be written as

$$\kappa = \kappa_r - i\kappa_i = 1 - i \frac{\sigma}{\epsilon_o \omega} = 1 - \frac{\omega_p^2}{\omega} \frac{(\omega + i\nu)}{(\omega^2 + \nu^2)}, \quad (5)$$

where

$$\omega_p = \sqrt{\frac{ne^2}{m\epsilon_o}}, \quad (6)$$

is the natural plasma frequency. Since the complex refractive index

$$\mu = \mu_r - i\chi \quad (7)$$

is obtained by taking the square root of the dielectric constant

$$\mu = \sqrt{\kappa} \quad (8)$$

the attenuation index (imaginary part of the refractive index) can be written as

$$\chi = \left\{ \begin{array}{l} \left[-\frac{1}{2} \left(1 - \frac{\left(\frac{\omega_p}{\omega}\right)^2}{1 + \left(\frac{\nu}{\omega}\right)^2} \right) \right]^{\frac{1}{2}} \\ + \frac{1}{2} \left[\left(1 - \frac{\left(\frac{\omega_p}{\omega}\right)^2}{1 + \left(\frac{\nu}{\omega}\right)^2} \right)^2 + \left(\frac{\left(\frac{\omega_p}{\omega}\right)^2}{1 + \left(\frac{\nu}{\omega}\right)^2} \left(\frac{\nu}{\omega}\right) \right)^2 \right]^{\frac{1}{2}} \end{array} \right\}. \quad (9)$$

The imaginary refractive index is required to obtain the absorption of the microwave beam by the plasma

$$\frac{P_{abs}}{P_{inc}} = \exp\left(-\frac{\omega\chi d}{c}\right). \quad (10)$$

This is the same Equation used by Blevins et al.⁶⁹, Frederick et al.,⁷⁰ and Funaki et al.⁷¹

Another data reduction Equation used for obtaining electron number density values from the amount of microwave energy absorbed is^{62,72}:

$$n_e = \frac{mc\epsilon_0}{e^2} \nu \frac{P_{abs}}{P_{inc}} \frac{1}{d}. \quad (11)$$

This Equation is an approximation of Eqns. (9) and (10) in the limit of small absorption and where $\nu \gg \omega$.

Plots of Eqn. (11) and Eqn. (10) are given in Figure 19 and Figure 20 for a microwave frequency of 10 GHz. This is the frequency at which most of the data in this paper were taken. Figure 19 shows the full range of absorption values while Figure 20 only shows those values less than 0.1. For the most part, weakly ionized plasmas produce absorption values less than 0.1. Figure 19 shows that collisions cause the absorption curve to flatten out from a vertical line. If it were not for collisions the microwave absorption technique would only be capable of measuring a very narrow range of number densities. Results from Eqn. (11) are only shown in Figure 20. From this figure it can be seen that Eqn. (10) gives better results at higher collisional frequencies, but at collisional frequencies less than 10^{10} Hz Eqn. (11) starts to predict the wrong trends in the absorption as a function of collision frequency. Note that in Figure 8 the 10^8 Hz collision frequency line is plotted, but does not show up on the scale chosen.

One of the drawbacks of using Eqn. (10) or Eqn. (11) to determine the electron number density is that there are two unknowns, electron number density and collision frequency. In order to use either of these Equations some estimate of the electron collision frequency must be made. Reasonable estimates of this number can be made from published data⁷³. For this work a collision frequency of 1.7×10^{10} Hz is used for discharge currents below 100 mA and 4.2×10^9 Hz is used for discharge currents at or above 100 mA. At 100 mA the discharge tends to convert from a glow discharge to a combination between a glow and arc-like discharge.

Another quantity required to solve Eqn. (10) or (11) is the depth of the plasma. In this work the no flow discharges generally filled the width of the wind tunnel with plasma, thus 7 cm was used for d . For the flow-on cases, the discharges were taken to be the width of the electrodes.

3.3. Problems Encountered

The first microwave system measurements were made with on a discharge that occurred in the tunnel boundary layer. Many of the microwave measurements made on this boundary layer discharge resulted in what the authors will call negative absorption. Negative absorption occurs when the microwave energy sensed by the receiving horn is larger when the plasma is turned on as compared to when it is off. This renders the microwave diagnostic tool useless for determining electron number densities. This did not happen for all boundary layer plasma measurements, but it happened for many of them.

Microwave energy measurements with the plasma off and with the plasma on, utilizing a boundary layer type plasma, are shown in Figure 21. There are three pairs of curves on this graph. One set of curves was obtained using the X-band horns, another set was obtained using the Ku-band horns, and the third set was obtained using the X-band wave guides with no horns attached. The horizontal axis on this graph represents the distance between the openings of the transmitting horn or wave guide and the receiving horn or wave guide normalized by the microwave wavelength. The vertical axis is the power at the receiving horn or wave guide. Figure 21 shows that the energy transmitted through the plasma is almost equal to the plasma-off energy. This means there is no absorption or very little absorption. In many cases the signal is greater with the plasma on than with the plasma off. This means that the plasma actually increased the microwave energy measured at the detector.

The other interesting observation from the Figure 21 data is that the received power is periodic with the separation distance. The period is 0.5 wavelength of the microwave signal. The largest percentage oscillation is seen with the Ku-band horns operating at 18 GHz. This oscillation is seen better in Figure 22 for three different frequencies with only air between the transmitting and receiving horns. A separation of zero wavelengths means that the horns are touching. Both the 15 and 18 GHz data use the Ku-band horns, and the 10 GHz data use the X-band horns. The data taken with the Ku-band horns has oscillations that approach zero every half wavelength. The X-band horns operating at 10 GHz have much less oscillation.

The data in Figure 22 also indicate that the Ku-band horns collimate the microwave beam better than the X-band horns. This is indicated by the drop of the wavelength-averaged signal with horn separation. It is very small with the Ku-band horns and very noticeable with the X-band horns.

It is not completely understood why in some cases the detected microwave power increases when the plasma is turned on. The oscillations in the data shown in Figure 21 and Figure 22 repeat themselves every half wavelength within the accuracy of the measurements taken. Most of the microwave separation data in this paper was taken every 1mm. These oscillations occur whether a plasma is present or not; however, the presence of the plasma may alter this interference phenomenon and produce a larger signal with the plasma on⁶⁶. Another possible cause for this increased signal with the plasma on is that the plasma focuses the microwave beam in some manner. Diffraction or refraction or some other scattering phenomenon may do this.

Plasma-off and plasma-on runs were made immediately after each other to avoid drift or other spurious time-dependent phenomena. The plasma-off measurement took about 3 to 6 seconds and the plasma-on measurement took about 3 to 6 seconds. The measurement time could have been shorter, but averaging the readings over a period of seconds is desirable due to the random fluctuations present in the plasma discharge. Because the plasma-on and plasma-off measurement were taken within a period of 12 seconds, with no other changes made, differences in the two measurements should be due to the plasma alone.

Operating under the assumption that the negative absorption was due to modification of the interference effects by the plasma, efforts were made to reduce interference. One way

to minimize interference was to utilize the X-band horns instead of the Ku-band horns. Figure 21 and Figure 22 show that interference effects at 18 GHz bring the microwave signal close to zero every half wavelength in horn spacing. At 10 GHz the interference patterns are still seen, but they are a much smaller percentage of the total signal. Data taken using the wave guides alone at 10 GHz do not show as severe an interference pattern as the Ku-band horns, but the overall signal is much lower than the X-band horn signal. For these reasons it was decided to use the X-band horns.

Figure 23 measurements were made on a core-flow plasma. The Ku-band horns were not used because of the oscillatory behavior seen in Figure 21 and Figure 22. Like Figure 21, it is difficult to see when the plasma-on measurement is larger than the plasma-off measurement. Although at some points in Figure 11 the plasma-on measurement is larger than the plasma-off measurement, these points are fewer than for the boundary layer plasma. These results indicate that the shape of the plasma influences whether negative absorption is seen. A possible explanation for this is that the core flow plasma produces a larger volume of plasma. This could reduce diffraction effects and increase the overall absorption of the microwave beam. A larger absorption would tend to hide any focusing or interference effects of the plasma.

Another source of negative absorption is seen in Figure 23; that is a phase shift. A phase shift misaligns the plasma-on measurements relative to the plasma-off measurements. Data in Figure 23 indicate that the phase shift must be less than 0.034 wavelengths. This corresponds to a 1 mm distance. The data in Figure 23 were taken in 1 mm intervals. One way to reduce phase shift effects is to lessen interference.

In addition to using the X-band horns instead of the Ku-band horns, a method to minimize the interference⁷⁴ was to put absorbing material between the X-band horns. A number of different absorbing pad locations were tried. These were a pad covering the transmitting horn, a pad covering the receiving horn, a pad covering the receiving horn and another pad covering the transmitting horn, two absorption pads covering the transmitting horn, and no absorption pad. The absorbing pads were made of 0.95 cm thick Eccosorb AN-73. The data obtained for various absorbing pad locations are shown in Figure 24 for the plasma-off case. The minimum oscillation is obtained with the absorbing pad over the transmitting horn. It is interesting to note that an absorbing pad over the receiving horn does not have as large an effect compared to an absorbing pad on the transmitting horn. It appears that two absorbing pads covering the transmitting horn is no improvement over one. The overall signal is reduced, but the percentage amplitude fluctuations remain the same.

One additional problem with making microwave measurements on plasmas discharges whose surface area is smaller than that of the microwave beam is obtaining the proper value of the incident energy. The P_{inc} value in both Eqns. (10) and (11) should only be the microwave energy incident on the plasma, not the microwave energy going around the plasma. An attempt was made to minimize this effect by placing a 0.95 cm thick Eccosorb AN-73 absorbing pad with a 2.5 cm square hole in the center over the receiving horn.

Figure 25 shows the behavior of an absorbing pad on the transmitting horn and an absorbing pad with a 2.5 cm square hole on the receiving horn, compared to the case with

no absorbing material and the case with one absorbing pad on the transmitting horn. The hole configuration case has slightly larger oscillations than the absorbing pad on the transmitting horn case.

The configuration of choice for making microwave measurements on small discharges was the two X-band horns operating at 10 GHz with one absorbing pad completely covering the opening of the transmitting horn and another absorbing pad with a 2.5 cm square hole covering the receiving horn. Plasma-on and plasma-off data for this configuration are shown in Figure 26. No negative absorption was observed; however, the separation distance of the horns affects the absorption measurement. Since the amount of absorption varies over one-half wavelength of separation distance, data are taken at three or more horn separations around the peak of one of the oscillations. In the measurements to be shown, electron number densities are calculated at each of these separation distances and their average is presented.

3.4. Results

Electron number densities measured by the microwave system are shown in Figure 27 - Figure 29. Figure 27 shows number densities measured in a no flow glow discharge. Results were obtained using the preferred horn and absorbing pad configuration described above. The correspondence between the 10 and 12 GHz data is good, except for the 50 mA case. Figure 28 also shows good agreement between the 10 and 12 GHz microwave signals for flow-on.

Electron number densities for the no flow case are a strong function of the current, varying by over an order of magnitude for a four-fold increase in discharge current (see Figure 27). For the flow-on case the electron number densities are a much weaker function of discharge current for a current range from 100 to 600 mA. There is only one current where the flow and no-flow data overlap, 100 mA. The no-flow number density falls within the flow-on data spread.

Figure 29 shows the effect of electrode configuration. Thin and wide shoe electrodes with uncovered tips produce similar results. When the tip of the wide shoe is uncovered number densities decrease. Normally the tip of the cathode electrode was covered with a dielectric paint to keep it from conducting current into the discharge. This helped keep the discharge from constricting for currents around 100 mA. At higher currents the discharge changed to a glow with arc-like regions whether the tip was covered or not. The data in Figure 29 indicates a change in the discharge between the covered and uncovered tip cases.

3.5. Summary

When making microwave absorption measurements in small plasma discharges care must be taken, and even then accuracy will be limited. In certain situations negative absorption can be seen. When this occurs the microwave measurements are useless for determining the electron number density of the plasma. Even when this does not happen, the problems encountered in this study may decrease the accuracy of the electron number density.

A number of techniques were examined for minimizing the effects of negative absorption. The first is that interference between the transmitting horn and the receiving

horn should be minimized. One technique employed in this study to use the X-band horns instead of the Ku-band horns and to operate in the X-band frequency range. Further improvements were made by placing a 0.95 cm thick sheet of Eccosorb AN-73 absorbing material over the entire opening of the transmitting horn. Placing this absorbing pad over the transmitting horn produced better results than placing it over the receiving horn. Another sheet of Eccosorb AN-73 absorbing material with a 2.5 cm square hole cut into it was placed over the opening of the receiving horn. To minimize interference effects, it is also recommended that data be taken at several horn separations around one of the interference maxima, an electron number density be calculated for each one of these points, and then these values averaged to obtain the best estimate of the microwave number density.

Data were taken using a microwave frequency of 10 GHz and a microwave frequency of 12 GHz. In general the 12 GHz measurements predict slightly lower electron number densities than the 10 GHz measurements, but the difference is insignificant given the number of uncertainties involved in these measurements. In general the electron number density increases with current for the flow-on and the flow-off cases. The no flow number densities for a 100 mA discharge current are essentially the same as those with the flow on.

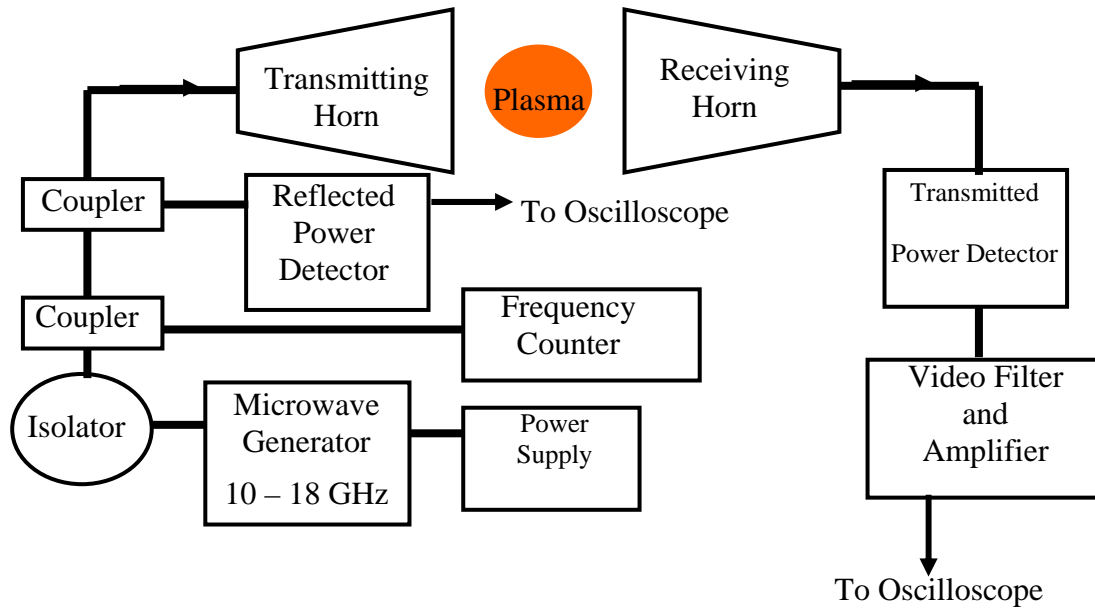


Figure 14 Schematic of microwave diagnostic system.

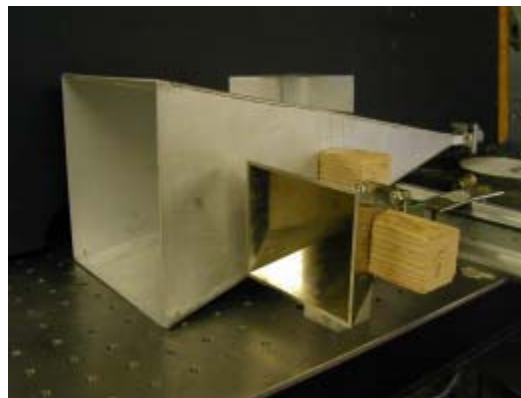


Figure 15 Ku-band horn and wave guide (back) and X-band horn and wave guide (front).

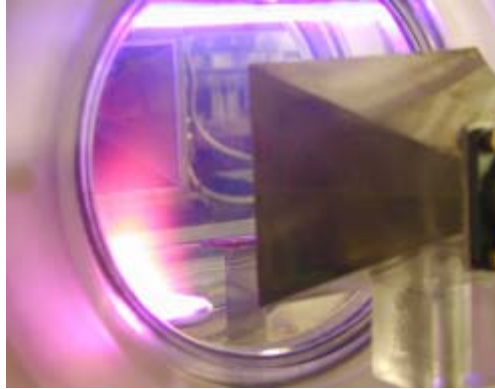


Figure 16 X-band horns in operation on Mach 5 wind tunnel with a plasma discharge.

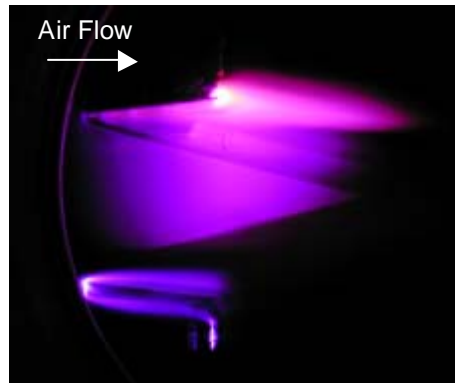


Figure 17 Front view of a 100 mA DC discharge generated with upstream pointing, shoed electrodes.

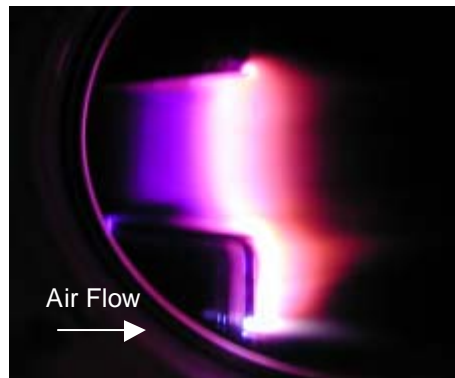


Figure 18 Front view of a 500 mA DC discharge generated with upstream pointing, shoed electrodes.

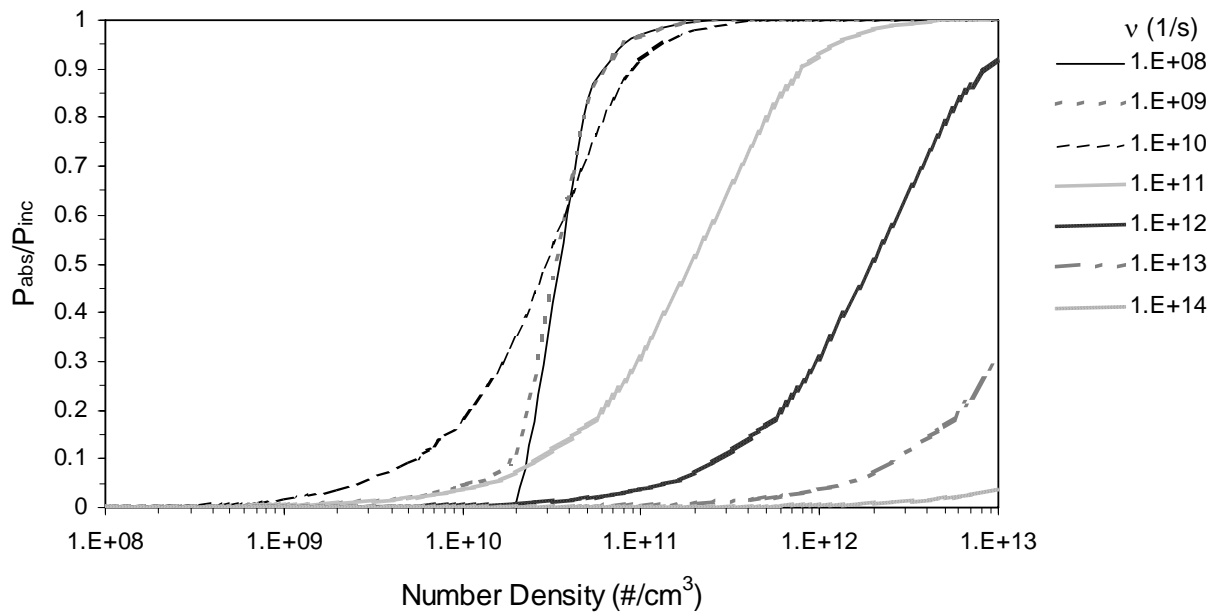


Figure 19 Absorption of microwave power as a function of electron number density and collision frequency for a microwave beam at 10 GHz and a path length of 7 cm. The full range of absorption values are shown for Eqn. (10).

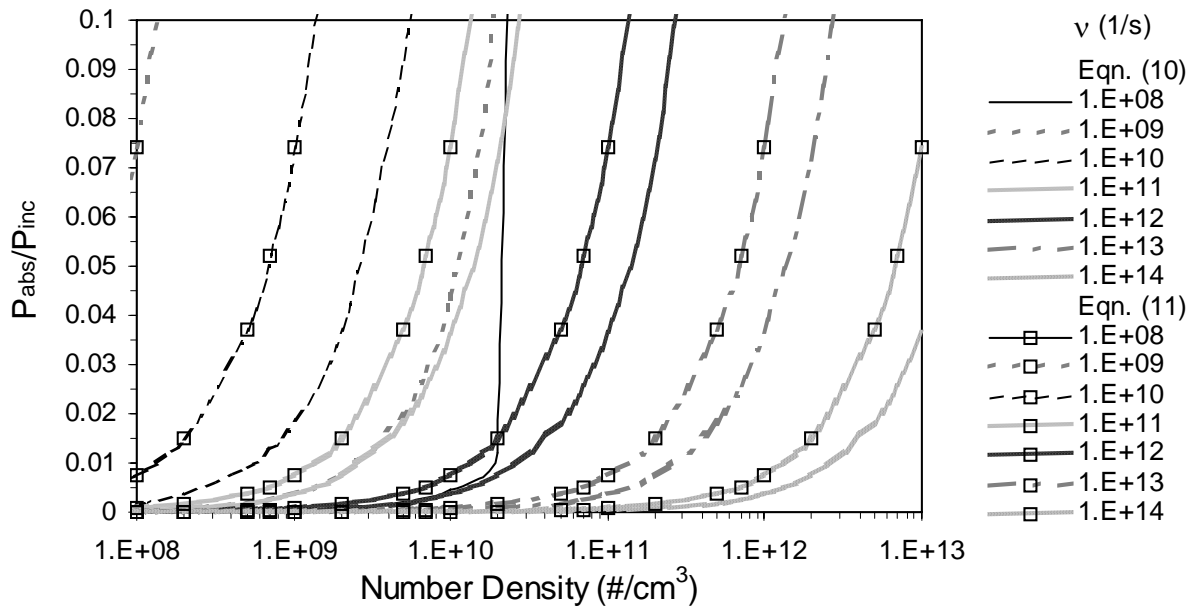


Figure 20 Absorption of microwave power as a function of electron number density and collision frequency for a microwave beam at 10 GHz and a path length of 7 cm. The full range of absorption values are shown for Eqn. (10).

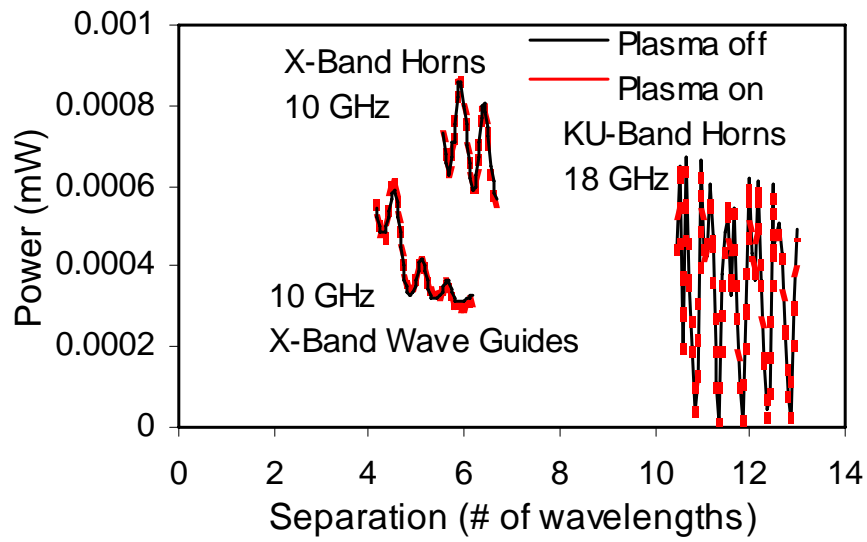


Figure 21 Transmitted microwave power through a boundary layer plasma and with no plasma as a function of the separation between the horns or wave guides.

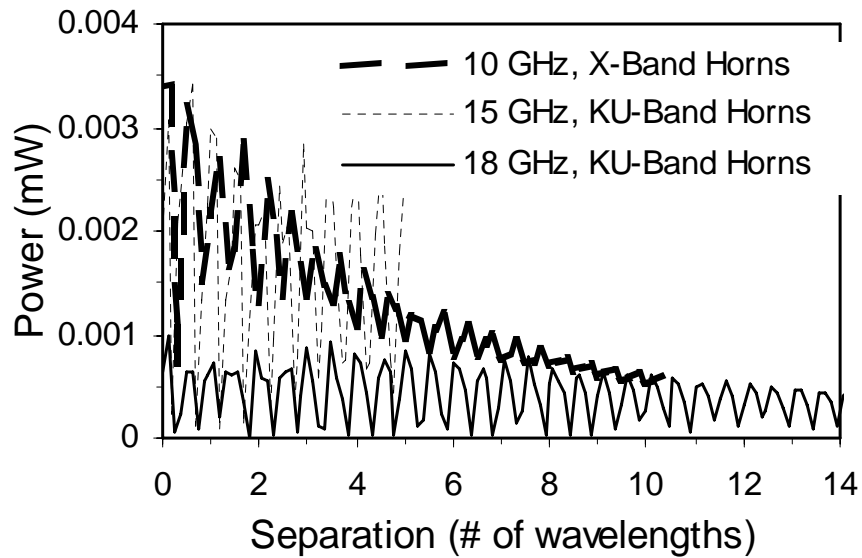


Figure 22 Interference pattern of a transmitted microwave beam as a function of separation distance between the horns with no plasma.

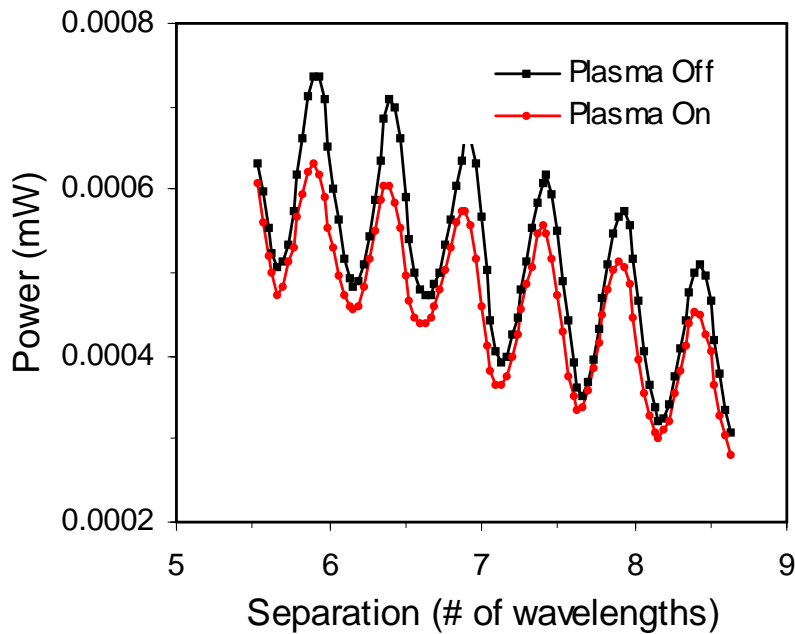


Figure 23 Transmitted 10 GHz microwave power as a function of the separation between the X-band horns with the plasma off and the plasma on. The plasma discharge is a core flow plasma.

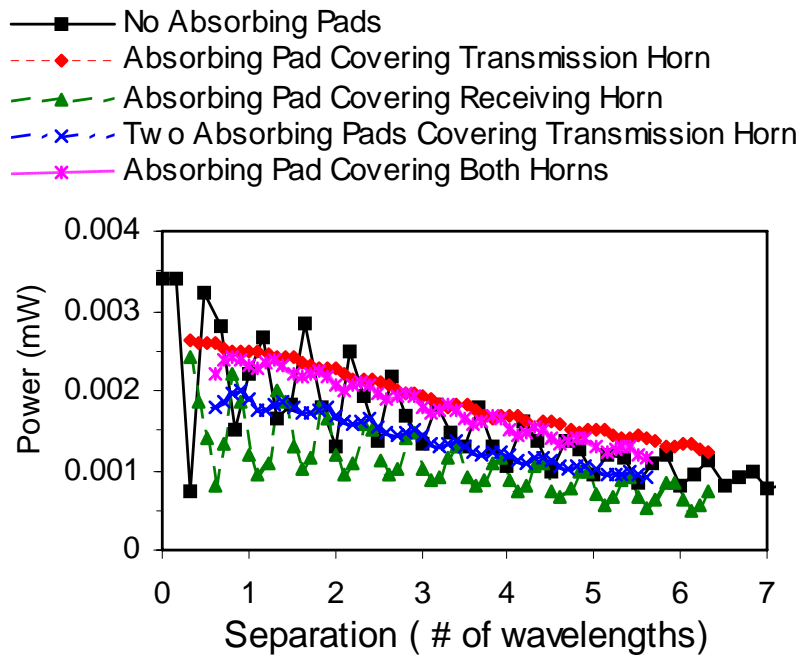


Figure 24 Interference pattern of a 10 GHz transmitted microwave beam as a function of separation distance between the X-band horns with the plasma off for several absorbing pad configurations.

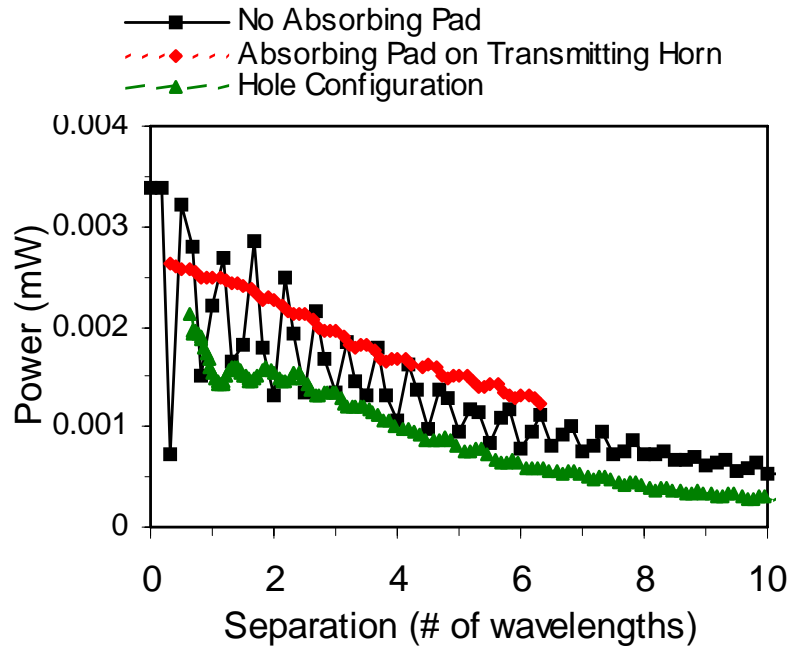


Figure 25 Interference pattern of a 10 GHz transmitted microwave beam as a function of separation distance between the X-band horns with the plasma off for the hole configuration. The no absorbing pad and the absorbing pad on the transmitting horn cases are also shown for comparison.

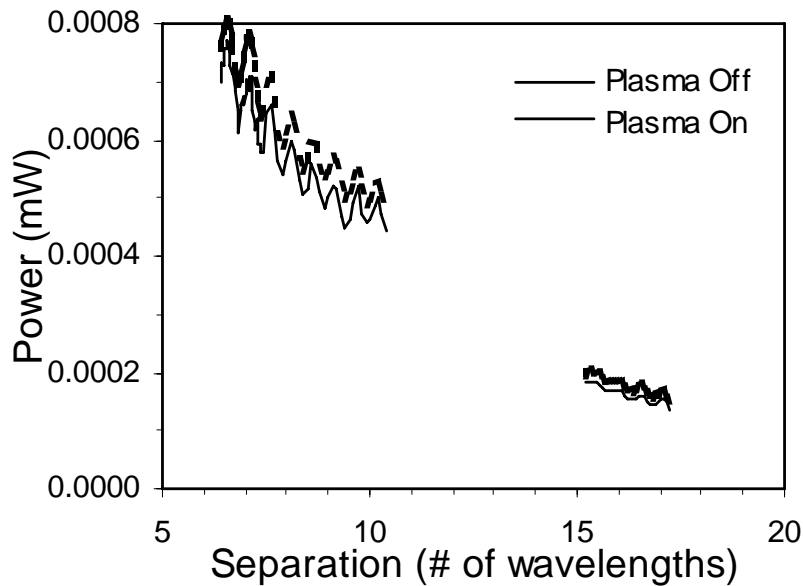


Figure 26 Transmitted 10 GHz microwave power as a function of the separation between the X-band horn for the plasma-off and the plasma-on cases utilizing an absorbing pad on the transmitting horn and an absorbing pad with a hole in it on the receiving horn. The plasma discharge is a core flow plasma.

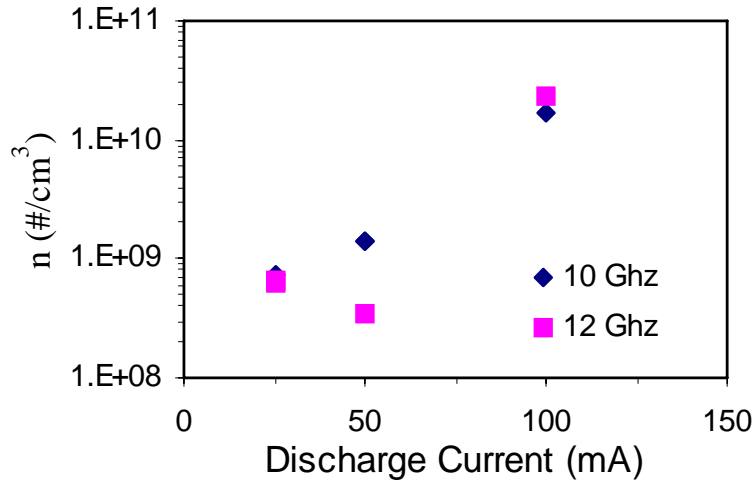


Figure 27 Electron number density versus discharge current for thin shoe electrodes with no flow through wind tunnel. Plasma produced was a glow discharge at 7 torr.

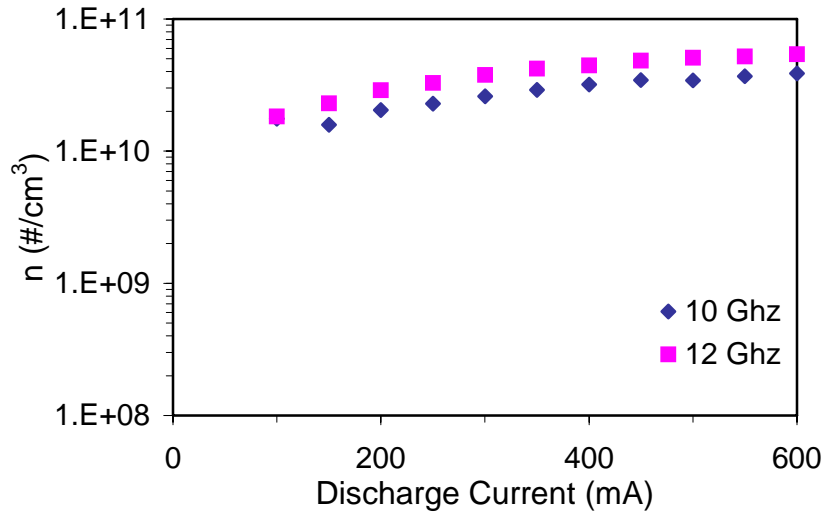


Figure 28 Electron number density versus discharge current for thin shoe electrodes with Mach 5 flow and a stagnation pressure of 300 torr. Plasma produced was a core flow plasma

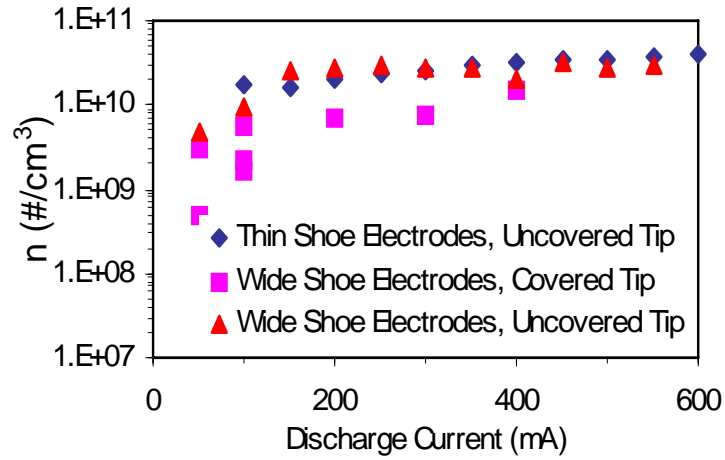


Figure 29 Electron number density vs. current for different electrodes, with Mach 5 flow and a stagnation pressure of 300 torr. The microwave frequency was 10 GHz, and the plasma produced was a core flow plasma.

4. Freestream Plasma Characterization and Optical Temperature Measurement

4.1. Introduction

It was known prior to this investigation that the discharges used for flow control would be spatially nonuniform and in nonequilibrium. The discharge structure and thermophysics need to be characterized in order to provide useful data for comparison to computations and to elucidate the actuation physics. Langmuir probe measurements and optical temperature measurements were undertaken to obtain spatial resolution of these data. This section describes in detail the optical emission spectroscopy developed to this end. The emission spectroscopy, Langmuir probe measurements, and Pitot pressure surveys were then used to characterize a plasma created in the tunnel freestream.

4.2. Temperature Measurement – Method and Verification

A system for rotational and vibrational temperature measurement using emission spectroscopy was acquired from Research Support Instruments, Inc. The system hardware consists of a fiber-optic probe connected to an Ocean Optics PC 2000 spectrometer. A collimating head may be attached to the fiber-optic probe to improve spatial resolution. Software is provided to drive the spectrometer and analyze the spectra. Vibrational temperatures are determined using the well-known Boltzman-plot method.⁷⁵ The system measures the spectrum of the second positive group of nitrogen, $N_2(C^3\Pi_u) \rightarrow N_2(B^3\Pi_g)$. The intensity of a vibrational transition is given by

$$I_{v',v''} = DN_{v'}V_{v',v''}^4 S_{v',v''}. \quad (12)$$

The assumption of a Boltzman distribution relates the upper level population and temperature:

$$N_{v'} = \frac{N}{Q_v(T)} \exp[-G(v')hc/kT]. \quad (13)$$

Substitution of Equation (13) into Equation (12) provides a straight-line relationship between the normalized intensity of the vibrational transition and the vibrational temperature:

$$\ln\left(\frac{I_{v',v''}}{V_{v',v''}^4 S_{v',v''}}\right) = -\left(\frac{hcG(v')}{k}\right)\frac{1}{T} + const. \quad (14)$$

The intensities of vibrational transitions, as normalized in Equation (14) are plotted as a function of the normalized transition energy. A straight line is curve-fitted through these points, and rotational and vibrational temperatures are extracted from the slope of the line. Transitions with intensities less than 5 percent of full-scale are rejected.

The spectrometer FWHM resolution was measured at 0.167 nm using a mercury lamp and software provided by Ocean Optics. Rotational lines are not fully resolved by the spectrometer, so rotational temperatures are estimated by comparing a simulated spectrum to the measured spectrum. Twenty rotational lines are simulated at each of 15 vibrational transitions. The predicted spectrum is convolved with the slit function of the spectrometer, and the mean square error between the predicted and measured spectrum is

computed. This curve-fitting procedure is done in 10 K increments, effectively creating a 10 K resolution in the measured temperature. Integration times for the spectral measurements described below ranged from 3 msec to 50 sec, depending on the signal strength, but the limiting factor in the data acquisition rate is the time required for curve-fitting rotational temperature measurements. Maximum data acquisition rates were several Hz.

Spectral measurements using a nitrogen discharge tube (Edmund Scientific CR30609-11) are compared in Figure 30 to measurements taken in a discharge between two rod electrodes with flow-on in the Mach 5 channel. The lower temperature of the flow-on plasma is qualitatively discernible from its spectra. Rotational bands in the flow-on case, compared to the discharge tube spectra, are pushed to longer wavelengths, indicating a relatively higher population in the lower rotational states and a de-population of the higher rotational states. Also, the spectral peaks with flow-on are pushed to longer wavelengths, probably due to the increased intensity from P-branch rotational transitions at wavelengths near the band head. Analysis of the spectra confirm these qualitative observations, indicating a rotational temperature of approximately 60 K for the flow-on case, compared to approximately 490 K for the discharge tube. Vibrational temperatures for the flow-on case are also lower, approximately 310 0K compared to 6700 K for the discharge tube.

4.3. Langmuir Probe Measurements

The Langmuir probe system used in the current measurements was developed for use in high-speed flows and has been described in detail in another reference.⁷⁶ A double probe configuration was used, consisting of two 0.2 mm diameter platinum wires 1.6 mm long with axes parallel to the flow, separated vertically by 0.5 mm. Conductivity and number density results presented here are the average of both wires. Probe data were analyzed using a model that includes the collisionless to the collisional domains but does not include the effects of high-speed fluid flow.⁷⁷ Surveys were made in the vertical direction at three axial stations near the downstream portion of the electrodes.

The electron temperature and ion number density measurements are subject to some uncertainty. A number of factors influence the accuracy of Langmuir probe measurements. Five of these factors are the fluid velocity, contamination of the probe surfaces, temporal variations in the plasma, the lack of electrons sensed by the double probe, and possibly a non-Maxwellian electron distribution.

The fluid velocity only affects flow-on results. When a Langmuir probe is placed into a hypersonic flow, shock waves develop, and these shock waves distort the plasma in the vicinity of the probe. This complicates data reduction.

The second factor affecting the results is probe surface contamination. This factor was addressed by cleaning the probe with hydrochloric acid after a number of data sets were taken. After cleaning with hydrochloric acid the probes were placed in a water-filled ultrasonic cleaner. This proved to be an effective technique for cleaning the platinum probes.

Unsteadiness in the plasma discharge may also have had some effect on the results. Although attempts were made to minimize unsteadiness, day-to-day changes and oscillations in the visual appearance of the plasma sometimes occurred. This means that

one measurement may be in a slightly different discharge than previous measurements. This could be the cause of the lack of smoothness in some of the Langmuir probe results. In addition to relatively slow changes in the discharge, small, rapid oscillations were also present. From the shape of the voltage-current characteristics measured by the Langmuir probes it is deduced that the rapid fluctuations did not have a large effect.

The last two reasons listed above, sensing a small fraction of the electrons and a non-Maxwellian electron energy distribution, can have a profound effect on the measured electron temperature. Since the electron temperature is used to calculate the ion number density these problems can also cause errors in these results. It is fortunate that the ion number densities are a much stronger function of the measured saturation currents than the electron temperature. It should be noted that if the electron temperature distribution is not Maxwellian, an electron temperature can not be defined. However, some representative temperature can be approximated for the energy distribution of electrons sensed by the probes. From the shape of the voltage-current curves measured by the Langmuir probes, it seems as if something like a Maxwellian distribution is present for the high energy electrons sensed by the double probe.

4.4. Results

4.4.1. Langmuir Probe Measurements

DC discharges were generated between two flat plates, 45.7 mm in length in the streamwise direction and 6mm wide in the spanwise direction. A photograph of the electrodes and a discharge is shown in Figure 31. The electrodes were relieved approximately 5 deg to create a low-density region on adjacent surfaces to help guide the discharge between them. Ion number densities are shown for a 50 mA discharge with flow-off and flow-on in Figure 32 and Figure 33, respectively. Measurement conditions for the no-flow case were 300 K and 7 torr. Ion number densities generally increase from anode to cathode. This is typical for a standard glow discharge.⁶² Number densities for the flow-on case are larger than the flow-off case. For the no-flow case number densities tend to decrease from the center of the electrodes back past their trailing edge. This same trend does not appear for the flow-on case. This difference may be due in some part to simplifications used in the data reduction as well as flow effects. A no-flow analysis was used to reduce the flow-on raw measurements.

Electron temperatures for the no-flow case are shown in Figure 34. Electron temperatures are generally uniform in the y -direction except close to the cathode. Temperatures lie between about 4,000 K to 9,000 K, spiking up to 25,000 K near the cathode. Electron temperatures at this y -location drop sharply downstream of the trailing edge of the plate. For the flow-on case, Figure 35, electron temperatures are generally higher than the flow off case and show a different trend as a function of y . Generally, electron temperatures are distributed around approximately 10,000 K, but reach 29,000 K just downstream of the trailing edge of the anode.

The electrical conductivity of the plasma is a strong function of the electron number density and a somewhat weaker function of the electron temperature. In addition the gas pressure also affects the results. Figures 36 and 37 show the flow-off and flow-on electrical conductivity values as a function of y and x . Conductivity for the flow-on plasma is larger than the no-flow case, but once again this may be due to the data

reduction procedure used. Conductivities tend to be higher near the cathode reflecting the higher ion number densities there.

4.4.2. Temperature and Pitot Measurements

Simultaneous with the optical temperature measurements, Pitot pressures were measured between the two electrodes with current on and current off. The Pitot probe was placed in the undisturbed freestream of the windtunnel, between shocks from the electrodes, as shown in Figure 31.

A detailed survey of the rotational and vibrational temperatures in a DC discharge was undertaken using the collimating head for the fiber-optic probe to improve spatial resolution. Spatial resolution was estimated by projecting a light backwards through the collimating head and measuring the spot diameter at the tunnel centerline. The probe volume diameter at the tunnel centerline was less than 3 mm. Surveys were made in the streamwise direction on the centerline between the two plates, and in the vertical direction near the center of the two plates for two discharge currents, 100 and 400 mA. Point measurements were also taken near the center of the discharge for a range of currents.

Rotational temperatures as a function of current are shown in Figure 38. Rotational temperatures are normalized by the freestream static translational temperature in the absence of the discharge. At a Mach number of 5.2 and stagnation temperature of 270 K, the expected static translational temperature in the absence of a discharge is 42 K. The error bars represent the +/- 10 K increment in curvefits of the rotational spectra. Measured rotational temperatures are approximately twice the static temperature.

Due to the very low density of the Mach 5 plasma channel, any assumption that rotational and translational temperatures are in equilibrium must be examined critically. The rotational relaxation number for nitrogen (the average number of collisions required for the exchange of rotational and translational energy) has been measured to be less than ten.^{78,79,80} With the collision frequency estimated to be approximately 10^7 per second, the characteristic rotational relaxation time is $O(10^{-6})$ seconds. With a flow velocity of 670 m/s, the expected distance required for relaxation is less than one millimeter. On the basis of these estimates, the discharge might be assumed to be in rotational/translational equilibrium.

An increase in translational temperature by a factor of two in the discharge would correspond to a decrease in Mach number by 1.4, if velocity remains constant. An estimate of the maximum attainable temperature rise in the discharge is obtained by assuming all power goes into heating the fluid. For a discharge voltage and current of 300 V and 400 mA, the power expended is 120 W. Constant-area and constant-pressure heating cases were examined. Constant-area heating is analyzed using the control-volume approach of Heiser and Pratt.⁸¹ Assuming constant γ and C_p , the constant-area heating exit velocity is 608 m/s, and the exit temperature is 182 K, giving a Mach number of 2.25. For constant-pressure heating, the exit Mach is 4.42 and the exit temperature is 142 K.

Mach number changes this large would be evident in Pitot probe measurements. The measured Pitot pressures in Figure 39 however, show no change when the discharge is on. This indicates no significant heating of the gas at this location. The conclusion that

no significant translational heating occurs in the bulk of the gas is bolstered by schlieren visualization of shock waves about a spherical model shown in Figure 40. In Figure 40, a portion of the schlieren image with no plasma (the darker vertical strip) is superimposed on another schlieren taken with a 150 mA discharge. No discontinuities in the shock location or slope are evident, thus indicating no significant heating. An indication of the sensitivity of this method is obtained by observing that at Mach 5.2, an 8 percent change in Mach number creates a one-degree change in Mach angle.

In summary, it must be concluded that the rotational temperature measurements do not provide an unbiased representation of the plasma translational temperature. This is presumed due to inaccuracy in curve-fitting the rotational spectra, or perhaps spatial non-uniformity across the integration path of the measurement. Rotational non-equilibrium is considered unlikely, but cannot be completely ruled out, given the uncertainty in characteristic times for rotational relaxation. The rotational temperatures may be used, however, to extract qualitative trends.

Additional spatial temperature distributions were obtained for discharges from the same electrodes, but with the support rods on the upstream ends of the plates. Rotational and vibrational temperature distributions in the streamwise direction for 100 and 400 mA discharges are shown in Figures 41 and 42, respectively. The error bars in these and subsequent figures denote $\pm 1\sigma$ deviations in the measurements as an indication of unsteadiness in the discharge. Generally the 400 mA discharge has a larger rms than the 100 mA discharge, quantitatively confirming visual observations of increased unsteadiness. Rotational temperatures for the 100 mA discharge are approximately 80K over most of the streamwise survey. Downstream of the plate, rotational temperatures begin to rise, either due to relaxation or heating from the electrode bow shock. Vibrational temperatures generally decrease in the streamwise direction, perhaps indicating a vibrational relaxation.

Rotational temperatures approximately twice freestream static translational temperatures are measured in the most upstream portion of the discharge in the 100 mA case. If energy were being dumped into the rotational mode that quickly, one would expect rotational temperatures to continue rising in the downstream direction through the discharge, but instead they remain relatively constant. The lack of a rotational temperature gradient in the x -direction for the 100 mA discharge is another indicator that little of the discharge energy goes into rotational or translational modes of the gas at these x -locations.

Vibrational temperatures for the 400 mA discharge show a more complicated variation than that observed in the 100 mA discharge. This is probably due to non-uniformity of the discharge, as evidenced by a local bright spot in the 400 mA discharge at $x/x_p = 0.7$. This bright spot has characteristics more akin to an arc than a glow discharge.

Rotational and vibrational temperature distributions in the vertical direction at $x/x_p = 0.7$ are shown in Figures 43 and 44, respectively. The upper and lower plate surfaces are at $y/y_p = 1.0$ and -1.0 , respectively. The upper limit of measurement was restricted to $y/y_p = 0.7$, due to mechanical interference in the probe drive. Rotational temperatures in the 100 mA discharge are generally about 80 K and uniform throughout the discharge in the vertical direction (Figure 43). Rotational temperatures for the 400 mA discharge are slightly higher. The rotational temperature for both discharge currents begins to increase

below $y/y_p = -0.6$, probably due to the combined effects of heating from the plate bow shock, viscous heating, and local heating in the cathode layer. Vibrational temperatures are approximately 5000 K over most of the 100 mA discharge in the vertical direction, and 7000 K for the 400 mA discharge. Like the rotational temperatures, vibrational temperatures also increase at $y/y_p < -0.6$.

Vibrational temperatures for a range of discharge currents, measured at $y/y_p = 0.0$ and $x/x_p = 0.7$, are shown in Figure 45. Unsteadiness as measured by the rms is quite high for discharges above 100 mA. Vibrational temperatures range from about 4000 K at 50 mA, and increase up to about 200 mA. Above this current, they appear to saturate at about 5000 to 7000 K.

4.5. Summary

Flat plate electrodes were used to generate DC discharges in a Mach 5 crossflow. Lower-current discharges were more steady than higher-current discharges. Langmuir probe measurements showed ion number densities and fractional ionization to be higher in the flow-on case compared to the no-flow case. Maximum ion number densities of approximately 10^{18} m^{-3} were observed near the cathode for the flow-on case. Electron temperatures ranged from 3,000 K to 25,000 K for the no-flow case, and 3,000 K to 29,000 K for the flow-on discharge. This compares to vibrational temperatures for nitrogen of 4,000 K to 7,000 K. Rotational temperature measurements in the bulk of the discharge were approximately twice the undisturbed freestream static temperatures. Pitot pressures and shock shapes in this region showed no evidence of elevated translational temperatures, however. Rotational temperature measurements showed very little gradient in rotational temperature through the discharge in the x-direction. Some local increase in rotational temperatures was recorded near the electrodes. A weak decrease in vibrational temperature in the downstream direction perhaps indicates vibrational relaxation.

It should be noted that the heating conclusions are based on measurements taken in the inviscid flow between the electrodes. As will be shown in Section 5, significant heating occurs in the boundary layer near the electrodes, particularly near the cathode. Later surveys that extended into the cathode and anode boundary layers showed pronounced Pitot pressure changes there due to the discharge.⁸² Beyond the shock emanating from the electrodes, however, no appreciable heating was detected within the visible glow.

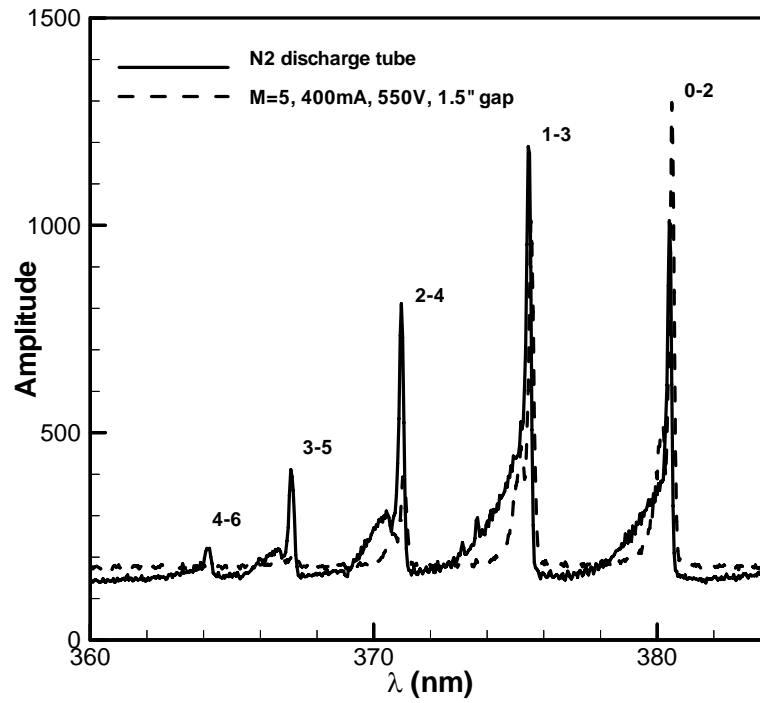


Figure 30 Nitrogen second positive group spectra for static discharge tube and Mach 5 DC glow discharge.

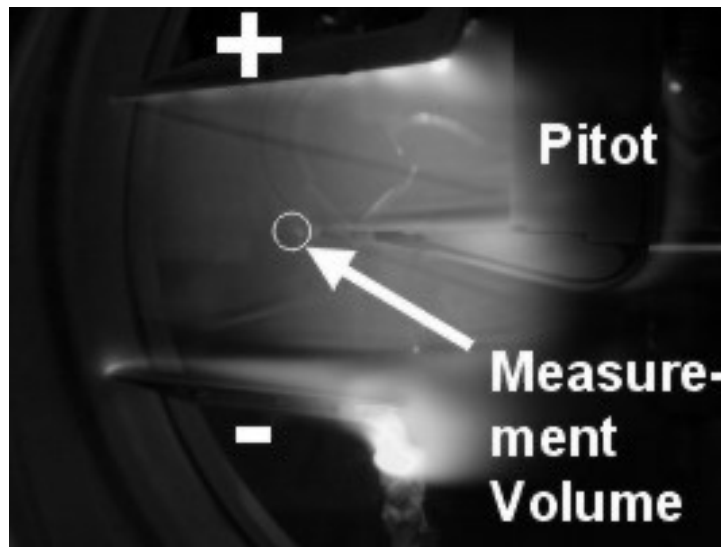


Figure 31 Photograph of discharge with Pitot probe. Note shock structure between electrodes.

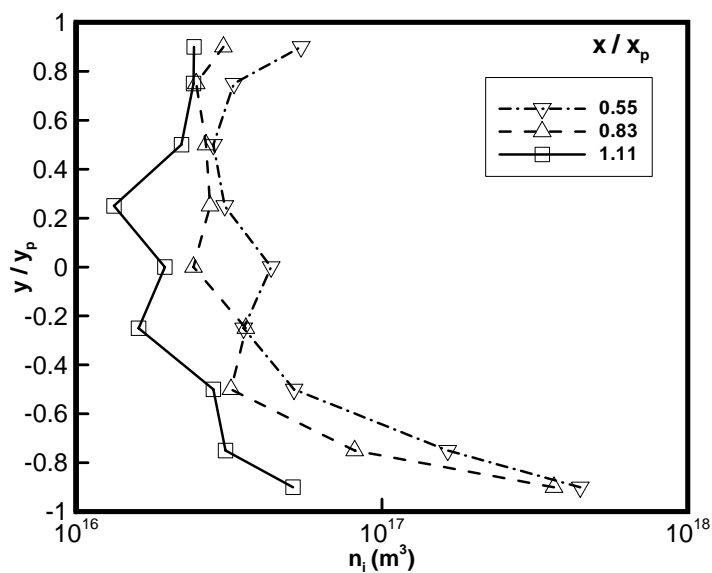


Figure 32 Ion number density in a 50 mA discharge, no-flow case. In this and next figures, spanwise location is in the center of the electrodes.

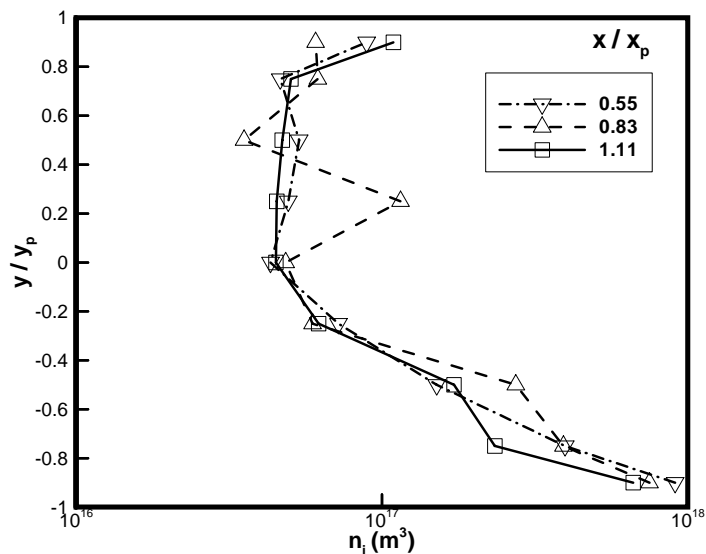


Figure 33 Ion number density in a 50 mA discharge, flow-on.

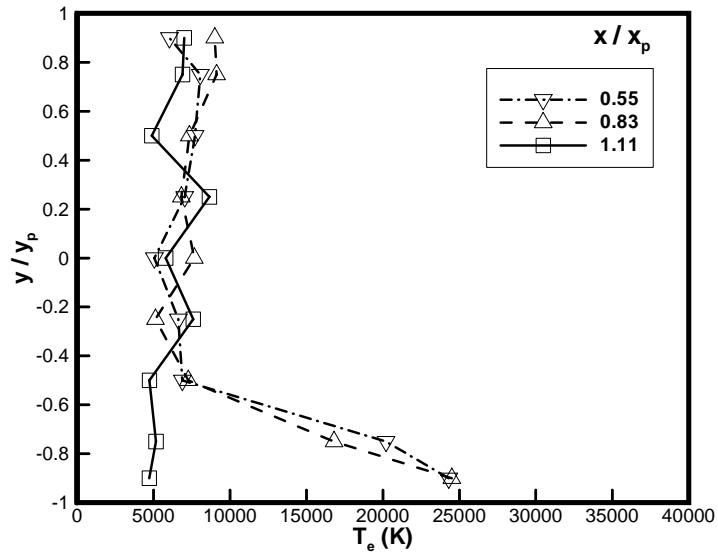


Figure 34 Electron temperature in a 50 mA discharge, no-flow case.

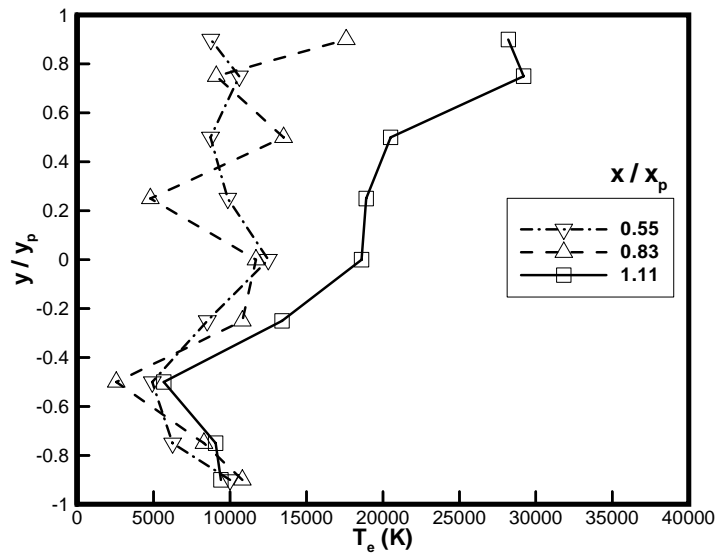


Figure 35 Electron temperatures measured in a 50 mA discharge, flow-on case.

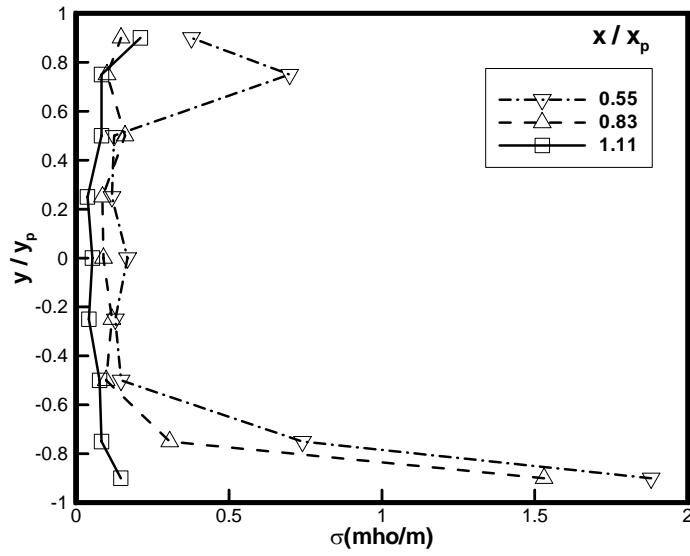


Figure 36 Plasma conductivity in a 50 mA discharge, flow-off case.

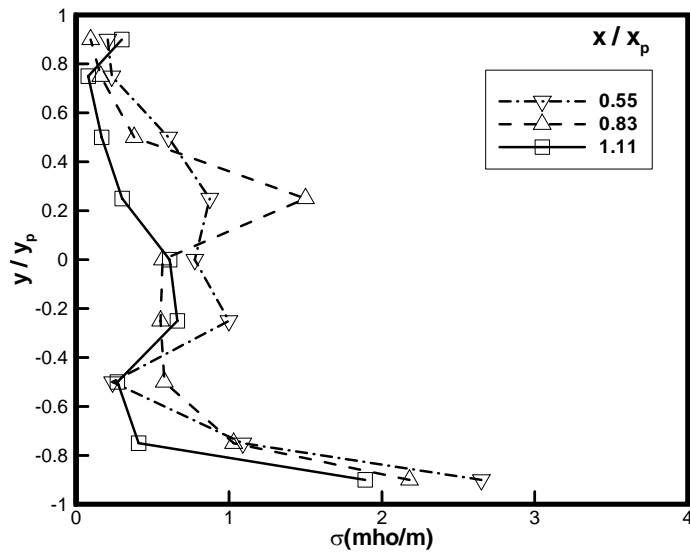


Figure 37 Plasma conductivity measured with the Langmuir probe in a 50 mA discharge.

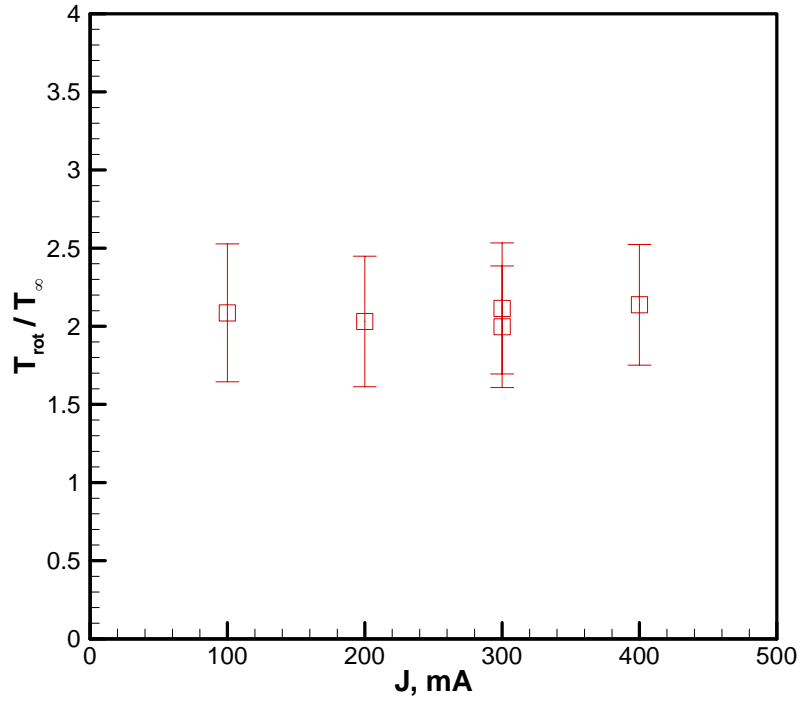


Figure 38 Rotational temperatures measured in discharge as a function of current. Error bars represent +/- 10 K uncertainty.

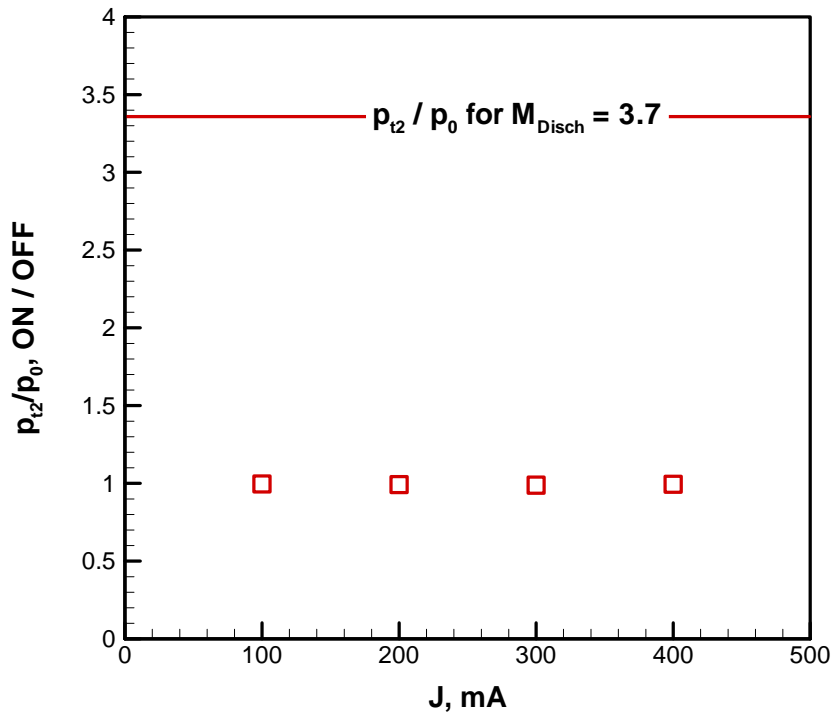


Figure 39 Ratio of current-on Pitot pressure to current-off Pitot pressure

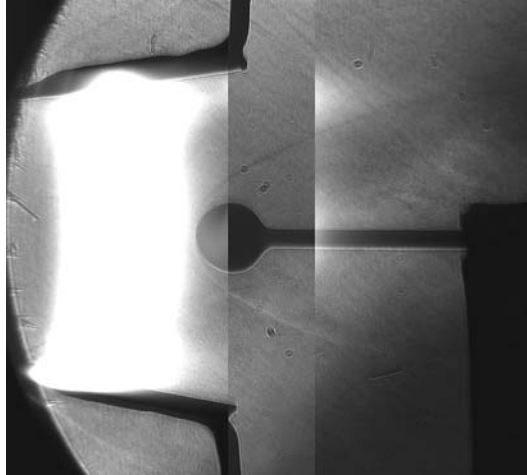


Figure 40 Schlieren image of shock produced by a sphere in the presence of a DC discharge. Luminosity from the discharge is evident between the plate electrodes on the left. The darker vertical strip in the middle is the superimposed schlieren image in the absence of a discharge.

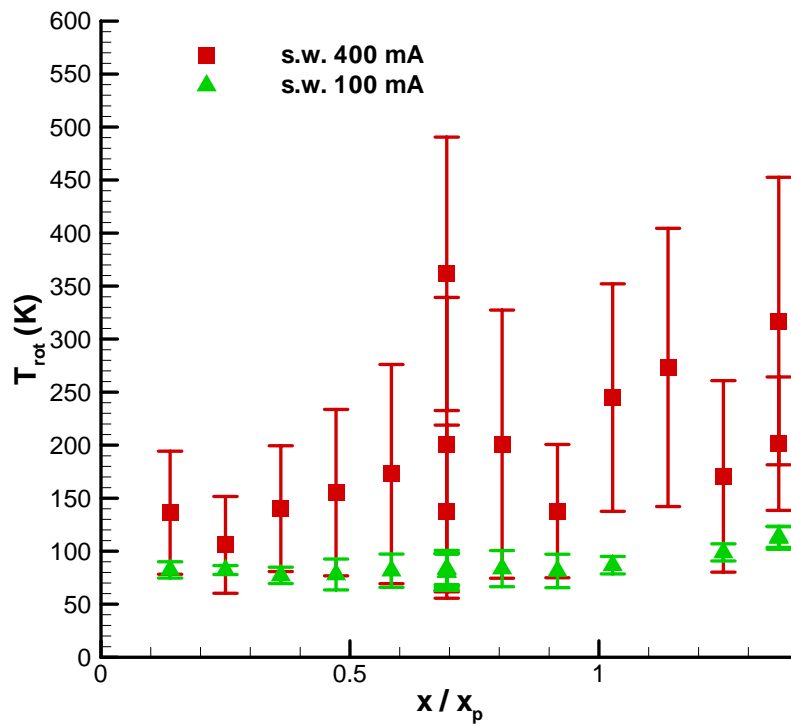


Figure 41 Rotational temperatures for 100 and 400 mA DC discharge between plates, streamwise distribution at $y/y_p = 0.0$.

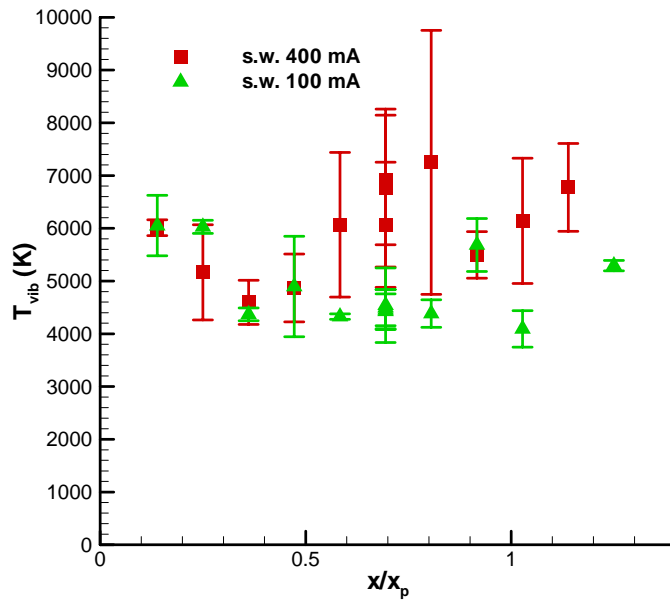


Figure 42 Vibrational temperatures for 100 and 400 mA DC discharge between plates, streamwise distribution at $y/y_p = 0.0$.

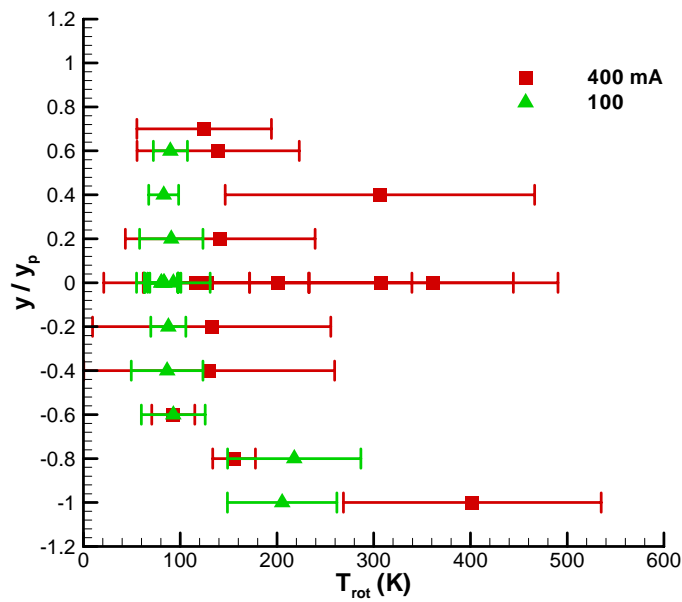


Figure 43 Rotational temperatures for 100 and 400 mA DC discharge between plates, vertical distribution at $x/x_p = 0.7$.

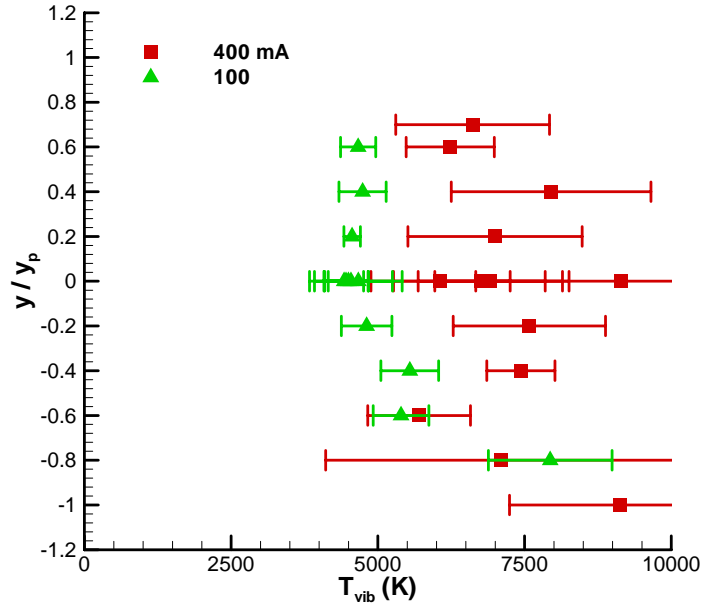


Figure 44 Vibrational temperatures for 100 and 400 mA DC discharge between plates, vertical distribution at $x/x_p = 0.7$.

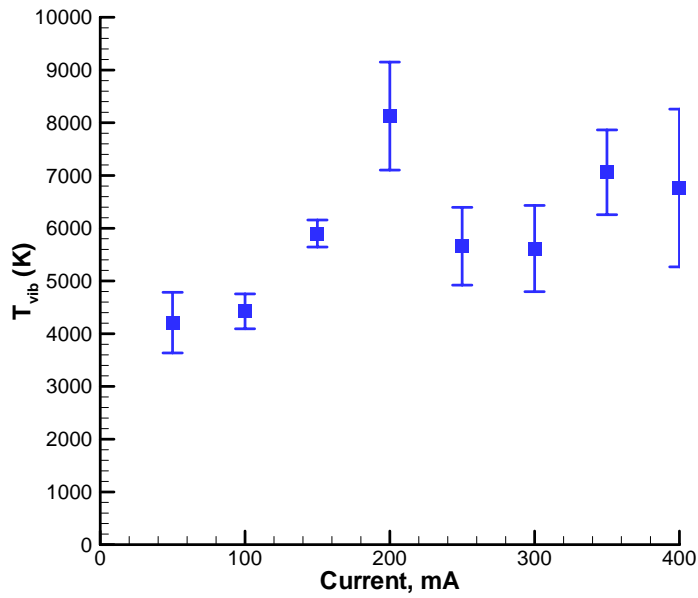


Figure 45 Vibrational temperatures for DC discharges between plates, at $x/x_p = 0.7$, $y/y_p = 0.0$ as a function of discharge current.

5. Thermal Actuation Using Surface Discharges

5.1. Introduction

Menart et al.²⁹ observed that surface DC discharges caused a local increase in static pressures on a flat plate at Mach 5. In this experiment, streamwise and transverse discharges were generated on a flat plate. The maximum effect was derived from the streamwise discharge, with cathode upstream, and observed just downstream of the cathode. These results occurred even without the presence of a magnetic field, and were ascribed to Joule heating of the fluid from the discharge. Magnetic fields imposed normal to the plate surface modified the pressures. This effect was believed to be caused by an interaction between the magnetic field and the plasma discharge, creating a change in the discharge heating. There was no evidence indicating effects of a Lorentz force on the bulk fluid flow, however, even though a magnetic field would distort the visible glow from the discharge.

The motivation for the work described in this section was to investigate the effects of plasma discharges on hypersonic boundary layers, with and without magnetic fields, and elucidate in more detail the effects observed in Ref. 29. Flowfield surveys were obtained to aid in CFD validation.

5.2. Experiment

The flat plate was constructed of machinable ceramic with copper electrodes. A schematic is shown in Figure 46. The discharge was run with the cathode either upstream or downstream. In all cases the discharge was run in a constant-current mode. The model contained three pressure taps on centerline, spaced 1.27 cm apart, as shown in Figure 46.

It is recognized by the authors that the DC discharge may not be an optimum system for demonstrating MHD effects. Higher conductivities and more diffuse plasma may be achieved with an RF discharge. The objective of the current work was merely to demonstrate the feasibility of surface discharges for boundary layer control and to investigate their behavior with and without applied magnetic fields.

At a stagnation pressure of 370 torr the length Reynolds number for the plate based on freestream conditions was 9.4×10^4 . The boundary layer would be expected to be laminar at this Reynolds number. This was verified by placing a Pitot probe near the plate surface and varying tunnel stagnation pressure. The near-surface Pitot pressure (Figure 47) showed a smooth trend with stagnation pressure, indicating that boundary layer transition did not occur over this pressure range. A survey of the boundary layer at $x = 5.65$ cm (Figure 48) showed a laminar-like profile. The measured boundary layer thickness was approximately twice that of a similarity solution for a sharp leading-edge flat plate. The discrepancy between the measured boundary layer and a similarity profile is not unexpected, given the viscous interaction and bluntness present in the experiment.

5.3. Results

5.3.1. No Applied Magnetic Field

The effect of the DC discharge on surface pressures is shown in Figure 49. After an initial 20-second period, the discharge was turned on for 40 seconds, then turned off. For all 50 mA discharges with $B=0$, voltage varied from 1100 to 1200 V.

Voltages were generally steady for the first 20 seconds of a run, as shown in Figure 50, with the exception of some ramp-up time after the current was initially turned on. All measurements, including voltages, were sampled at 0.5-second intervals. After about 20 seconds of current-on time, some unsteadiness in the discharge was observed. The largest increase in pressure, up to 10 percent of the undisturbed static pressure, occurs just downstream of the cathode.

Electron number density obtained from Langmuir probe measurements is shown in Figure 51. Electron number density as a function of x is shown at four heights above the plate surface. Surveys were on the plate centerline. Electron number density is highest near the plate surface, and decreases away from the plate. Peak number densities of about 10^{12} cm^{-3} are obtained above the cathode. Low electron concentrations are measurable 0.5 cm above the plate surface downstream of the cathode, but the number density at this height drops off rapidly upstream and downstream from this location.

The mechanism for the increase in surface pressure is postulated to be the increase in boundary layer displacement thickness due to heating from the discharge. The 10 percent pressure increase shown in Figure 52 is equivalent to approximately a 0.8-degree flow deflection through an oblique shock at Mach 5. The local flow deflection, θ , due to the growth of the boundary layer is equal to $d\delta^*/dx$. The pressure increase due to this deflection is related to the Mach number through the $\bar{\chi}$ parameter⁸³ where

$$\bar{\chi} = \frac{M_\infty^3}{\sqrt{\text{Re}}} \sqrt{C}, \quad (15)$$

and C is the Chapman-Rubesin parameter, $\rho_w \mu_w / \rho_e \mu_e$. For an adiabatic flat plate, laminar boundary layer in the weak interaction regime,

$$\frac{P}{P_\infty} = 1 + 0.31\bar{\chi} + 0.05\bar{\chi}^2. \quad (16)$$

It is obvious from Eqns. (15) and (16) that the induced surface pressure from slope-changes in boundary layer displacement thickness is a strong function of Mach number. This and the results shown in Figure 49 indicate a potential for creating forces and moments on hypersonic vehicles through surface plasma discharges. This observation has also been made by Leonov et al.,⁵⁵ although these discharges were at a higher-power and lower Mach number and in some cases separated the boundary layer.

It should be noted that energy input to the laminar boundary layer will certainly influence its stability. Adverse pressure gradients will trip or otherwise destabilize the boundary layer. Changes in the boundary layer profile, the enthalpy of the boundary layer fluid, and heat transfer to the wall have all been demonstrated to affect stability and transition.⁸⁴

These effects are interrelated and quite complex, and it is impossible to predict a priori their net effect on boundary layer stability.

To estimate the temperature increase from the discharge, a total-temperature probe was introduced into the flow. The thermocouple consisted of a junction inside a floating sheath and electrically isolated from the sheath. Thermocouple measurements in discharges are subject to numerous uncertainties. These include induced currents in the thermocouple and exothermic vibrational relaxation and recombination on the probe. Relaxation and recombination in this flow could not be assessed, but temperatures showed no discontinuities when the discharge was extinguished, thus indicating that there was no electrical interference. Also, no distortion of the discharge glow in the presence of the thermocouple was observed. The measurements in this experiment possibly suffered from conduction along the sheath of the probe. Also, the probe was not calibrated for recovery factor. The total-temperature probe measurements are thus largely qualitative. However, the results in Figure 52 clearly show increases in measured total temperature within the discharge. Measured total temperatures peak near the cathode and relax downstream and away from the plate surface. Since the probe is uncalibrated, measured total temperatures in the undisturbed flow are less than the stagnation temperature.

A Pitot pressure survey through the boundary layer and bow shock is shown in Figure 53. It is clear from these data that the boundary layer is decelerated and slightly thickened due to the discharge. Above the boundary layer edge, Pitot pressure is slightly increased in the presence of the discharge due to the more efficient compression through the oblique wave system. These effects on Pitot pressure and the above-observed effect on surface pressure are similar to those observed by Leonov et al.⁵⁵ using surface DC discharges and predicted by Shibkov et al.⁵⁰ for surface microwave discharges.

The coalescence of the compression wave system from the cathode is demonstrated by streamwise Pitot surveys shown in Figure 54. The compression wave is manifested as an increase in Pitot pressure when the discharge is on. As the height above the plate increases, the compression front moves downstream. Downstream, the Pitot tube is engulfed in the growing boundary layer, and Pitot pressure decreases when the discharge is turned on, due to thickening of the boundary layer.

Figure 55 shows the effect of discharge power on surface pressures. These pressures are an average of the last ten seconds of data with the discharge on. Although the effects are rather complex, several trends are noted. In general, the surface pressure increase is roughly linear with power. This is especially evident for the two downstream pressure taps. The pressure tap nearest the cathode shows a more complex behavior. At this location, the pressure increases linearly with power, with the exception of outlier points near 60 and 140 W. The cluster of points near 60 W corresponds to 50 mA discharges. It was observed that at this current level the discharge was generally diffuse. This is also the case for the outlier point at 140 W (point A in Figure 55). At other currents, the discharge had a tendency to constrict. This behavior is illustrated with images of the 140 W discharge in and the 170 W discharge (point B in Figure 55) in Figure 56 and Figure 57. The 140 W discharge is fairly diffuse and uniform, but the 170 W discharge shows a non-uniform, constricted structure on the right of the plate.

Presumably, the brighter portion of the 170 W discharge in Figure 57 corresponds to a higher conductivity region with a higher current density. Locally higher heating is expected here, but the pressure increment from this heating has not propagated laterally to the most upstream pressure tap. At the more downstream stations however, the pressure rise from the local hot region has been communicated to the pressure taps. This explains the more regular trend of pressure versus power at these stations.

5.3.2. Thermal Response of the Plate and Electrode

The observed effects in short-duration discharges were expected to arise primarily from Joule heating of the plasma. During longer discharges the electrodes heat, and the boundary layer fluid may be heated by convective heat transfer from the electrodes and the region of the ceramic plate near the electrodes. The lagged response of the surface pressures shown in Figure 49 and the temperature response of the cathode and plate raise the question of how much of the pressure response is due to Joule heating of the fluid in the discharge, and how much is due to convection from the hot cathode and plate to the fluid.

An attempt was made to answer this question by examining the time response of the interaction. In order to do this, the time-response of the instrumentation had to be assessed. This was done by manually increasing the stagnation pressure by about 7 percent over one second. The Pitot pressure response was well-described by a first-order system with a time constant of approximately 0.4 seconds. The surface pressure response however was highly lagged and had not fully equilibrated even after 80 seconds.

The effect of heat transfer from the plate to the boundary layer is illustrated in Figure 58. In this case, the discharge was turned on for periods of 40, 20, 10, and five seconds. It is seen that for the 40-second discharge, the Pitot pressure drops about 6 percent immediately after the discharge is turned off. After this, approximately 50 seconds is required for it to decay to its undisturbed value. This slow decay indicates that heating of the electrode has occurred during the discharge. As the plasma-on time decreases, the recovery time decreases. For the five-second discharge, most of the Pitot-pressure decay occurs immediately after the plasma is turned off. In this case, the electrode and plate have had little time to heat during the discharge. It is likely in this case that the bulk of the observed effect is due to Joule heating of the plasma. The Pitot pressure recovers quickly after the discharge is extinguished because the Joule heating ceases.

Figure 59 illustrates the Pitot probe response for discharges of approximately three and five-seconds duration. The Pitot probe location was 0.5 cm above the plate surface at the rear edge of the downstream electrode, on the model centerline. In this case, the cathode was upstream. When the discharge is turned on, the Pitot pressure drops due to the thickening of the boundary layer. When the discharge is extinguished after five seconds, two timescales are evident. The Pitot pressure recovers to about 60 percent of its pre-discharge value within about one second. This rapid change in pressure is due to the removal of Joule heating in the plasma. After this initial rapid response, the pressure recovers more slowly, as thermal energy accumulated in the electrode and ceramic plate convects into the boundary layer. For a discharge of approximately three seconds duration, the electrode and plate have had less time to heat, so 90 percent of the pre-discharge Pitot pressure is recovered within about one second. For discharges of three

seconds or less for this configuration, the bulk of the surface pressure effects are thus due to Joule heating of the plasma.

Temperature-sensitive paint and a thermocouple were also used to estimate the time-dependent temperature of the cathode and plate. A thermocouple embedded in the cathode measured cathode temperature. A switch was used to disconnect the thermocouple from the data acquisition hardware prior to turning on the discharge. When the discharge was extinguished, the switch was closed to reconnect the thermocouple. A sample thermocouple signal versus time is shown in Figure 60. This process was repeated for a variety of discharge-on times to form an approximation to the temperature versus time response of the cathode. The cathode temperature as a function of time is shown in Figure 60. The cathode heats quickly, increasing 100 K within the first five seconds. Temperature-sensitive paint was used to visualize propagation of the temperature pulse through the ceramic plate. Prior to the discharge, the plate was at a nearly uniform temperature. After a 40 second discharge the plate surface temperature immediately upstream of the cathode increased as much as 50 K. Near the anode, the plate surface temperature increase was less than 10 K.

5.3.3. Effect of Magnetic Field on Applied Voltage

In this portion of the investigation, current, voltage and surface pressures were recorded at a 2 Hz sampling rate. Data were acquired continuously during each 20-second discharge and for 20 seconds before and after. For cases with an applied magnetic field, the magnet was turned on and stabilized at a predetermined field strength before data were taken. Data were obtained at increasing field strengths until a stable discharge was no longer obtainable.

Voltage as a function of applied magnetic field for currents of 0.05, 0.1, 0.2, and 0.3 A are shown in Figure 61. Negative currents refer to cases in which the upstream electrode is the cathode. The plotted voltages represent an average over the last fifteen seconds of the discharge. For currents with magnitudes of 0.1 to 0.3 A, the voltage required to drive the current generally increases with increasing magnetic field. Within the scatter of the data, there is no dependence on the placement of the cathode. For 0.05 A current, the behavior is more complex. These data exhibit a great deal of scatter and show a trend of decreasing voltage with increasing magnetic field for $-0.4 < B < 0.2$ T. This is a region of high scatter in the data. Also, at $B=0$, the voltage required to drive the current downstream is about 1400 V, compared to about 1200 V for current upstream. At higher magnetic fields, voltage increases with increasing magnetic field as it does at the other current levels.

The source of this behavior is a switch in the structure of the discharge from a generally diffuse to a more constricted discharge at higher currents and magnetic fields. In some cases (for example, $B=0.1$ T and 0.05 A) the images and voltage records indicate an unsteady switching between the two modes, so that the net result is an average of the two modes.

An estimate of the bulk fluid conductivity at zero magnetic field may be obtained by estimating the electric field and the current density. The electric field is assumed proportional to the applied voltage over the electrode separation, $V/\Delta x$, and the current density is assumed proportional to the total current divided by the electrode area, J/A . A 0.05 A current at 1100 V implies a bulk conductivity of about 7×10^{-3} mho/m. This is

contrasted with a 500 V applied voltage for a 0.2 A current, implying an effective conductivity of 0.06 mho/m. It must be stressed that these values are effective or bulk conductivities, for comparison purposes only. The electric field is non-uniform, especially near the cathode. Conductivity is also nonuniform. Langmuir probe measurements (Figure 51) show that the electron number density at a given height above the plate can vary an order of magnitude between cathode and anode. A similar variation is observed in the vertical direction between the cathode and the edge of the discharge.

The increased voltage required to drive a constant current in a magnetic field is consistent with a Hall effect. Given the relatively low density of the flow, a pronounced Hall effect is not unexpected. The current transverse to the magnetic field lines is

$j_x = \sigma(E_x - \beta E_y)/(1 + \beta^2)$.⁴⁰ Assuming that the fluid conductivity is independent of the applied electric field, data at 0.9 T for a 0.2 A current compared to the zero magnetic field case indicate an effective Hall parameter of approximately 1.3. This value may be compared to an expected Hall parameter based on collision frequency data from Raizer.⁶² Raizer cites a collision frequency of 3.9×10^9 per second per standard torr. With the freestream temperature a factor of six lower than ambient, this implies a collision frequency of 2.3×10^{10} per second at freestream densities. With⁴⁰ $\beta = eB/(m_e v)$, this implies a Hall parameter at $B=0.9$ T of about 7, significantly higher than the value inferred from experimental measurements. Again, it must be stressed that the experimental value is a bulk parameter, and that the structure of the discharge varies significantly with the magnetic field. Also, it is questionable whether the conductivity remains constant with changes in applied electric field. Nevertheless, it is clear that the electron mobility is restricted across the magnetic field lines.

5.3.4. Effect of Magnetic Field on Surface Pressures

Surface pressures were recorded for a variety of magnetic field strengths and currents, and for all combinations of electrode and magnet polarity. For these cases the current vector is largely in the plane of the flat plate and directed either upstream or downstream. The magnetic field vector is also in the plane of the plate and transverse to the freestream velocity. The Lorentz force vector in this case is oriented either into or out of the plate surface, depending on the relative electric and magnetic field polarities. If the pressure induced by the discharge is due to a modification of the boundary layer displacement thickness, then a Lorentz force oriented into the plate should suppress the pressure rise associated with Joule heating, and a Lorentz force directed away from the plate should enhance the pressure rise, given sufficient coupling between the plasma and neutrals.

Two factors combine to complicate interpretation of the magnet-on pressure measurements. First, in order to obtain high interaction parameters, high load factors, E/UB , were tested. The maximum load factor attained was over 500. At such high load factors, Joule heating is inescapable and can dominate the interaction. The dominance of Joule heating and convection in and out of the plate surface make it difficult to separate heating from MHD effects. Second, as noted in the above section, the structure of the discharge changes with the application of a magnetic field, generally from a diffuse discharge at $B=0$, to a more constricted discharge at higher values of B . Also, as noted below, the tendency of the discharge to follow magnetic field lines causes some of the visible discharge to appear around the sides of the model, rather than entirely on the top of the plate. The structure of the discharge strongly affects pressures at the most

upstream tap (Figure 55). At more downstream locations, the pressure is less sensitive to the structure of the discharge, since the pressure signal from the discharge is able to propagate laterally to these taps.

Images of the discharges for $B=0$ and $B=0.9$ T in the positive and negative directions for 50 mA discharges are shown in Figure 62. It is apparent that the magnetic field does indeed influence the shape of the discharge in the expected manner. A Lorentz force vector oriented into the plate suppresses the thickness of the glow above the plate. In fact, the discharge tends to spill over the plate surface and around the sides of the plate. Conversely, a Lorentz force vector oriented upward tends to move the glow off the plate surface. For this case (Figure 62, bottom), a dark region can be observed between the bright portion of the glow and the plate surface.

The interaction parameter in the presence of an applied electric field is given as $I = (\sigma B^2 L / \rho U)(E / UB)$. The fluid conductivity and electric field are unknown and spatially non-uniform. An estimate of the bulk conductivity may be obtained from the current density, $j = \sigma E$. The current density j is likewise non-uniform, but is estimated based on the overall current and electrode area, $j = I/A$. The gas density, ρ , and velocity, U , are assessed at edge conditions. For this experiment, using the above assumptions, the interaction parameter is approximately $JB/26$. The maximum interaction parameter attained in this experiment, based on the above assumptions, was 0.009.

The ratio of the Lorentz force to viscous forces on a fluid element is equal to the square of the Hartmann number times the load factor. For the conditions of this experiment, $Ha^2 E/UB \approx 40JB$. The maximum Hartmann number obtained in this experiment is approximately nine, indicating that the maximum Lorentz force achieved is significant compared to viscous forces in the boundary layer.

Surface pressures for each of the three pressure taps on the plate surface are plotted against applied power (Figure 63). Overall, induced pressure increases with increasing power input, but the scatter in the data is quite high. Except for tap 3 at powers below 90 W, the cathode-downstream discharges create a lesser pressure rise. This behavior of the tap 3 pressure is probably correlated with a change from a diffuse to a constricted discharge in this range.

Figure 64 shows the induced pressure for each tap as a function of total current times magnetic field, which as shown above, may be related to some measure of bulk interaction parameter. The sign of JB is retained to differentiate between the Lorentz force into the plate ($JB < 0$) and Lorentz force out of the plate ($JB > 0$) cases. Cases with $B=0$ are not plotted, since they were obtained at various powers and do not scale in this coordinate system. Scatter is present, but is considerably reduced compared to scaling with power. The Lorentz force direction has little effect on the most upstream tap pressure. Tap two shows some effect of the Lorentz force vector direction. A Lorentz force into the plate reduces the pressure rise, compared to a Lorentz force out of the plate. This trend is further emphasized for tap 3. In some cases the pressure rise at tap 3 is completely negated by the magnetic field.

This result is consistent with the expected behavior of a Lorentz force coupled into the neutrals. However, given the significant changes in discharge structure with magnetic

field, and the strong effect of Joule heating, it cannot be ruled out that the observed magnetic field effects are due in part or whole to changes in Joule heating from the magnetic field. Figure 62 shows that at least part of the discharge moves around the sides of the plate for a sufficiently high field. Nevertheless, the effects observed in Figure 64 show a pronounced and repeatable coupling between the applied magnetic field and the surface pressure.

5.4. Summary

The streamwise DC discharge on a flat plate at freestream Mach 5 has a pronounced effect on surface pressure. Heating thickens the boundary layer, increasing the slope of the displacement thickness and increasing surface pressure. The bulk of the heating occurs near the cathode. A compression wave system emanates from the cathode and interacts with the bow shock. A 50 mA (approximately 60 W) discharge increases surface pressures immediately downstream of the cathode approximately 10 percent. Smaller pressure increases occur downstream.

The pressure increment due to the discharge scales roughly linearly with the discharge power for the range of parameters considered. In general, the pressure increment near the cathode was higher for more diffuse discharges. A constriction in the discharge had a pronounced effect on the pressure near the cathode, but had a lesser effect downstream. This is presumed to be due to the non-uniformity of the discharge near the cathode.

Magnetic fields changed the structure of the discharge and altered the pressure distribution. At low magnetic field strengths some constriction of the discharge occurred, lowering the power input to the plasma and decreasing the pressure rise. At higher magnetic fields power inputs increased, perhaps due to the Hall effect, with attendant increases in pressure. The Lorentz force visibly acted on the plasma glow, but the interaction parameter was apparently not large enough to dominate over heating effects. In general, the pressure distribution over the plate was more uniform in the presence of a (-B) field (Lorentz force away from the plate surface). Integration of surface pressures shows the overall induced normal force to be larger for $B=-0.9$ T than for $B=0$ T.

Surface discharges are shown to be an effective means of manipulating the pressure field about a flat plate. The configuration demonstrated in this paper could have applications as a virtual flap or boundary layer diverter. The observed effect is due to Joule heating of the boundary layer fluid near the cathode. The heated fluid expands and deflects the external flow. Although there is some convective heat transfer from the electrode to the gas, for discharges of less than several seconds the bulk of the observed effect is due to Joule heating of the fluid.

For the configuration tested, the discharge tends toward a diffuse discharge for currents of less than 100 mA and magnetic fields less than about 0.2 T. Higher currents and magnetic fields create a more constricted discharge. When the discharge is constricted, increasing voltage is required to drive a fixed current in the presence of an applied magnetic field. Although this observation is consistent with a Hall effect, the measured effective Hall parameter is less than that predicted using published values for collision frequency. This discrepancy is probably due to changes in the structure and conductivity of the discharge which are not accounted for in calculation of an effective Hall parameter.

Observation of the glow from the discharge indicated that a Lorentz force oriented into the plate pushed the discharge downward, and a Lorentz force vector oriented upwards pushed the discharge away from the plate. Surface pressures on the plate were affected accordingly. The pressure rise was enhanced in the presence of an upward-oriented Lorentz force, and negated when the Lorentz force vector was oriented downward. This effect is more pronounced with increasing x . This effect is consistent with a Lorentz force coupling into the neutrals and changing the boundary layer thickness. However, given the 3D nature of the discharge, the alteration of the discharge with magnetic field, and the strong Joule heating of the boundary, it cannot be ruled out that this effect is due to a change in Joule heating with the applied magnetic field. Nevertheless, the observations show a consistent effect of the magnetic field on the pressure field created by the discharge.

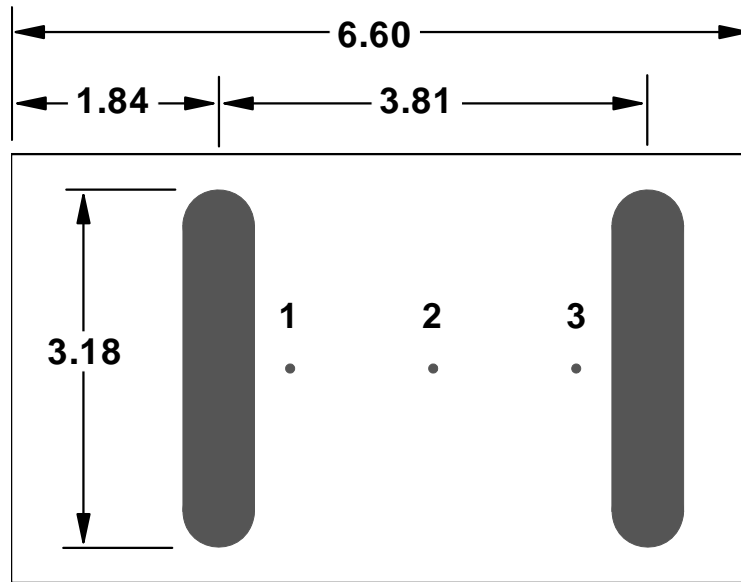


Figure 46 Schematic of flat plate model. All dimensions cm. Electrodes are 0.64 cm wide. Pressure taps are spaced 1.27 cm, starting at $x = 2.48$ cm.

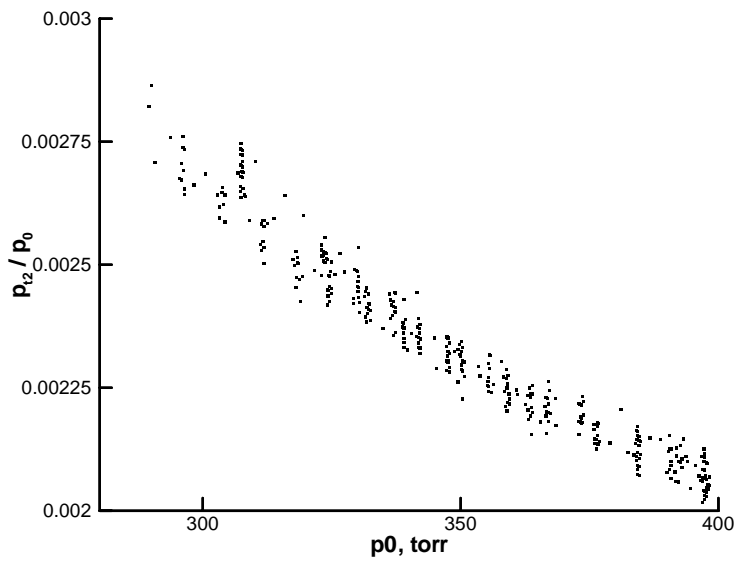


Figure 47 Pitot pressure near plate surface, normalized by stagnation pressure, as a function of stagnation pressure.

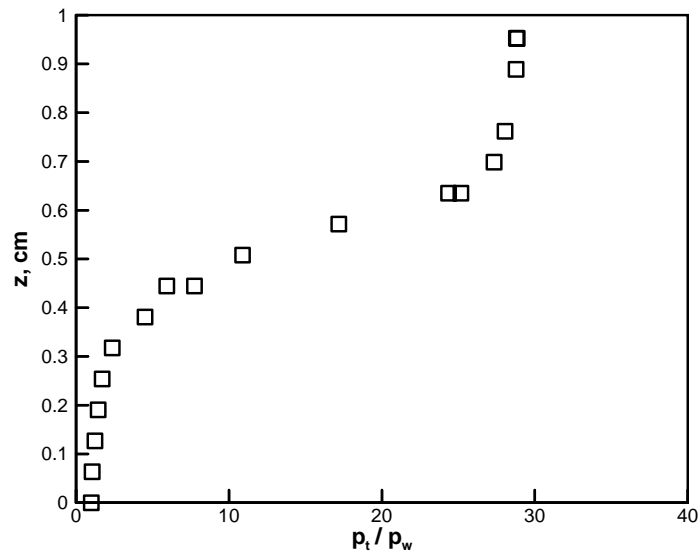


Figure 48 Pitot survey at $x = 5.65$ cm from leading edge.

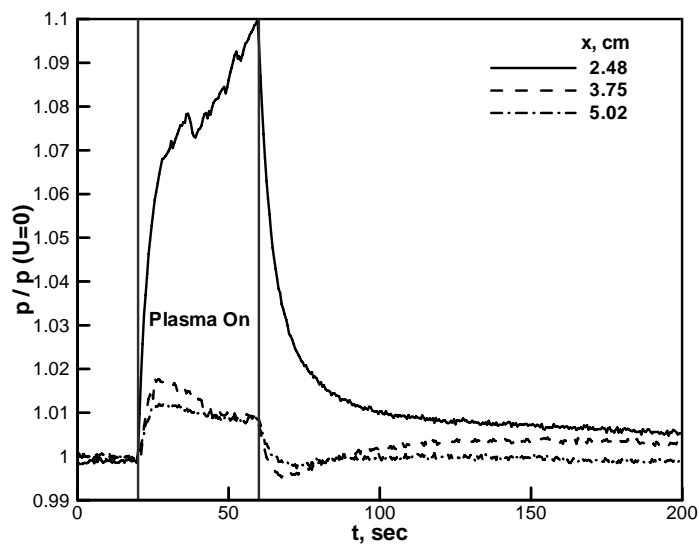


Figure 49 Effect of DC discharge on flat plate surface pressures. Pressures are normalized by undisturbed ($U=0$) static pressures.

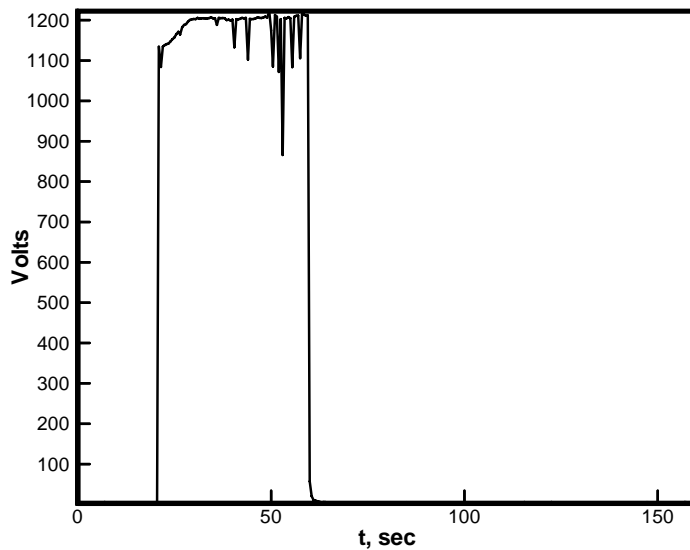


Figure 50 Sample voltage trace during discharge.

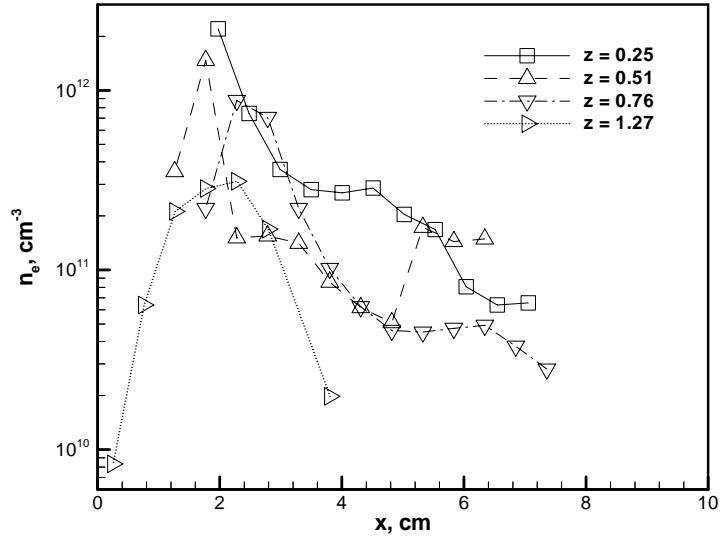


Figure 51 Electron number density as a function of streamwise distance at four locations above plate surface. Measurements made on model centerline.

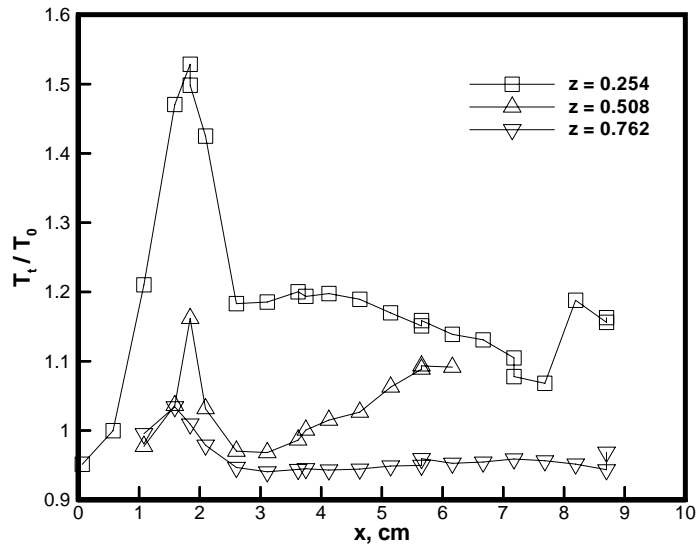


Figure 52 Average discharge-on total temperature measurements at three locations above plate surface, normalized by stagnation temperature.

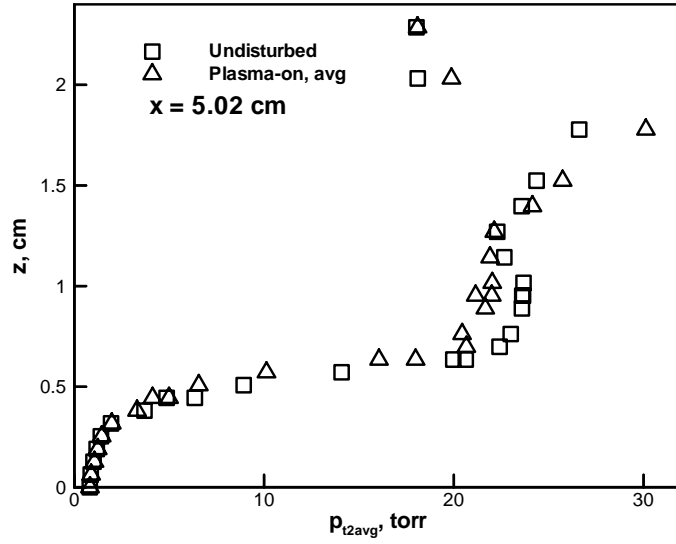


Figure 53 Average Pitot pressure above downstream electrode (anode) on flat plate.

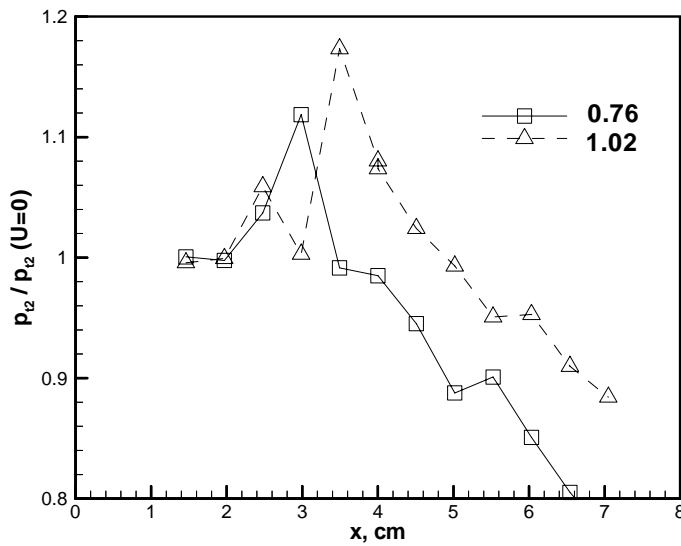


Figure 54 Average Pitot pressure during discharge normalized by undisturbed Pitot pressure as a function of distance along the model for two heights above the plate.

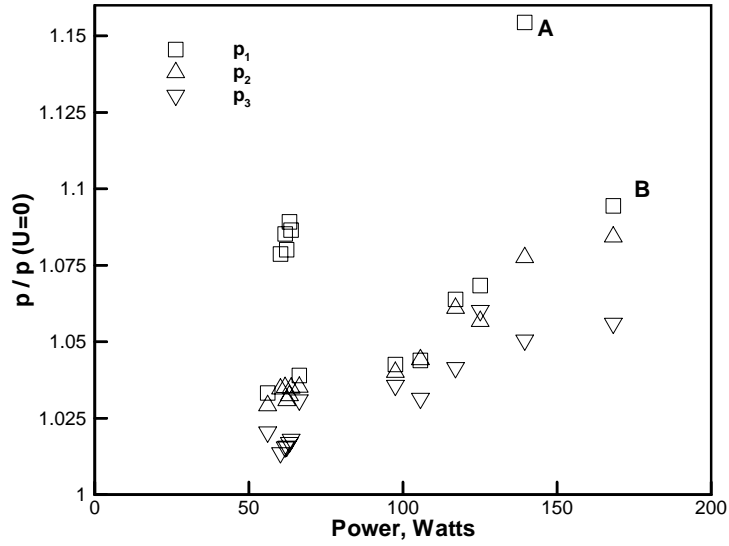


Figure 55 Normalized surface pressure at stations 1, 2, 3 ($x= 2.48, 3.75$ and 5.02 cm, respectively) as a function of discharge input power. Pressure is normalized by discharge-off pressure.



Figure 56 100 mA, 140 W discharge, point A in Figure 55. View is from location downstream and above plate. Flow is from top-to-bottom, cathode is at top of image.

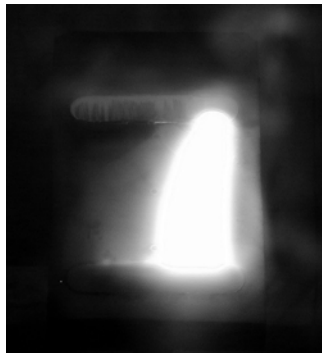


Figure 57 400 mA, 170 W discharge, point B in Figure 55.

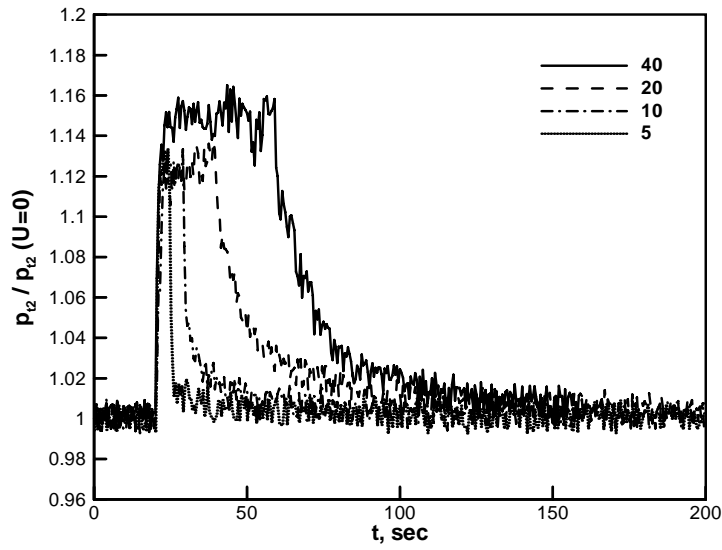


Figure 58 Ratio of average Pitot pressure during discharge to undisturbed Pitot pressure for four different discharge durations.

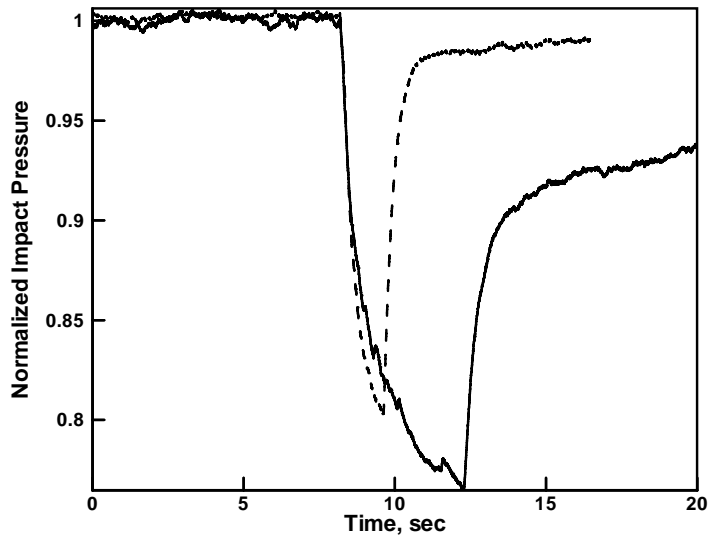


Figure 59 Pitot pressure measured 0.5 cm above the plate surface at the downstream edge of the rear electrode.

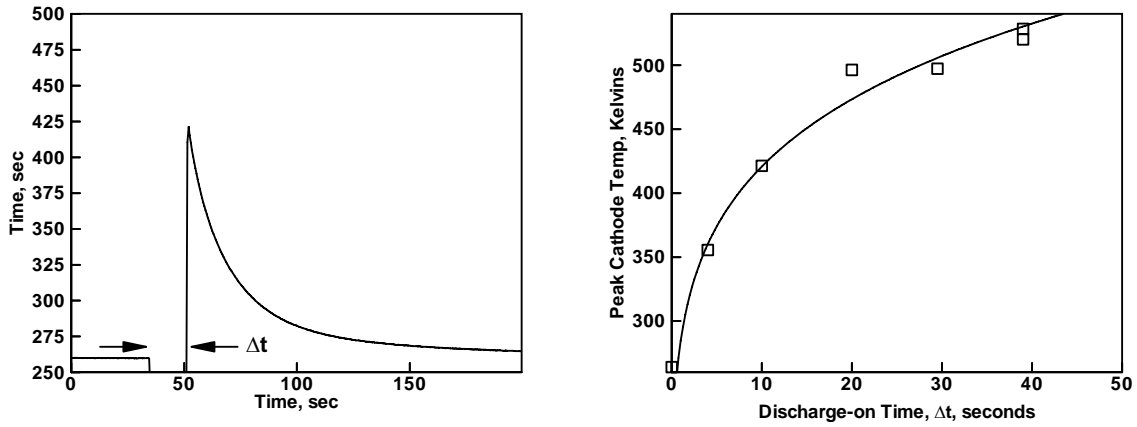


Figure 60 Cathode temperature as a function of time before and after a ten-second discharge (left), and peak cathode temperature as a function of discharge-on time.

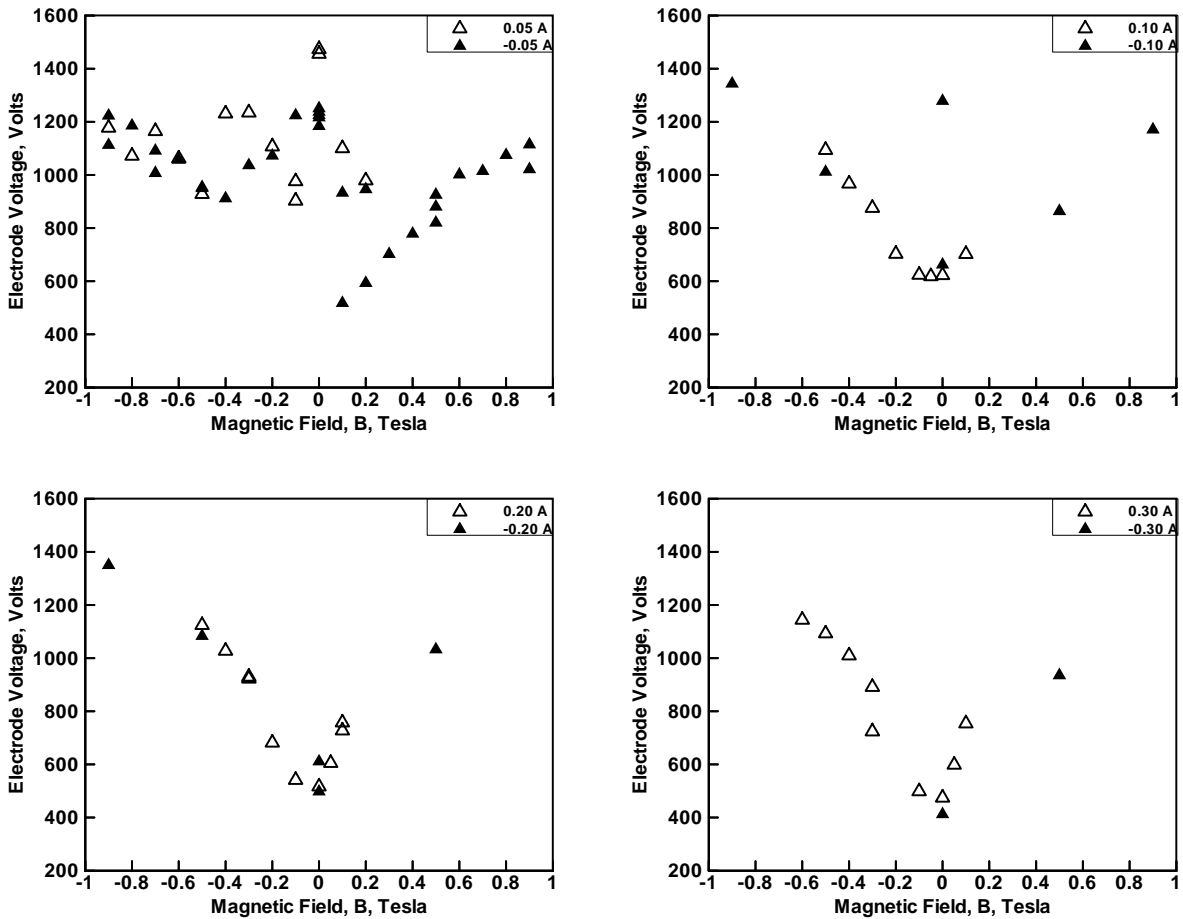


Figure 61 Effect of magnetic field on the voltage required to drive a given current.

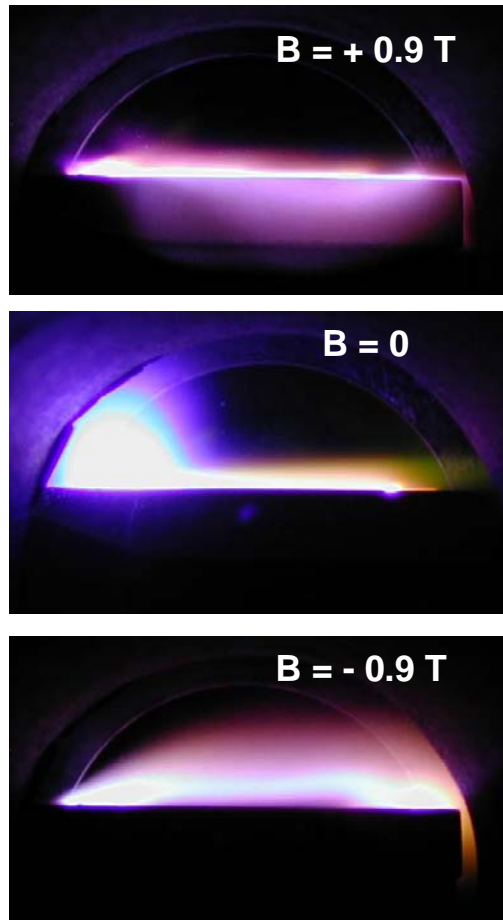


Figure 62 Images showing the effect of transverse magnetic fields on the glow from a surface discharge. Flow is from left-to-right, cathode upstream.

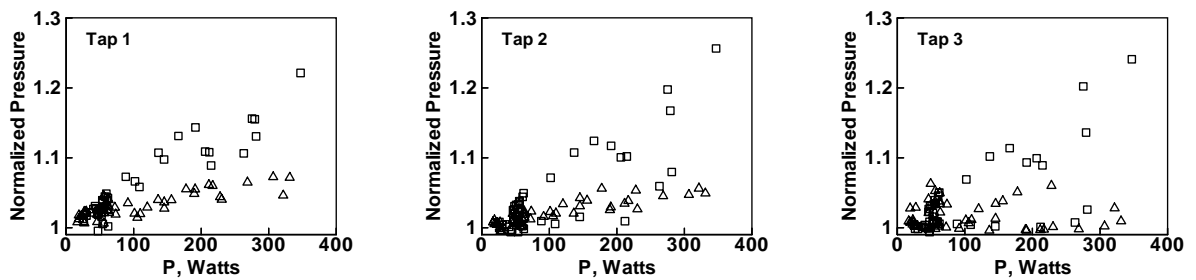


Figure 63 Induced pressure at each measuring station as a function of power. Squares, cathode upstream, triangles, cathode downstream.

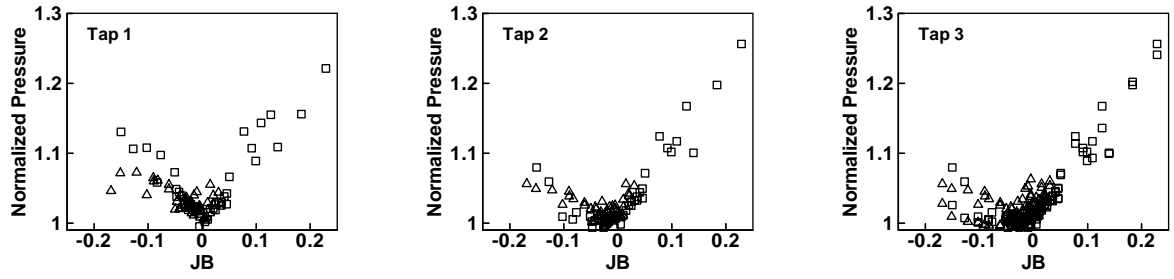


Figure 64 Pressure induced by the discharge at each measuring station plotted versus the product of current and magnetic field.

6. References

- ¹ Reed, H. L., Kimmel, R. L., Schneider, S., Arnal, D., and Saric, W., "Drag Prediction and Transition in Hypersonic Flow," AGARD Paper C-15, Symposium on Sustained Hypersonic Flight, AGARD Conference on Future Aerospace Technology in the Service of the Alliance, 14-17 April 1997, Ecole Polytechnique, Palaiseau, France.
- ² Whitehead, A., "NASP Aerodynamics," AIAA paper 89-5013, July 1989.
- ³ Small, W. J., Kirkham, F. S., and Fetterman, D. E., "Aerodynamic Characteristics of a Hypersonic Transport Configuration at Mach 6.86," NASA Technical Note NASA TN D-5885, June, 1970.
- ⁴ Burns, K. A., Deters, K. J., Haley, C. P., and Khilken, T. A., "Viscous Effects on Complex Configurations," Air Force Wright Laboratory Technical Report WL -TR-95-3060 (ADA302456), August 1995.
- ⁵ Finley, D., "Hypersonic Aerodynamics Considerations and Challenges," AIAA paper AIAA-90-5222, October 1990.
- ⁶ Suchomel, C. F., Van Wie, and D. Risha, D. J., "Perspectives on Cataloging Plasma Technologies Applied to Aeronautical Sciences," AIAA Paper 2003-3852, June 2003.
- ⁷ Heiser, W. H. and Pratt, D. T., *Hypersonic Airbreathing Propulsion*, American Institute of Aeronautics and Astronautics, Washington, D.C., 1994, pp 237-239.
- ⁸ Blottner, F. G., "Chemical Nonequilibrium Boundary Layer," *AIAA Journal*, Vol. 2, No. 2, February 1964, pp. 232-240.
- ⁹ Corke, T. C., Cavalieri, D. A., and Matlis, E., "Boundary-Layer Instability on Sharp Cone at Mach 3.5 with Controlled Input," *AIAA Journal*, Vol. 40, No. 5, May 2002, pp. 1015-1018.
- ¹⁰ Kastell, D. and Shipliyuk, A. N., "Experimental technique for the investigation of artificially generated disturbances in planar laminar hypersonic boundary layers," *Aerospace Science and Technology*, No. 6, 1999, pp. 345-354.
- ¹¹ Maslov, A. A., Mironov, S. G., Shipliyuk, A. A., Sidorenko, A. A., Buntin, D. A., and Aniskin, V. M., "Hypersonic Flow Stability Experiments," AIAA Paper 2002-0153, January 2002.
- ¹² Lineberry, J. T., Rosa, R. J., Bitiyurin, V. A., Botcharov, A. N., and Potebnya, V. G., "Prospects of MHD Control for Hypersonics," AIAA Paper 2000-3057.
- ¹³ Rossow, V. J., "On Flow of Electrically Conducting Fluids Over a Flat Plate in the Presence of a Transverse Magnetic Field," NACA TN 3971, May 1957.
- ¹⁴ Ostrach, S., "Laminar Flows with Body Forces," *High Speed Aerodynamics and Jet Propulsion, Vol. IV, Theory of Laminar Flows*, Moore, F. K. ed., Princeton University Press, Princeton, NJ, 1964, pp. 691-712.
- ¹⁵ Bush, W. B., "Compressible Flat-Plate Boundary-layer Flow With an Applied Magnetic Field," *J. of the Aerospace Sciences*, Vol. 27, No. 1, January 1960, pp. 49-58.

- ¹⁶ Sastry, M. S., "Magneto Hypersonic Boundary-Layer Flow past a Plate," *AIAA Journal*, Vol. 5, No. 1, 1967.
- ¹⁷ Crawford, C. H., and Karniadakis, G. E., "Control of External Flows via Electro-Magnetic Fields," AIAA paper 95-2185, June 1995.
- ¹⁸ Borghi, C. A., Carraro, M. R., and Cristofoline, A., "Numerical Modeling of MHD Interaction in the Boundary Layer of Hypersonic Flows," *IEEE Transactions on Magnetics*, Vol. 39, No. 3, May 2003, pp. 1507-1510.
- ¹⁹ Poggie, J., and Gaitonde, D. V., "Magnetic Control of Hypersonic Blunt Body Flow," AIAA paper 2000-0452, January 2000.
- ²⁰ Bush, W. B., "Magnetohydrodynamic-Hypersonic Flow Past a Blunt Body," *J. of the Aerospace Sciences*, Vol. 25, No. 11, Nov. 1958, pp. 685-690, 728.
- ²¹ Bussing, T. R. A., Eberhardt, S., "Chemistry Associated with Hypersonic Vehicles," AIAA paper 87-1292, June 1987.
- ²² Palm, P., Meyer, R., Plönjes, E., Bezant, A., Adamovich, I. V., Rich, J. W., and Gogineni, S., "MHD Effect on a Supersonic Weakly Ionized Flow," AIAA paper 2002-2246, May 2002.
- ²³ Kimmel, R. L., Hayes, J. R., Menart, J., Shang, J., and Henderson, S., "Measurements of a Transverse DC Discharge in a Mach 5 Flow," AIAA paper 2003-3855, June 2003.
- ²⁴ Macheret, S. O., Shneider, M. N., and Miles, R. B., "Magnetohydrodynamic and Electrohydrodynamic Control of Hypersonic Flows of Weakly Ionized Plasmas, AIAA paper 2002-2249, May 2002.
- ²⁵ Sears, W. R. "Magnetohydrodynamic Effects in Aerodynamic Flows," *ARS Journal*, Vol. 29, No. 6, June 1954, pp. 397-406.
- ²⁶ Heno, C., and Stace, J., "Experimental investigation of a salt water turbulent boundary-layer modified by an applied streamwise magnetohydrodynamic body force," *Physics of Fluids*, Vol. 7, No. 6, June 1995, pp. 1371-1383.
- ²⁷ Van Driest, E. R., "Turbulent Boundary Layer in Compressible Fluids," *Journal of the Aeronautical Sciences*, Vol. 18, No. 3, March 1951, pp. 145-160, 216.
- ²⁸ Weier, T., Gerbeth, G., Mutschke, G., Platacis, E., Lielausis, O., "Experiments on cylinder wake stabilization in an electrolyte solution by means of electromagnetic forces localized on the cylinder surface," *Experimental Thermal and Fluid Science*, Vol. 16, nos. 1&2, January/February 1998, pp. 84-91.
- ²⁹ Menart, J. A., Shang, J., Kimmel, R. L., and Hayes, J. R., "Effects of Magnetic Fields on Plasmas Generated in a Mach 5 Wind Tunnel," AIAA 2003-4165, June 2003.
- ³⁰ Jaffe, N. A., "Effects of a Transverse Magnetic Field and Spanwise Electric Field on the Boundary-layer of a Conducting Fluid," *AIAA Journal*, Vol. 4, No. 10, pp. 1843-1846, Oct. 1966.
- ³¹ Rossow, V. J., "Boundary-Layer Stability Diagrams for Electrically Conducting Fluids in the Presence of a Magnetic Field," NACA TN 4282, August, 1958.

- ³² Cheng, F. Zhong, X., Gogineni, S., and Kimmel, R. L., “Effect of Applied Magnetic Field on the Instability of Mach 4.5 Boundary-layer over a Flat Plate, AIAA paper 2002-0351, January 2002.
- ³³ Cheng, F., Zhong, X., Gogineni, S., and Kimmel, R. L., “Magnetic-field effects on second-mode instability of a weakly ionized Mach 4.5 boundary layer,” *Physics of Fluids*, Vol. 15, No. 7, July 2003, pp. 2020-2040.
- ³⁴ Chandrasekhar, S., “The stability of viscous flow between rotating cylinders in the presence of a magnetic field,” *Proceedings of the Royal Society of London*, series A, Vol. 216, February 1953, pp. 293-309.
- ³⁵ Stuart, J. T., “On the stability of viscous flow between parallel planes in the presence of a co-planar magnetic field,” *Proc. Roy. Soc. London*, ser A, Vol. 221, No. 1145, 21 Jan 1954.
- ³⁶ Lock, R. C., “The stability of the flow of an electrically conducting fluid between parallel planes under a transverse magnetic field,” *Proc. Roy. Soc. Of London*, Ser. A, Vol. 233, no. 1192, 6 Dec. 1955, pp. 105-125.
- ³⁷ Mack, L. M., “Boundary-Layer Stability Theory,” *Special Course on Stability and Transition of Laminar Flow*, edited by R. Michel, AGARD Report No. 709, pp. 3-1 to 3-81, 1984.
- ³⁸ Kimmel, R. L., Poggie, J., and Schmisser, J. D., “Effect of Pressure Gradients on Axisymmetric Hypersonic Boundary-layer Stability,” AIAA-2000-0538, January 2000.
- ³⁹ McEldowney, B., Meyer, R., Chintala, N., and Adamovich, I. V., “Measurements of Electrical Parameters of a Supersonic Nonequilibrium MHD Channel,” AIAA Paper 2003-4279, June 2003.
- ⁴⁰ Rosa, R. J., *Magnetohydrodynamic Energy Conversion*, McGraw-Hill Book Company, New York, 1968, pp. 1-24.
- ⁴¹ Roth, J. R., Sherman, D. M., and Wilkinson, S. P., “Electrohydrodynamic Flow Control with a Glow-Discharge Surface Plasma,” *AIAA Journal*, Vol. 38, No. 7, July 2000, pp. 1166-1172.
- ⁴² Artana, G., D’Adamo, J., Léger, L., Moreau, E., and Touchard, G., “Flow Control with Electrohydrodynamic Actuators,” AIAA Paper 2001-0351.
- ⁴³ Léger, L., Moreau, E., and Touchard, G., “Electrohydrodynamic airflow control along a flat plate by a DC surface corona discharge – Velocity profile and wall pressure measurements,” AIAA Paper 2002-2833.
- ⁴⁴ Corke, T. C., Jumper, E. J., Post, M. L., Orlov, D., and McLaughlin, T. E., “Application of Weakly-Ionized Plasmas as Wing Flow-Control Devices,” AIAA 2002-0350, Jan. 2002.
- ⁴⁵ Post, M. L., Corke, T. C., “Separation Control on High Angle of Attack Airfoil Using Plasma Actuators,” AIAA Paper 2003-1024, January 2003.

- ⁴⁶ Hultgren, L. S., and Ashpis, D. E., "Demonstration of Separation Delay with Glow-Discharge Plasma Actuators," AIAA Paper 2003-1025, January 2003.
- ⁴⁷ Roth, J. R., Sin, H., Madhan, R. C. M., and Wilkinson, S. P., "Flow Re-Attachment and Acceleration by Piezoelectric and Peristaltic Electrohydrodynamic (EHD) Effects," AIAA Paper 2003-531, January 2003.
- ⁴⁸ Johnson, G. A., and Scott, S., J., "Plasma-Aerodynamic Boundary Layer Interaction Studies," AIAA Paper 2001-3052.
- ⁴⁹ Wilkinson, S. P., "Investigation of an Oscillating Surface Plasma for Turbulent Drag Reduction," AIAA Paper 2003-1023, January 2003.
- ⁵⁰ Shibkov, V. M., Alexandrov, A. F., Chernikov, A. V., Ershov, A. P., Georgievskiy, P. Yu., Gromov, V. G., Larin, O. B., Levin, V. A., Shibkova, L. V., Timofeev, I. B., Voskanyan, A. V., Zlobin, V. V., "Influence of the Surface Microwave Discharge on the Parameters of Supersonic Airflow Near a Dielectric Body," AIAA Paper, 2003-1192, January 2003.
- ⁵¹ Leonov, S., Bityurin, V., Savischenko, N., Yuriev, A., and Gromov, V., "Influence of Surface Electric Discharge on Friction of Plate in Subsonic and Transonic Airflow," AIAA paper 2001-0640, January 2001.
- ⁵² Leonov, S., Bityurin, V., Klimov, A., Kolesnichenko, Y., and Yuriev, A., "Influence of Structural Electric Discharges on Parameters of Streamlined Bodies in Airflow," AIAA paper 2001-3057, June 2001.
- ⁵³ Leonov, S., Bityurin, V., Savelkin, K., and Yarantsev, D., "Effect of Electrical Discharge on Separation Processes and Shocks Position in Supersonic Airflow," AIAA paper 2002-0355, January 2002.
- ⁵⁴ Leonov, S., Bityurin, V., Savelkin, K., and Yarantsev, D., "Progress in Investigation for Plasma Control of Duct-Driven Flows," AIAA paper 2003-0699, January 2003.
- ⁵⁵ Leonov, S., Bityurin, V., and Yarantsev, D., "The Effect of Plasma Induced Separation," AIAA paper 2003-3853, June 2003.
- ⁵⁶ Shang, J. S., Ganguly, B., Umstadtd, R., Hayes, J., Arman, M., and Bletzinger, P., "Developing a Facility for Magneto-Aerodynamics Experiments, *Journal of Aircraft*, Vol. 17, No. 7, Nov.-Dec., 2000, pp. 1065-1072.
- ⁵⁷ Shang, J. S., Hayes, J. R., Miller, J. H., Menart, J. A., "Magneto-Aerodynamic Interactions in Weakly Ionized Hypersonic Flow," AIAA paper 2002-0349, January 2002.
- ⁵⁸ Menart, J. A., Shang, J., Henderson, S., Kurpik, A., Kimmel, R. L., Hayes, J., R., "Survey of Plasmas Generated in a Mach 5 Wind Tunnel," AIAA-2003-1194, January 2003.
- ⁵⁹ Shang, J. S., Kimmel, R. L., Hayes, J. R., and Tyler, C., "Performance of a Low-Density Hypersonic Magneto-Aerodynamic Facility," AIAA 03-0329, January 2003.

- ⁶⁰ Kurpik, A., Menart, J., Shang, J., Kimmel, R. L., and Hayes, J. R., "Technique for Making Microwave Absorption Measurements in a Small Plasma Discharge," AIAA 2003-3748, June 2003.
- ⁶¹ Dahm, F. J., "Air Condensation in a Hypersonic Wind Tunnel," *AIAA Journal*, Vol. 1, No. 5, May 1963, pp. 1043-1046.
- ⁶² Raizer, Yuri P., *Gas Discharge Physics*, Springer-Verlag New York, 1997.
- ⁶³ Shang, J. S., Hayes, J. R., Miller, J. H., Menart, J. A., "Blunt Body in Hypersonic Electromagnetic Flow Field," AIAA paper 2001-2803, June 2001.
- ⁶⁴ Ames Research Staff, "Equations, Tables, and Charts for Compressible Flow," NACA Report 1135, National Advisory Committee for Aeronautics, Ames Aeronautical Laboratory, Moffett Field, California, 1953.
- ⁶⁵ Estevadeordal, J., Gogineni, S., Kimmel, R. L., and Hayes, J. R., "Schlieren Imaging in Hypersonic Plasmas," AIAA 2004-1139, January 2004.
- ⁶⁶ Heald, M. A. and Wharton, C. B., *Plasma Diagnostics with Microwaves*, Wiley, New York, 1965.
- ⁶⁷ Meuth, H., and Sevillano, E., "Microwave Diagnostics," in *Plasma Diagnostics*, Vol. 1, edited by Auciello, O. and Flamm, D., Academic Press, pp. 239-311, 1989.
- ⁶⁸ Wharton, C. B., "Microwave Techniques," in *Plasma Diagnostic Techniques*, ed. by Huddleston, R. H. and Leonard, S. L., Academic Press, New York, pp. 477-516, 1965.
- ⁶⁹ Blevins, J. A., Frederick, R. A., and Coleman, H. W., "An assessment of microwave measurement techniques in rocket exhaust applications," AIAA Paper 94-0671, Jan. 1994.
- ⁷⁰ Frederick, R. A., Blevins, J. A., and Coleman, H. W., "Investigation of microwave attenuation measurements in a laboratory-scale rocket motor plume," *Journal of Spacecraft*, Vol. 32, No. 5, 1995.
- ⁷¹ Funaki, I., Ogawa, H., Kato, T., Abe, T., Fujita, K., and Nonaka, S., "Microwave attenuation measurement of full-scale solid rocket motor plumes," AIAA Paper 2002-2241, May 2002.
- ⁷² Palm, P., Plönjes, E., Buoni, M., Subramaniam, V. V., and Adamovich, I. V., "Electron density and recombination rate measurements in CO-seeded optically pumped plasmas," *Journal of Applied Physics*, Vol. 89, No. 11, June 2001.
- ⁷³ Huxley and Crompton, *Diffusion and Drift of Electrons in Gases*, John Wiley & Sons, Inc., 1974.
- ⁷⁴ Palm, P., Private communication, July 2002.
- ⁷⁵ Howatson, A. M., *An Introduction to Gas Discharges*, Pergamon Press, New York, 1976, p. 183.
- ⁷⁶ Menart, J., Shang, J., and Hayes, J., "Development of a Langmuir Probe for Plasma Diagnostic Work in High Speed Flow," AIAA paper 2001-2804, June 2001.

- ⁷⁷ Menart, J. and Shang, J., "Data Reduction Analysis for Cylindrical, Double Langmuir Probes Operating in Collisionless to Collisional, Quiescent Plasmas," AIAA paper 2003-0136, January 2003
- ⁷⁸ Greenspan, M., "Rotational Relaxation in Nitrogen, Oxygen, and Air," *The Journal of the Acoustical Society of America*, Vol. 31, No. 2, February 1959, pp. 155-160.
- ⁷⁹ Kistemaker, P. G., Tom, A., and De Vries, A. E., "Rotational Relaxation Numbers for the Isotopic Molecules of N₂ and CO," *Physica*, Vol. 48, 1970, pp. 414-424.
- ⁸⁰ Andersen, W. H., and Hornig, D. F., "The structure of shock fronts in various gases," *Molecular Physics*, Vol. 2, pp. 49-63, 1959.
- ⁸¹ Heiser, W. H., and Pratt, D. T., *Hypersonic Airbreathing Propulsion*, American Institute of Aeronautics and Astronautics, Washington, D.C., 1994, pp. 66-81.
- ⁸² Menart, J. A., Henderson, S., Shang, J., Kimmel, R. L., and Hayes, J. R., "DC Plasma Discharge Effects on a Mach 5 Flow Between Small Plate Electrodes," AIAA 2004-2264, June 2004.
- ⁸³ Hayes, W. F., and Probstein, R. F., *Hypersonic Flow Theory*, Academic Press, New York, 1959.
- ⁸⁴ Kimmel, R. L., "Aspects of Hypersonic Boundary Layer Transition Control," AIAA Paper 2003-0772, January 2003.